Impacts of Salt and pH on the Phase Behavior of Sea Spray Aerosol Proxy Films

THESIS

Presented in Partial Fulfillment of the Requirements for the Degree Master of Science in the Graduate School of The Ohio State University

By

Kimberly A. Carter, B.A.

Graduate Program in Chemistry

The Ohio State University

2018

Master's Examination Committee:

Prof. Dr. Heather C. Allen, Advisor

Prof. Dr. Sherwin J. Singer

Abstract

Sea spray aerosol (SSA) constitutes one of the largest fractions of aerosol emissions on the planet, and it impacts Earth's radiative budget by regulating cloud albedo, cloud formation, and ice nucleation in the troposphere. Organic matter from the ocean is enriched in SSA with surfactants comprising one of the most surface active classes of compounds. Saturated fatty acids are particularly abundant and readily form thin films at the air-water interface. In this study, a proxy SSA mixture was used to examine interfacial amphiphile organization and dynamics as a function of aqueous subphase composition. The goal was to understand how soluble fatty acids impact film phase behavior at various SSA-relevant pH values. To do this, surface pressure-area isotherms were conducted at nascent SSA and at acidified SSA conditions. Soluble surfactants contribute to SSA proxy phase behavior regardless of the pH, but their overall impact on surface organization increases with decreasing pH. Thus, as SSA acidifies in the marine boundary layer, the surface activity of soluble fatty acids dramatically increases. This work highlights the necessity of including parameters for soluble surfactants in global climate models.

Dedication

To Kevin and Patch

Acknowledgements

I would like to thank my advisor, Dr. Heather Allen, for her support and guidance in the pursuit of this degree. I would also like to thank Dr. Bethany Wellen Rudd for helpful discussions, advice, and feedback throughout the course of this project. I am particularly grateful for my undergraduate researchers, Michelle Fiamingo and Jeongin Kim, for their helpful contributions to my research and for motivating me to be a better scientist and mentor. Allen lab group members are also deserving of thanks for their helpfulness and companionship. I owe gratitude to my family for their love and support throughout my educational journey. Finally, I would like to thank Kevin Fenk for his partnership, encouragement, insightful input, and endless patience.

Vita

August 17, 1993	Born - Wooster, OH, USA
May 22, 2012	Valedictorian, Triway High School, Wooster, OH, USA
May 16, 2016	B.A. Chemistry, The College of Wooster, Wooster, OH, USA
August 2016 - August 2017	GAANN Fellow, Department of Chemistry & Biochemistry, The Ohio State University, Columbus, OH, USA
August 2017 - Present	Graduate Teaching Associate, Department of Chemistry & Biochemistry, The Ohio State University, Columbus, OH, USA

Publications

Edmiston, P. L.; Carter, K. A.; Graham, A. L.; Gleason, E. J. Chemisorption of Microcystins to a Thiol and Amine Functionalized Organosilica. *Separation and Purification Technology* **2018**, *197*, 244–252.

Field of Study

Major Field: Chemistry

Table of Contents

List of Figures

List of Abbreviations & Symbols

Abbreviations

C_{12}	Lauric Acid
C_{14}	Myristic Acid
C_{16}	Palmitic Acid
C_{18}	Stearic Acid
CCN	Cloud Condensation Nuclei
Control	2 Myristic Acid : 4 Palmitic Acid : 3 Stearic Acid
G	Gaseous Phase
GDS	Gibbs Dividing Surface
GHG	Greenhouse Gas
L	Liquid Phase
LC	Liquid-Condensed Phase
LE	Liquid-Expanded Phase
MMA	Mean Molecular Area
S	Solid Phase
SSA	Sea Spray Aerosol
SSA Proxy	1 Lauric Acid : 2 Myristic Acid : 4 Palmitic Acid : 3 Stearic Acid
SSML	Sea Surface Microlayer
$\Pi - A$	Surface Pressure-Area

Symbols

W	Work
γ	Surface Energy
A	Interfacial Area
f	Force Opposing Interfacial Displacement
x	Displacement of Interface
α	Bulk Liquid Phase
β	Bulk Gaseous Phase
σ	Interfacial Plane
V^{σ}	Interfacial Volume
U	Internal Energy
Q	Heat

T	Temperature
S	Entropy
p	Pressure
V	Volume
μ_i	Chemical Potential of Species i
N_i	Number of Species i
U^α	Internal Energy of Phase α
U^β	Internal Energy of Phase β
U^σ	Internal Energy of Phase σ
S^α	Entropy of Phase α
S^β	Entropy of Phase β
S^σ	Entropy of Phase σ
V^α	Volume of Phase α
V^β	Volume of Phase β
N_i^α	Number of Species i in Phase α
N_i^β	Number of Species i in Phase β
N_i^σ	Number of Species i in Phase σ
p_α	Pressure of Phase α
p_β	Pressure of Phase β
$S_\sigma^{(1)}$	Surface Excess Entropy
Γ_i^σ	Surface Excess Concentration
Γ_i^1	Surface Excess Concentration Relative to Species 1
μ_i^0	Standard Chemical Potential of Species i
R	Ideal Gas Constant
a	Activity
a_0	Standard Activity
s	Entropy Density
c	Concentration
s^α	Entropy Density of Phase α
s^β	Entropy Density of Phase β
c_i^α	Concentration of Species i in Phase α
c_i^β	Concentration of Species i in Phase β
S_σ^1	Relative Excess Function for Entropy
π	Surface Pressure
γ_0	Subphase Surface Tension
γ_f	Film Surface Tension
F_g	Gravitational Force
F_b	Buoyancy Force
F_{net}	Sum of Forces Acting on Wilhelmy Plate
ρ_p	Wilhelmy Plate Density
l	Wilhelmy Plate Length
w	Wilhelmy Plate Width
t	Wilhelmy Plate Thickness
θ	Contact Angle

ρ_0	Subphase Density
h	Depth of Wilhelmy Plate Immersion into the Subphase
k_B	Boltzmann Constant
a_v	van der Waals Constant
C	London Dispersion Force Coefficient
N_0	Number of Molecules
σ_d	Molecular Diameter
b	Excluded Area Per Mole of Molecules
A_{12}	Total Area Per Molecule of a Mixed Film
X_1	Mole Fraction of Amphiphile 1
X_2	Mole Fraction of Amphiphile 2
A_1	Mean Molecular Area of Amphiphile 1
A_2	Mean Molecular Area of Amphiphile 2
π_{12}	Mixture of Surface Pressure
π_1	Surface Pressure of Amphiphile 1
π_2	Surface Pressure of Amphiphile 2
ΔG^{exc}	Gibbs Excess Free Energy of Mixing
A^{exc}	Excess Area of Mixing
ΔG^M	Total Free Energy of Mixing
ΔG^{id}	Ideal Gibbs Free Energy of Mixing
t	Time
N_t	Number of Molecules in Film at Time t
k	Desorption Rate
$[\text{Mixture}]_\text{c}$	Corrected SSA Proxy Mixture Concentration
n_myristic	Moles of Myristic Acid
n_palmitic	Moles of Palmitic Acid
n_stearic	Moles of Stearic Acid
V_lauric	Volume of Lauric Acid in SSA Proxy Mixture
V_myristic	Volume of Myristic Acid in SSA Proxy Mixture
V_palmitic	Volume of Palmitic Acid in SSA Proxy Mixture
V_stearic	Volume of Stearic Acid in SSA Proxy Mixture
$\text{MMA}_\text{corrected}$	Corrected SSA Proxy Mean Molecular Area
$\text{MMA}_\text{uncorrected}$	Uncorrected SSA Proxy Mean Molecular Area

Chapter 1

Introduction

1.1 Aerosol Impacts on Climate

Earth's surface temperature has risen precipitously since 1850 due to increased anthropogenic greenhouse gas (GHG) emissions, and the 30-year period between 1983 and 2012 was likely the warmest in 1400 years.[1] Oceans store a majority of the radiative energy in the climate system; approximately 90% of the energy accumulated from 1971-2010 was stored via ocean warming. Consequently, climate models project that Earth's oceans will warm by 0.6°C to 2.0°C throughout the 21st century, and this warming will likely continue to generate global change for hundreds to thousands of years even after global surface temperature stabilization.[2] Higher atmospheric concentrations of CO_2 also increased CO_2 dissolution into seawater, leading to a 0.1 decrease in ocean pH. Earth System Models predict a decrease in surface ocean pH of 0.06-0.07 at minimum and 0.30-0.32 at maximum by the end of the century.[1] Thus global change is inevitable and ongoing, so understanding its impacts on atmospheric and marine environments will be imperative to mitigate the effects of climate change.

It is uncertain how rising ocean temperatures and ocean acidification will impact aerosol production at the air-sea interface and oxidative reactions in the troposphere.

Significant uncertainty in the representation of cloud and aerosol processes remains in climate models, and the net impact of aerosols on the global radiative budget is unclear (Figure 1.1).[2] Aerosols can directly impact climate by absorbing and scattering solar radiation. Additionally, aerosols can indirectly affect the global radiative budget via cloud seeding and ice nucleation in the atmosphere.[3] Indirect radiative forcing from natural emissions of volcanic sulfur dioxide, marine dimethylsulfide, biogenic volatile organic carbon, biomass burning, and sea spray constituted 45% of the variance in models of aerosol forcing since 1750. Anthropogenic emissions contributed 34% of the variance in the model.[4] Hence, characterizing the composition, transformations, and climate impacts of natural aerosols will be crucial for determining the forcing from anthropogenic aerosols with greater certainty.[4,5]

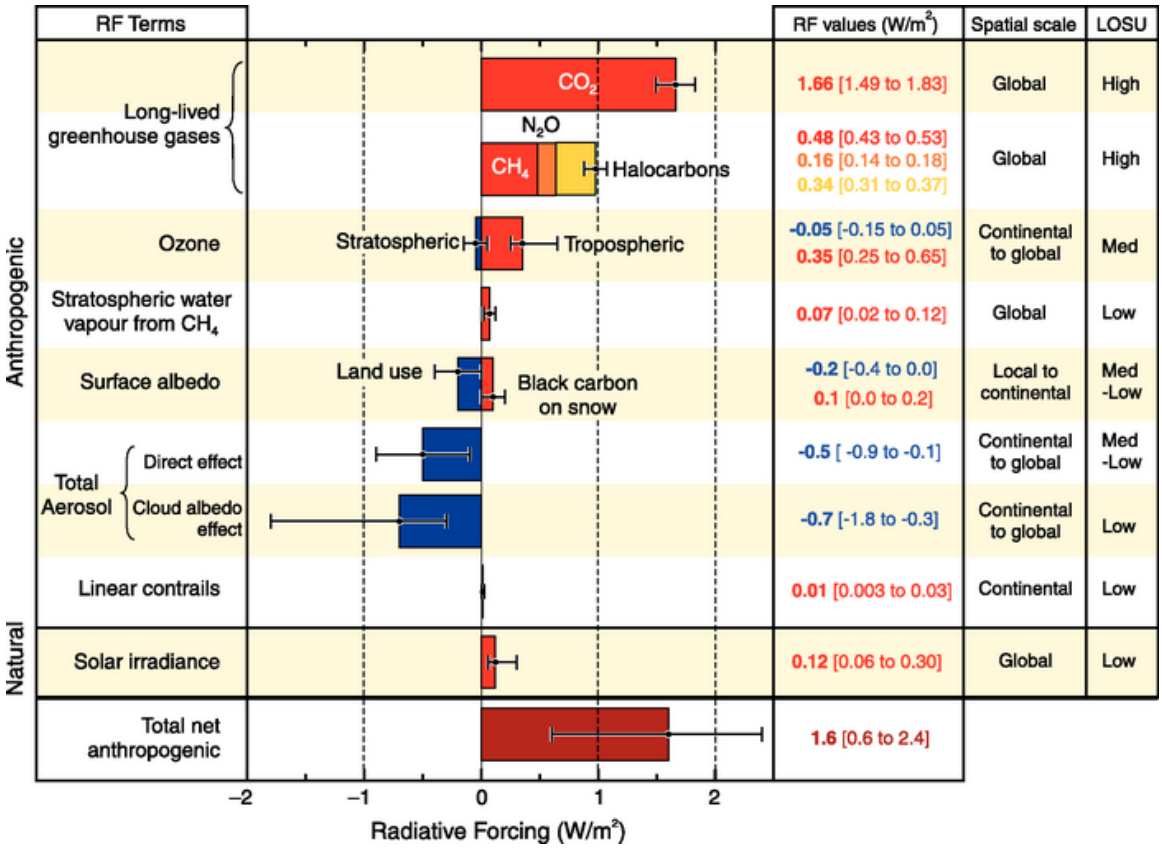

Figure 1.1: Global radiative forcing components. Figure reproduced from the IPCC Climate Change 2007: Synthesis Report, Figure 2.4.[6]

1.2 Sea Spray Aerosol

Marine aerosols, also known as sea spray aerosols (SSA), are one of the largest sources of aerosol emissions which contribute approximately 3.5×10^{12} kg yr^{-1}.[7] SSA is formed when air is entrained into the sea surface via breaking waves, and these bubbles burst upon reaching the air-sea interface.[8] While traversing through the water column, the bubbles scavenge surface active organic material which becomes incorporated into the SSA.[9] Upon bubble bursting, hundreds of film drops are generated from the bubble film cap, and a smaller number of jet drops are produced by the cavity at the base of the bubble destabilizing and releasing a jet of surface seawater.[10,11] The composition of each type of drop is a consequence of the source of material from the bubble. Film caps of bubbles are highly enriched in surface active organic material, such as fatty acids. Bubble rupturing is caused by the film cap thinning to the point of collapse, so the film droplets produced are also submicron in diameter. Jet drops tend to be larger than 1 μm, and their composition more closely reflects that of surface seawater. Hence, jet drops are enriched in organic material, but they tend to contain more soluble and particulate organic matter.[11–15]

1.2.1 Modeling Marine Aerosol

Aerosols are able to influence cloud areal extent, dynamics, and lifetime; and these cloud physical properties consequently affect albedo, defined as the fraction of light scattered from a particle.[16] Additionally, aerosols can act as cloud condensation nuclei (CCN) by promoting water condensation on their surfaces.[17] Surface-active organic compounds in aerosol particles enhance cloud formation, as predicted by a modified Köhler theory.[18] Aerosol surface tension depression due to surface-active organics decreases critical supersaturation and increases critical wet diameter, which are parameters that define the point at which an aerosol is considered to be an activated

CCN. As such, the barrier to cloud formation is reduced. In order to accurately predict aerosol contributions to atmospheric processes, appropriate climate models must be developed and parameterized.

Submicron SSA organic enrichment is particularly pronounced in oceanic regions downwind of phytoplankton blooms.[19–24] Organic enrichment has also been measured in laboratory-generated SSA.[14,25–31] The composition and flux of organic matter is especially important in global climate models. Various models have used empirical relationships to chlorophyll *a* concentrations in the ocean as a way to parameterize the organic content in nascent SSA, but it is only moderately predictive.[12,32–34] Therefore, a model incorporating a two-layer competitive Langmuir adsorption equilibrium, called OCEANFILMS-2, has been developed in which the surface activity of particular classes of ocean-relevant compounds are parameterized using experimental data.[35–38] Cooperative adsorption of soluble organics, such as polysaccharides, to an insoluble monolayer is included; this improves the alkane : hydroxyl ratio determined from spectroscopic measurements of ambient SSA.[38] While OCEANFILMS-2 more closely predicts the alkane : hydroxyl ratio of 0.24–0.38 from ship campaigns,[21,39,40] the model produces an alkane contribution that is erroneously high with a ratio value of 0.41–0.69. Consequently, the components contributing to the alkane signatures, primarily surface active fatty acids, need to be better parameterized to account for this descrepancy.

1.3 The Sea Surface Microlayer

Oceans cover approximately 71% (362 million km^2) of Earth's surface, providing one of the largest environmental interfaces on the planet. This interface, known as the sea surface microlayer (SSML), occupies 1 - 1,000 μm of the uppermost layer of the ocean. The SSML is chemically distinct from underlying seawater. Molecular adsorption and

aggregation at the surface yield organic matter and trace metal enrichment. This enrichment is thought to dictate the composition of sea spray aerosol formed by breaking waves. Chemical composition and transformation of sea spray aerosols is only beginning to become more thoroughly characterized, and its impact on climate is poorly understood.[11]

1.3.1 Surfactant Enrichment

The chemical composition of the SSML is complex, and this chemical complexity is transferred to SSA upon wave breaking. However, the enrichment of surfactants in SSA is of particular interest due to their high surface activity. Aliphatic moieties tend to form a film on the outside of aerosol particles, thus acting as a barrier to any photochemical or atmospheric processes. To better characterize the transfer of anionic surfactants into sea spray aerosol, a laboratory mesocosm experiment was conducted in which a phytoplankton bloom was grown in a large wave flume.[28] Aerosol was then collected from the flume and analyzed with liquid chromatography in tandem with high-resolution mass spectrometry. Saturated fatty acids between 8 and 24 carbons in length were the most abundant species measured in the SSML and in all sizes of aerosol. More specifically, palmitic acid (C_{16}) and stearic acid (C_{18}) constituted about two-thirds of the saturated fatty acids. Shorter-chain saturated fatty acids such as myristic acid (C_{14}) and lauric acid (C_{12}) were also abundant. In SSA with a diameter ≤ 2.5 μm, the most prevalent fatty acid was palmitic acid, followed by stearic acid, myristic acid, and lauric acid (Figure 1.2).

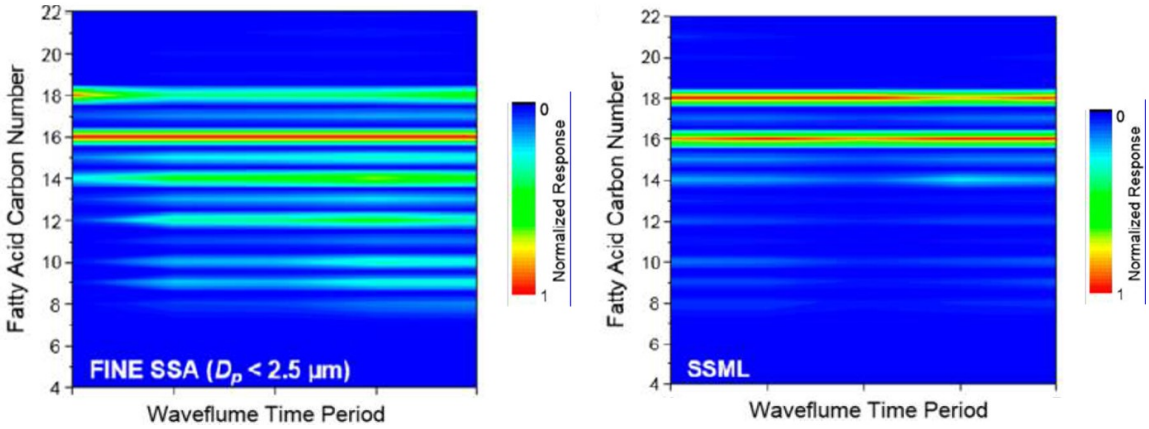

Figure 1.2: Normalized fatty acid signal responses from the SSML and SSA with particle diameters ≤ 2.5 μm. Figure adapted from reference.[28]

1.4 Objectives

This study aims to examine the interfacial organization and dynamics of proxy sea spray aerosol films. A surfactant mixture of 1 lauric acid : 2 myristic acid : 4 palmitic acid : 3 stearic acid (Figure 1.3) was chosen based on the fatty acid enrichment data presented in Figure 1.2. Phase dynamics of this proxy SSA monolayer were measured using surface pressure-area isotherms on a variety of aqueous subphases. The subphase compositions were chosen to mimic the transformations of the aqueous component of SSA throughout its lifetime in the atmosphere. The aqueous portion of nascent SSA closely mimics that of bulk seawater with a sodium chloride concentration around 0.4 M and a pH of 8.2,[41] and the aerosols acidify over time in the marine boundary layer.[42] A discussion of the theory guiding the surface chemistry and instrumentation is presented in Chapter 2, and the experimental details are detailed in Chapter 3. An analysis of the surface pressure-area isotherm data and its implications on climate modeling are discussed in Chapter 4.

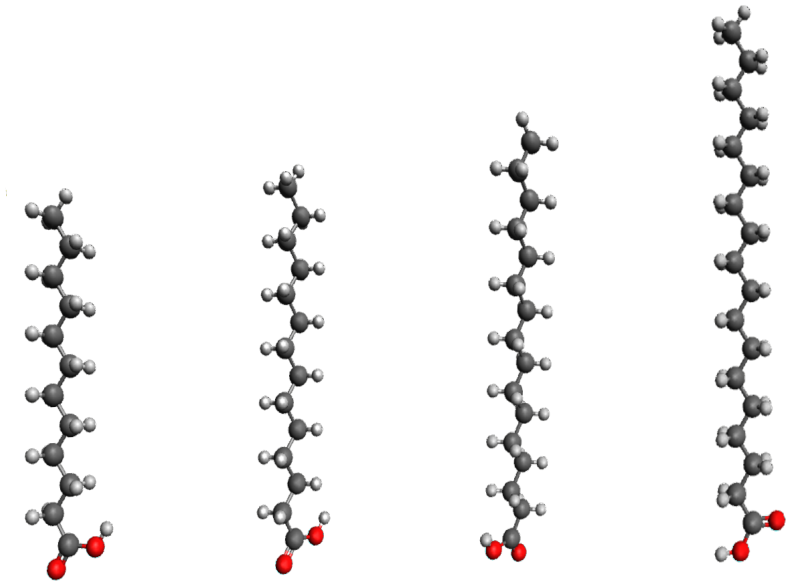

Figure 1.3: Structures of the four most abundant fatty acids in SSA.

Chapter 2

Theory and Instrumentation

2.1 The Liquid-Vapor Interface

The liquid-vapor interface is a chaotic region in which multiple competing processes contribute to its unique chemical and physical properties. Molecules can evaporate from the liquid phase, condensate from the vapor phase, diffuse into the bulk, and diffuse to the surface. The interface is not a discontinuous barrier separating the two phases; rather, the density decreases continuously from the bulk liquid to that of its vapor.[43] Additionally, the interface contains orientational anisotropy in which molecules arrange in particular conformations. This preferential molecular arrangement decreases with increasing distance from the interface such that the bulk is orientationally isotropic.[44]

2.1.1 Surface Tension

Molecules in a liquid phase are surrounded by other molecules in each direction, and these intermolecular interactions lower the overall potential energy of the system. However, molecules positioned at the interface are surrounded by fewer molecules due to the lower molecular density in the adjacent vapor phase (Figure 2.1). Con-

sequently, these interfacial molecules have higher potential energies, and the system must perform work W to move a molecule from the bulk to the surface. Surface energy γ must be spent in order to increase the interfacial area A. This is described the relationship:

$$dW = \gamma dA \tag{2.1}$$

The surface energy can also be defined in terms of the force f opposing the displacement dx of the interface.

$$f dx = \gamma dA \tag{2.2}$$

When both the bulk and interface reach equilibrium, the surface energy is equal to the surface tension.[44–46]

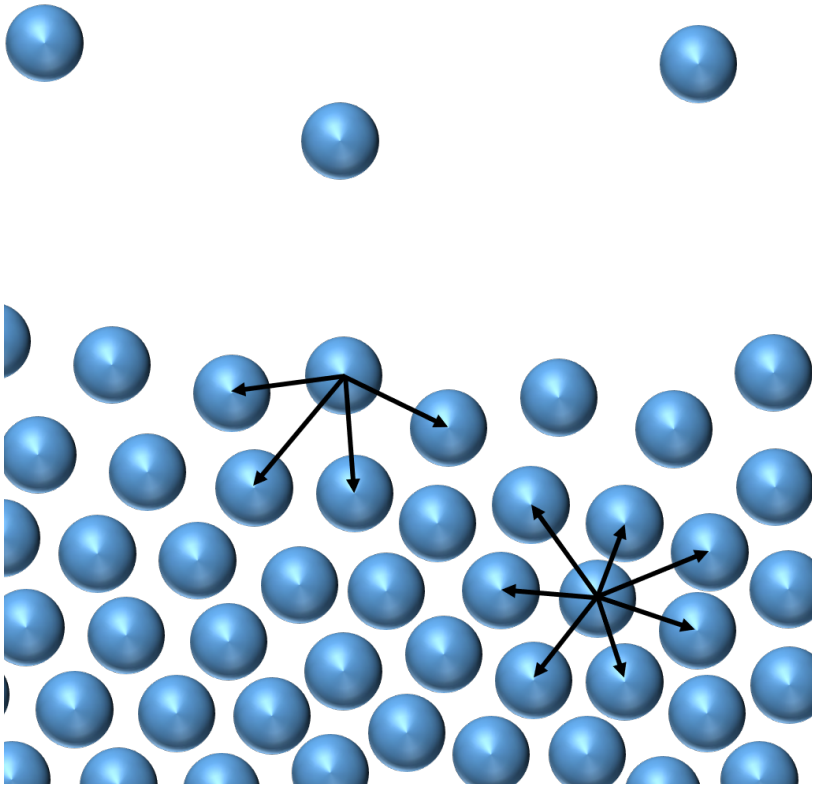

Figure 2.1: Model of a liquid-vapor interface.

2.2 Thermodynamics at the Air-Water Interface

2.2.1 Gibbs Adsorption Equation

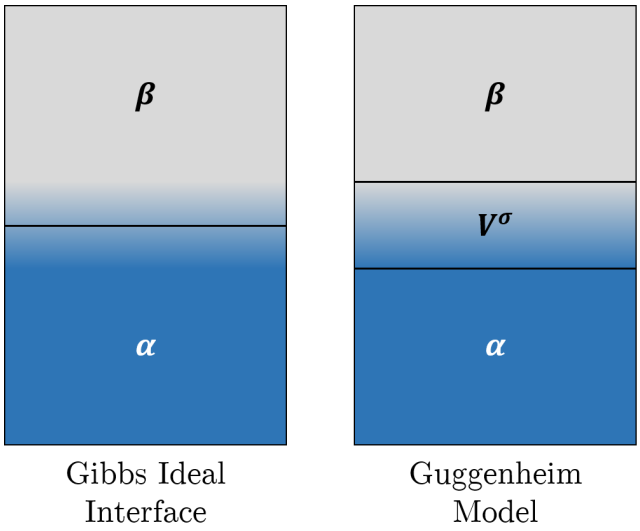

Figure 2.2: Models of an interface between two bulk media.

The interface of two bulk phases of matter yields a region with thermodynamic characteristics distinct from its bulk counterparts. Guggenheim described a model in which an estimated interfacial region volume V^σ is taken into account (Figure 2.2).[47] However, the interfacial region is inhomogeneous and poorly defined. Depth of interfacial anisotropy is highly dependent upon the molecular components of the system, and composition of the interfacial region is nonuniform such that the molar composition of a particular component i as a function of interfacial depth will likely differ from that of another species present in the system. Therefore, the ideal Gibbs model of an infinitesimally thin boundary layer separating two bulk phases α and β, known as the Gibbs dividing surface (GDS), provides a simple yet generally sufficient model for describing thermodynamics at the interface (Figure 2.2).[44]

The ideal Gibbs model can be used to derive an expression relating surface tension and excess interfacial concentrations, known as the Gibbs Adsorption Equation. According to the First Law of Thermodynamics, a variation of the internal energy of

a closed system can be expressed as

$$dU = \delta Q + \delta W \tag{2.3}$$

in which U is internal energy, Q is heat, and W is work. For multicomponent systems, U is function of the extensive variables entropy S, volume V, and number of species N_i:

$$dU = TdS - pdV + \sum_i \mu_i dN_i \tag{2.4}$$

The total internal energy for a system containing two bulk phases α and β and an interfacial plane σ is the sum of the internal energy from each component.

$$U = U^\alpha + U^\beta + U^\sigma \tag{2.5}$$

The extensive variables S, V, and N_i are described equivalently:

$$S = S^\alpha + S^\beta + S^\sigma \tag{2.6}$$

$$V = V^\alpha + V^\beta + V^\sigma \tag{2.7}$$

$$N_i = N_i^\alpha + N_i^\beta + N_i^\sigma \tag{2.8}$$

In the ideal Gibbs model, the GDS is a mathematical plane positioned arbitrarily between α and β. Consequently, its interfacial volume V^σ is zero, so the volume of the system can be simplified to

$$V = V^\alpha + V^\beta \tag{2.9}$$

Thus, the work done by the system dW for the change in volume dV^α and dV^β and

the change in interfacial area dA is expressed as

$$dW = p^{\alpha} dV^{\alpha} + p^{\beta} dV^{\beta} - \gamma dA \tag{2.10}$$

Because the system of interest is planar, then $p^{\alpha} = p^{\beta}$. As a result, the expression for expansion work simplifies:

$$p^{\alpha} dV^{\alpha} + p^{\beta} dV^{\beta} = pdV \tag{2.11}$$

To isolate the interfacial internal energy, Equation 2.5 can be rearranged.

$$dU^{\sigma} = dU - dU^{\alpha} - dU^{\beta} \tag{2.12}$$

Finally, expressions from Equations 2.6 and 2.8 - 2.11 can be plugged into Equation 2.12 to produce

$$dU^{\sigma} = T(dS - dS^{\alpha} - dS^{\beta}) + \gamma dA + \sum_i \mu_i dN_i - \sum_i \mu_i^{\alpha} dN_i^{\alpha} - \sum_i \mu_i^{\beta} dN_i^{\beta} \tag{2.13}$$

Equation 2.13 then condenses into the expression

$$dU^{\sigma} = TdS^{\sigma} + \gamma dA + \sum_i \mu_i dN_i^{\sigma} \tag{2.14}$$

An integrated equation for internal energy can be obtained by integrating Equation 2.14 while keeping the intensive variables T, γ, and μ_i constant.

$$U^{\sigma} = TS^{\sigma} + \gamma A + \sum_i \mu_i N_i^{\sigma} \tag{2.15}$$

Next, a second differential form of interfacial internal energy can be calculated by

differentiating Equation 2.15.

$$dU^{\sigma} = TdS^{\sigma} + S^{\sigma}dT + \gamma dA + Ad\gamma + \sum_i \mu_i dN_i^{\sigma} + \sum_i N_i^{\sigma} d\mu_i \tag{2.16}$$

Combining Equations 2.14 and 2.16 and cancelling like terms yields the following relationship:

$$-Ad\gamma = S^{\sigma}dT + \sum_i N_i^{\sigma} d\mu_i \tag{2.17}$$

Using the definitions of surface excess entropy $S_{\sigma}^{(1)}$ and surface excess concentration Γ_i^{σ},

$$S_{\sigma}^{(1)} = \frac{S^{\sigma}}{A} \tag{2.18}$$

$$\Gamma_i^{\sigma} = \frac{N_i^{\sigma}}{A} \tag{2.19}$$

Equation 2.17 can be divided by A to produce the form of the Gibbs Adsorption Equation.

$$-d\gamma = S_{\sigma}^{(1)}dT + \sum_i \Gamma_i^{\sigma} d\mu_i \tag{2.20}$$

Magnitudes and signs of the surface excess are dependent upon the position of the GDS. However, fixing the GDS such that $N_1 = N_1^{\alpha} + N_1^{\beta}$, where $i = 1$ denotes the solvent, causes N_1^{σ} to equal zero. Therefore, Γ_1^{σ} is also equal to zero. This redefines the surface such that the interfacial excesses of all other components are relative to the solvent, so Equation 2.20 can be rewritten as

$$-d\gamma = S_{\sigma}^{(1)}dT + \sum_{i=1}^{i} \Gamma_i^{1} d\mu_i \tag{2.21}$$

A simple example of the application of the Gibbs Adsorption Equation is a two-component system containing a solvent, $i = 1$, and a solute, $i = 2$. Assuming constant

temperature, the Gibbs adsorption isotherm is described as

$$d\gamma = -\Gamma_1 d\mu_1 - \Gamma_2 d\mu_2 \tag{2.22}$$

Because the GDS is positioned such that $\Gamma_1 = 0$, then Equation 2.22 can be simplified to

$$d\gamma = -\Gamma_2^{(1)} d\mu_2 \tag{2.23}$$

The chemical potential of the solute can be expressed as

$$\mu_2 = \mu_2^0 + RT \ln \frac{a}{a_0} \tag{2.24}$$

in which a is its activity and a_0 is the standard activity. Differentiating Equation 2.24 with respect to a/a_0 at constant temperature yields the relationship

$$d\mu_2 = RT \frac{d(a/a_0)}{a/a_0} = RT \frac{da}{a} \tag{2.25}$$

Substituting the expression in Equation 2.25 into 2.23 produces

$$\Gamma_2^{(1)} = -\frac{a}{RT} \frac{\delta\gamma}{\delta a}\bigg|_T \tag{2.26}$$

This equation is significant because it describes the magnitude of solute enrichment at the surface as a function of the experimentally measurable parameters solute concentration and changes in surface tension. When $\Gamma_2^{(1)} > 0$, meaning that the solute is enriched at the interface, then the surface tension will decrease with increasing solute concentration. Alternatively, when the solute is depleted from the interface ($\Gamma_2^{(1)} < 0$), then the surface tension increases with increasing solute concentration.

2.2.2 Relative Surface Excess

While the surface excess relationship (Eq. 2.26) defined in the previous section is useful, the requirement of the arbitrary placement of the GDS decreases its utility. A relative surface excess quantity independent of GDS position can be derived from the Gibbs-Duhem equations for bulk phases α and β, respectively

$$-V^{\alpha}dp + S^{\alpha}dT + \sum_i N_i^{\alpha} d\mu_i = 0 \tag{2.27}$$

$$-V^{\beta}dp + S^{\beta}dT + \sum_i N_i^{\beta} d\mu_i = 0 \tag{2.28}$$

At equilibrium, the intensive variables T, p, and μ_i must be the same for α and β. Consequently, Equations 2.27 and 2.28 can be rewritten as

$$V^{\alpha}dp = S^{\alpha}dT + \sum_i N_i^{\alpha} d\mu_i \tag{2.29}$$

$$V^{\beta}dp = S^{\beta}dT + \sum_i N_i^{\beta} d\mu_i \tag{2.30}$$

Dividing Equations 2.29 and 2.30 by their respective volumes yields expressions for dp that can be equated.

$$\frac{S^{\alpha}}{V^{\alpha}}dT + \sum_i \frac{N_i^{\alpha}}{V^{\alpha}} d\mu_i = \frac{S^{\beta}}{V^{\beta}}dT + \sum_i \frac{N_i^{\beta}}{V^{\beta}} d\mu_i \tag{2.31}$$

Quantities of entropy per unit volume and number of species i per unit volume can be defined as entropy density s and concentration c, respectively.

$$s = \frac{S}{V} \tag{2.32}$$

$$c = \frac{n_i}{V} \tag{2.33}$$

Plugging Equations 2.32 and 2.33 into Equation 2.31, expanding the sums, and reorganizing the expressions algebraically leads to

$$-d\mu_1 = \frac{s^\alpha - s^\beta}{c_1^\alpha - c_1^\beta} dT + \cdots + \frac{c_i^\alpha - c_i^\beta}{c_1^\alpha - c_1^\beta} d\mu_i \tag{2.34}$$

Then, plugging 2.34 into the expanded Gibbs adsorption equation (Eq. 2.20) yields

$$-d\gamma = S_\sigma^{(1)} dT - \Gamma_1^\sigma \left[\frac{s^\alpha - s^\beta}{c_1^\alpha - c_1^\beta} dT + \cdots + \frac{c_i^\alpha - c_i^\beta}{c_1^\alpha - c_1^\beta} d\mu_i \right] + \cdots + \Gamma_i^\sigma d\mu_i \tag{2.35}$$

Rearranging Equation eq:32a produces a form of the Gibbs adsorption equation exactly similar to the form of Equation 2.20.

$$-d\gamma = \left(S_\sigma^{(1)} - \Gamma_1^\sigma \frac{s^\alpha - s^\beta}{c_1^\alpha - c_1^\beta} \right) dT + \cdots + \left(-\Gamma_1^\sigma \frac{c_i^\alpha - c_i^\beta}{c_1^\alpha - c_1^\beta} + \Gamma_i^\sigma \right) d\mu_i \tag{2.36}$$

This equation is significant because it does not require the GDS to be fixed at $\Gamma_1^\sigma = 0$. As such, the relative excess functions for entropy and concentration are as follows:

$$S_\sigma^1 = S_\sigma^{(1)} - \Gamma_1^\sigma \frac{s^\alpha - s^\beta}{c_1^\alpha - c_1^\beta} \tag{2.37}$$

$$\Gamma_i^1 = \Gamma_i^\sigma - \Gamma_1^\sigma \frac{c_i^\alpha - c_i^\beta}{c_1^\alpha - c_1^\beta} \tag{2.38}$$

Furthermore, Equation 2.38 can be transformed to include only terms that are meaningful in a real air-water interfacial system. An isotropic composition in α and β is assumed up until the GDS at which point the composition changes, so the number of ith molecules at the surface N_i^σ can be expressed as

$$N_i^\sigma = N_i - N_i^\alpha - N_i^\beta \tag{2.39}$$

The mass balance equation representing the number of i molecules at the interface

can be described using concentrations of the bulk phases, c_i^α and c_i^β, multiplied by their volumes V_i^α and V_i^β, respectively to yield the number of i molecules in each bulk phase.

$$N_i^\sigma = N_i - c_i^\alpha V_i^\alpha - c_i^\beta V_i^\beta \tag{2.40}$$

For a multicomponent system, such as a liquid with dissolved solutes, the relationship $V^\alpha = V - V^\beta$ can be substituted into the mass balance equation for the solvent $i = 1$.

$$N_1^\sigma = N_1 - c_1^\alpha V + (c_1^\alpha - c_1^\beta)V^\beta \tag{2.41}$$

All other components are treated analogously:

$$N_i^\sigma = N_i - c_i^\alpha V + (c_i^\alpha - c_i^\beta)V^\beta \tag{2.42}$$

Only V^β depends on the position of the GDS, so the GDS position dependence can be removed by solving for V^β in Equation 2.41.

$$V^\beta = \frac{N_1^\sigma - N_1 + c_1^\alpha V}{c_1^\alpha - c_1^\beta} \tag{2.43}$$

Next, plugging Equation 2.43 into 2.42 and reorganizing algebraically produces

$$N_i^\sigma - N_1^\sigma \frac{c_i^\alpha - c_i^\beta}{c_1^\alpha - c_1^\beta} = \left(N_i - N_1 \frac{c_i^\alpha - c_i^\beta}{c_1^\alpha - c_1^\beta}\right) - V\left(c_i^\alpha - c_1^\alpha \frac{c_i^\alpha - c_i^\beta}{c_1^\alpha - c_1^\beta}\right) \tag{2.44}$$

Using the definition of surface excess concentration (Eq. 2.19), Equation 2.44 can be divided by A to obtain the relative adsorption of component i with respect to component 1:

$$\Gamma_i^1 = \frac{1}{A}\left[\left(N_i - N_1 \frac{c_i^\alpha - c_i^\beta}{c_1^\alpha - c_1^\beta}\right) - V\left(c_i^\alpha - c_1^\alpha \frac{c_i^\alpha - c_i^\beta}{c_1^\alpha - c_1^\beta}\right)\right] \tag{2.45}$$

All terms on the right side of the equation can refer to a real air-water interface. Subsequently, the relative surface excess concentration can be determined experimentally by measuring the surface tension as a function of solute concentration.

2.3 Experimental Tensiometry Methods

The Langmuir-Wilhelmy balance method is the most common tensiometry technique, and it was the method used in this particular study (Figure 2.3). Generally, a Langmuir trough coated in a hydrophobic substance, such as polytetrafluoroethylene (PTFE), is filled with an aqueous solution, known as the subphase. Two hydrophilic barriers are placed on top of the trough, and their compression rate can be carefully controlled. A Langmuir film is deposited on the subphase by dissolving the sample in a volatile organic solvent and spreading it dropwise on the aqueous surface. Following solvent evaporation, a single-molecule-thick film remains. The barriers compress the monolayer, and the changes in film surface pressure are measured with a Wilhelmy plate tensiometer. Surface pressure is related to surface tension by the relationship

$$\pi = \gamma_0 - \gamma_f \tag{2.46}$$

in which γ_0 is the surface tension of the bare subphase and γ_f is the surface tension of the film-covered subphase. There is also a force from barrier compression that contributes to the monolayer surface pressure; this term is often neglected.[44–46]

The Wilhelmy plate is used as a probe to measure the air-liquid surface tension. It is a thin plate normally a few square centimeters in area, and the material used for the Wilhelmy plate is unimportant as long as it can be completely wetted by the subphase. Normally, platinum is used because of its low reactivity, ease of cleaning, and durability. Filter paper can also be cut into a Wilhelmy plate and thrown away after an experiment. The plate is then attached to the tensiometer via a thin wire,

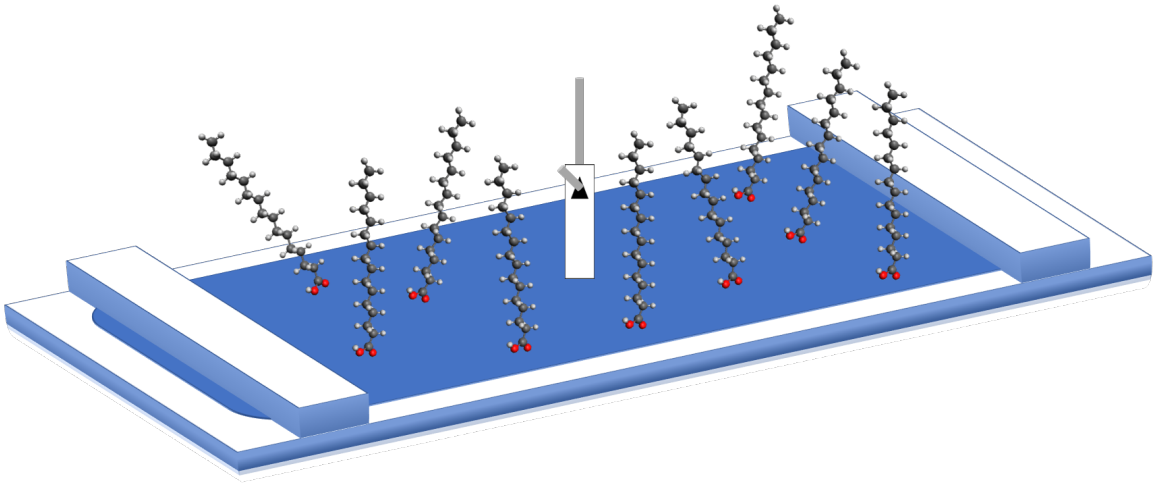

Figure 2.3: Wilhelmy plate method on a Langmuir trough.

and it is placed on the liquid such that it only makes contact with the subphase surface. The sum of the forces acting upon the Wilhelmy plate include gravity F_g, buoyancy F_b, and surface tension γ which can be expressed as

$$\begin{aligned} F_{net} &= F_g + F_b + \gamma \\ &= \rho_p lwt + 2\gamma(t+w)\cos\theta - \rho_0 gtwh \end{aligned} \tag{2.47}$$

In the above equation, ρ_p is the density of the Wilhelmy plate, l is the length of the plate, w is the width of the plate, t is the thickness of the plate, γ is the surface tension, θ is the contact angle between the subphase and the plate, ρ_0 is the density of the subphase, and h is the depth of plate immersion into the subphase. Assuming complete wetting where $\theta = 0$, the net downward force from a subphase and a monolayer-covered subphase can be measured and plugged into Equation 2.46.[45]

The Wilhelmy plate is a particularly appealing probe for force tensiometry because it is accurate and can be used for both static and dynamic surface tension measurements. Other probes can also be used, such as the Du Noüy ring and a platinum rod, but they have particular limitations. The Du Noüy ring is a platinum ring that is submerged into the interface by translating the stage supporting the liquid sub-

phase container. The ring is then pulled up from the subphase, pulling the meniscus along with it. Before the meniscus separates from the ring, the force exerted on the meniscus reaches a maximum value which is used to calculate static surface tension. Empirical correction factors must be applied to account for the finite diameter of the ring, and the density of the liquid must be known in order to implement the correction factors.[45,46,48,49] Unlike the Wilhelmy plate and the Du Noüy ring, a platinum rod can be used to measure static and dynamic surface tension of small volumes. However, the accuracy of a force tensiometry method is dependent upon the probe geometry accuracy, so a small probe is prone to larger percent error values.[50]

2.4 Thin Films on Liquid Surfaces

Organic compounds with the formula $C_nH_{2n+1}X$, in which X corresponds to a polar functional group, are surface active compounds that adsorb to the air-water interface from the aqueous subphase to form a Gibbs monolayer. Increasing the alkyl chain length decreases solubility in water such that non-ionized amphiphiles consisting of greater than 12 carbon atoms are nearly insoluble in aqueous solutions. These insoluble molecules can spread across the air-water interface and form a monolayer when the interactions between the organic compounds and the water are stronger than the interactions between the organic compounds themselves. Thus, a single-molecule thick film, called a Langmuir monolayer, is formed when the interfacial area is large enough for all of the molecules spread onto the aqueous surface.[45,46,51]

2.4.1 Monolayer Phases

Molecular confinement at the air-water interface due to slow desorption or evaporation yields two-dimensional phase behavior analogous to three-dimensional phase behavior in bulk matter. Monolayers can undergo transitions between gaseous, liquid, and

solid phases upon changes in temperature and interfacial area. Like in bulk media, the phase behavior is dictated by the strength of intermolecular interactions. Reduction of mean molecular area (MMA) at the surface increases the surface pressure of the monolayer until steric repulsion between amphiphiles overcomes their attractive interactions, causing monolayer collapse (Figure 2.4). The change in surface pressure as a function of MMA provides information on the nature of the intermolecular interactions between the amphiphiles themselves and their interactions with the aqueous subphase. Surface pressure-area isotherms also describe monolayer packing and stability.[44–46]

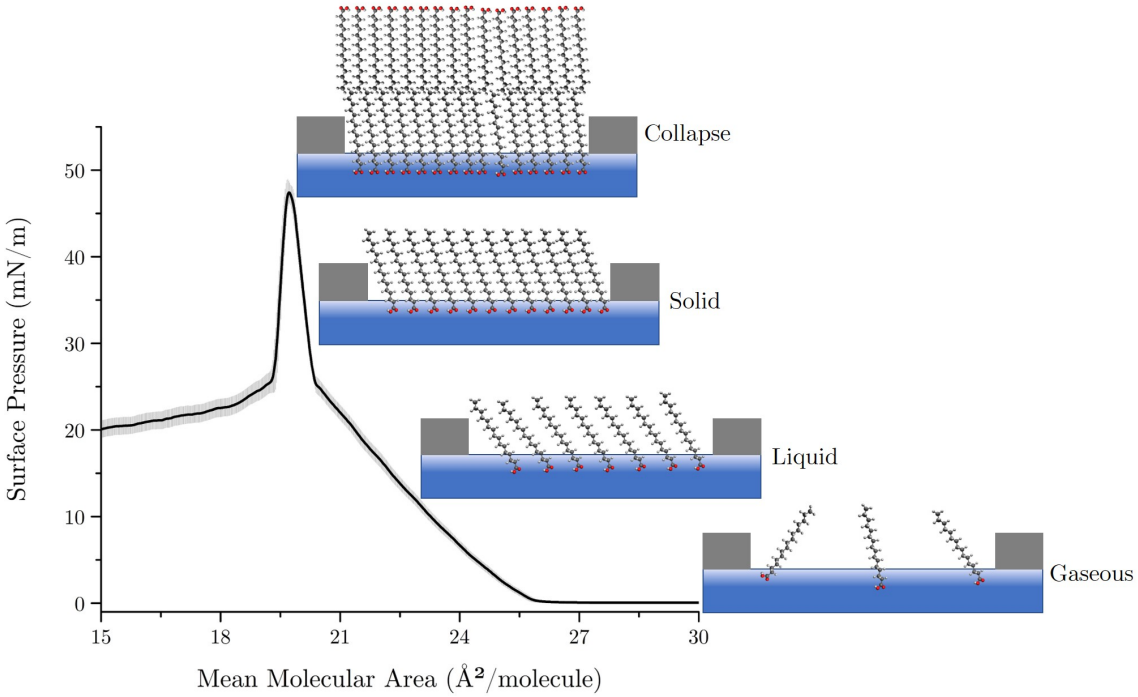

Figure 2.4: States and phase transitions of a palmitic acid monolayer at the air-water interface.

Gaseous films consist of amphiphilic molecules that have minimal van der Waals interactions between the aliphatic tails due to the large intermolecular distances. The aliphatic tilt angle relative to surface normal is the largest in this phase.[52–55] However, the interactions between the polar lipid headgroups and polar water subphase are strong enough to prevent film vaporization, and the aliphatic chains are generally

sufficiently hydrophobic to prevent desorption into the bulk aqueous subphase. At the interface, film molecules have two translational degrees of freedom, and the average kinetic energy for each degree of freedom is $\frac{1}{2}k_BT$. Thus, an ideal film in the gaseous phase behaves according to the two-dimensional ideal gas equation in which π is the surface pressure and A is the area/molecule.

$$\pi A = k_B T \tag{2.48}$$

Because A is very large in this phase, $\pi < 0.50$ mN/m.[45,46]

As the thin film is compressed further to smaller mean molecular area (MMA) values, the surface pressure begins to rise at the gas-liquid phase transition, referred to as the lift-off point. The liquid phase is characterized by increased lateral interactions between amphiphiles. For more fluid monolayers, the film can experience an additional transition from a liquid-expanded (LE) phase to a liquid-condensed (LC) phase. The LE phase occurs at MMA values much larger than the size of the molecule itself, so the headgroups are well hydrated. Lateral interactions between aliphatic chains are minimal due to low packing order. This phase can be described by a two-dimensional van der Waals equation of state that takes both the finite size of molecules and their attractive potentials into account.

$$\left(\pi + \frac{a_v}{A^2}\right)(A - b) = k_B T \tag{2.49}$$

In Equation 2.49 a_v and b are constants, k_B is the Boltzmann constant, and T is temperature. More specifically, these constants can be mathematically defined as

$$a_v = \frac{\pi C N_0^2}{4\sigma_d^4} \tag{2.50}$$

$$b = \frac{1}{2}\pi N_0 \sigma_d^2 \tag{2.51}$$

in which C is the London dispersion force coefficient, N_0 is the number of molecules, and σ_d is the diameter of the molecule modeled as a hard sphere. Thus, a_v is the van der Waals constant that parameterizes the strength of the attractive potential, and b represents the excluded or unavailable area per mole of molecules.[56]

Compression induces the subsequent first-order phase transition into the LC phase in which long-range molecular order is observed. Both alkyl chain tilt angles and headgroup hydration decrease to accommodate for tighter packing at the interface. The final transition into the solid phase leads to a precipitous increase in surface pressure with decreasing MMA caused by the steric repulsion between the headgroups. The alkyl chains are arranged in their tightest conformation, and the headgroups are largely dehydrated. Extrapolation of the isotherm slope in the solid phase to a surface pressure of 0 mN/m yields an MMA that corresponds to the molecular cross-section in the solid phase.[44–46]

The point at which the monolayer can no longer be compressed is known as the collapse. Eventually steric repulsion between molecules in the monolayer destabilizes the two-dimensional nature of the film such that three-dimensional structures are produced. The maximum surface pressure (or minimal surface tension) at which a film can exist is determined by its rigidity. Fluid monolayers have low collapse pressures and often lose material by desorption into the aqueous subphase. Rigid or highly ordered monolayers generally have higher collapse pressures, and these films tend to collapse via fracturing in which material is lost either by forming multilayer aggregates in the air phase or by desorption into the aqueous phase. The third collapse mechanism, known as folding, requires an intermediate rigidity to allow the monolayer to buckle and form protrusions into the subphase. These protrusions occur at random defects in the monolayer which act as folding nucleation sites, and the protrusions coexist with the monolayer. Continuous compression after protrusion formation increases the fraction of monolayer in the folds relative to the flat regions

so that constant collapse surface pressure is maintained. The monolayer integrity remains intact such that the process is reversible upon increase in interfacial area, unlike film desorption and fracturing which are irreversible processes.[57–59]

2.4.2 Mixed Monolayers

Both Gibbs and Langmuir monolayers can consist of one or multiple species of amphiphiles. The intermolecular interactions between the different molecules in the monolayer are of particular interest due to their role in determining interfacial organization and behavior. Monolayer mixtures produce different surface behavior than their individual counterparts. The interactions between the amphiphile headgroups cause the molecules to attract or repulse one another, depending upon their charge. As a result, deviations from ideality are largely from the headgroup interactions rather than the aliphatic chain interactions.[51]

Interactions between molecules in a Langmuir film can be examined via their miscibility and stability within the monolayer. The amphiphiles can be completely miscible, partially miscible, or immiscible (Figure 2.5).[45,51] Immiscible mixtures can be thought of as separate monolayers in equilibrium with one another because the individual components will form segregated domains. The total area per molecule of an immiscible mixed film A_{12} measured at a particular surface pressure can be expressed as a function of its monolayer components:

$$A_{12} = X_1 A_1 + X_2 A_2 \tag{2.52}$$

Variables X_1 and X_2 are the mole fractions of each type of amphiphile, and A_1 and A_2 are the corresponding mean molecular area values for the single components at the same surface pressure as the mixture. Equation 2.52 is also obeyed when the components form an ideal mixture. Positive deviations from a linear fit are indicative

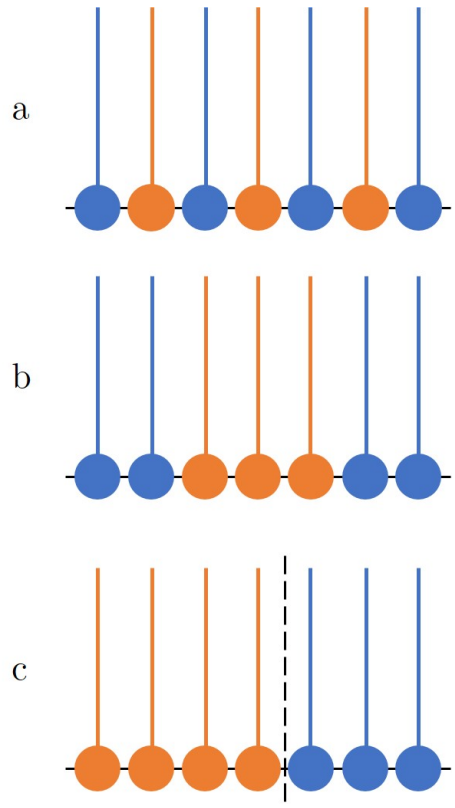

Figure 2.5: Possible molecular arrangements in a mixed monolayer. (a) Miscible, homogeneous mixed monolayer; (b) immiscible, non-homogeneous mixed monolayer; (c) immiscible, complete separation of monolayer components.

of repulsive interactions between the amphiphiles, and negative deviations suggest attractive interactions which facilitate monolayer compression. A combination of regions of linear fits and deviations from Equation 2.52 indicate partial film miscibility.[51]

A similar additivity relationship exists for the mixture surface pressure π_{12} measured at a particular mean molecular area

$$\pi_{12} = X_1\pi_1 + X_2\pi_2 \tag{2.53}$$

in which π_1 and π_2 are the surface pressures of the single components. A linear fit to this relationship indicates either an ideal two-dimensional mixture or monolayer immiscibility, and deviations from linearity suggest interactions between the different

amphiphiles. Additionally, immiscible monolayers have multiple collapse points corresponding to each component in the mixture. Miscible monolayers have a collapse pressure that is dependent upon the molar fraction of each component in the mixture; thus, the monolayer mixture collapse occurs at a pressure between that of its individual components.[45,51]

Mixed Langmuir films can also be described by excess thermodynamic functions. The Gibbs excess free energy of mixing ΔG^{exc} can be used to quantify film stability. In the case of nonideal mixing, Equation 2.52 can be rewritten in terms of the excess area of mixing A^{exc}:

$$A^{exc} = A_{12} - (X_1 A_1 + X_2 A_2) \tag{2.54}$$

A^{exc} is positive when the monolayer expands upon mixing, A^{exc} is negative when the monolayer contracts, and $A^{exc} = 0$ when the components are immiscible or mix ideally. Then ΔG^{exc} can be determined directly from surface pressure-area isotherms using the calculated A^{exc} value.

$$\Delta G^{exc} = \int_0^{\pi} A^{exc} d\pi \tag{2.55}$$

A negative ΔG^{exc} is indicative of monolayer stability, and a positive value suggests plane separation in the monolayer. Finally, the total free energy of mixing ΔG^{M} can be determined from the sum

$$\Delta G^{M} = \Delta G^{exc} + \Delta G^{id} \tag{2.56}$$

in which ΔG^{id} is the ideal Gibbs free energy of mixing, described by the relationship

$$\Delta G^{id} = RT(X_1 \ln X_1 + X_2 \ln X_2) \tag{2.57}$$

The mixed monolayer is more thermodynamically stable than its individual counter-

parts if ΔG^M is negative.[51]

Chapter 3

Experimental

3.1 Aqueous Subphase Preparation

Ultrapure water obtained from a Milli-Q Advantage A10 system (18.2 MΩ·cm) was used for all surface pressure-area isotherm aqueous subphases. To create the model seawater solution, NaCl (Sodium chloride, 99+%, ACS reagent, Acrōs Organics) was baked at 650° C in a furnace (Fisher Scientific Isotemp® Muffle Furnace) for at least 10 hours to remove any residual organics. Both pure water and 0.4 M NaCl solutions had a pH of 5.6 due to acidification by atmospheric CO_2. Acidic subphases were prepared at pH 2.0 via the addition of HCl (Hydrochloride Acid, TraceMetal Grade, Fisher Scientific). Only the 0.4 M NaCl solution could be adjusted to pH 8.2 via NaOH (Sodium Hydroxide Pellets, Mallinckrodt Analytical Reagent) addition. A basic water subphase rapidly acidified when exposed to laboratory air. The 0.4 M NaCl solution acidified more slowly over time; therefore, the solution was initially prepared at pH 8.5 so that the pH would drop to 8.2 when the tensiometer was recording data. All pH measurements were collected using an Orion VersaStar Pro Advanced Electrochemistry Meter (Thermo Scientific) and an Orion ROSS Ultra pH/ATC triode (Thermo Scientific) with an error of ±0.1 pH units.

3.2 Lipid Solution Preparation

Stearic acid ($\geq$ 99%, Sigma), palmitic acid ($\geq$ 99%, Sigma), myristic acid ($\geq$ 99%, Sigma), and lauric acid (99%, Acrōs Organics) were used without any further purification. Each lipid was dissolved in chloroform (HPLC Grade, Fisher Chemical) at a concentration of 3 mM. The concentrations of palmitic acid and stearic acid were calibrated by performing surface pressure-area isotherms on water at pH 5.6 and adjusting the concentrations until the lift-off points occurred at 26 and 24 Å^2/molecule, respectively. The myristic acid concentration was calibrated via a surface pressure-area isotherm on water at pH 2.0 to minimize desorption into the subphase; its concentration was adjusted such that the lift-off point occurred at 55 Å^2/molecule. Lauric acid could not be calibrated with a surface pressure-area isotherm because of its solubility, so its concentration was determined using the mass (Mettler Toledo XS104 Analytical Balance) added to the chloroform.

The fatty acid mixtures were prepared using the individual fatty acid solutions described above. All mixtures consisted of molar ratios of their respective components (1 lauric acid : 2 myristic acid : 4 palmitic acid : 3 stearic acid, 2 myristic acid : 4 palmitic acid : 3 stearic acid, and 1 lauric acid : 9 stearic acid). The individual fatty acid concentrations were used to calculate the volume required to make approximately 15 mL of the mixture solution, and all mixtures were created in duplicate. Aliquots of the individual lipid solutions were transferred using a micropipette (FisherBrand® Elite).

3.3 Surface Pressure-Area Isotherms

Surface pressure-area isotherms were measured on a Teflon Langmuir trough (KSV NIMA) with an attached tensiometer and Delrin® barriers (KSV NIMA). Both the trough and barriers were thoroughly cleaned with reagent alcohol (Histological Grade,

Fisher Chemical) and ultrapure water. Surface pressure was measured as a function of mean molecular area (MMA) using a filter paper plate (Ashless, Whatman™) to serve as the Wilhelmy plate, and the paper plate was fully wetted before running an isotherm. To check for surface cleanliness prior to beginning an experiment, the trough was filled with its aqueous subphase and compressed at the maximum compression speed (270 mm/min/barrier) to check for any significant rise in surface pressure ($\leq$ 0.20 mN/m). A microsyringe (50 μL, Hamilton®) was used to spread the lipid solution dropwise onto the aqueous subphase, and 10 minutes were allowed for the chloroform to evaporate after spreading. The monolayer was symmetrically compressed at a rate of 10 mm/minute (5 mm/minute per barrier). All surface pressure-area isotherms were completed in triplicate and were conducted at 21.6° C ($\pm$ 1.0° C).

Chapter 4

Results and Discussion

The goal of this project is to study a sea spray aerosol (SSA) surface proxy in order to understand how the presence of soluble organic surfactants impacts the monolayer organization and behavior. It is hypothesized that the long-chain fatty acids will stabilize the soluble short-chain fatty acids at the air-water interface via increased dispersion interactions between the alkyl chains. Therefore, surface pressure-area isotherms (Π-A) of the 1 lauric acid (C_{12}) : 2 myristic acid (C_{14}) : 4 palmitic acid (C_{16}) : 3 stearic acid (C_{18}) SSA proxy mixture were conducted on pure water and 0.4 M NaCl aqueous subphases. The solution pH was adjusted to mimic nascent SSA and acidified SSA in the marine boundary layer.

4.1 Surface Pressure-Area Isotherms

4.1.1 Individual Fatty Acid Surface Pressure-Area Isotherms

Surface pressure-area isotherms of the individual saturated fatty acids were measured in order to understand their phase behavior on various aqueous subphases (Figures 4.1 - 4.10). The interfacial behavior of myristic acid,[60–65] palmitic acid,[66–71] and stearic acid[72–76] have been extensively documented in the literature. Lauric acid is

partially soluble such that it does not form a stable Langmuir monolayer at the air-water interface.[77] Therefore, a full lauric acid isotherm could not be obtained due to desorption into the subphase (Figures A.1 and A.2).

Myristic acid is also partially soluble in water, and the desorption kinetics of lauric and myristic acid were thoroughly described by Ter Minassian-Saraga[77] and Cornwell.[78] During the first few minutes after spreading into the gaseous phase, there was rapid film loss into the subphase. Later desorption could be described by the relationship

$$\log N_t = -kt + c \tag{4.1}$$

in which N_t is the number of molecules in the film at time t, and c is a constant. The desorption rate of surface active amphiphiles is dependent upon their size, functional groups, protonation state, and strength of intermolecular interactions between other amphiphiles in the monolayer.[45] Therefore, the film desorption rate is expected to be greatest in the gaseous phase due to weaker dispersion interactions between the aliphatic moieties. Charged films have increased solubility in aqueous subphases, thereby increasing their rates of desorption. Ionized amphiphiles interact more strongly with the underlying water molecules, and the free energy decrease caused by removal of the charged molecules from the surface region of high electrical potential yields more energetically favorable dissolution. Additionally, electrostatic repulsion between the ionized headgroups yields a more expanded monolayer, further increasing the rate of desorption.

The different phase behaviors in Figures 4.1 - 4.4 are a consequence of that desorption into the bulk aqueous phase. Myristic acid is fully protonated at pH 2.0 based on the surface pK_a value of 7.88 at 20° C,[79] so its solubility is minimized in Figure 4.2. As a result, its desorption kinetics are slow, so myristic acid is most surface active at pH 2.0. For this reason, myristic acid spread on water at pH 2.0 has the highest lift-off point at 55 Å^2/molecule.[80] At pH 5.6, myristic acid is partially

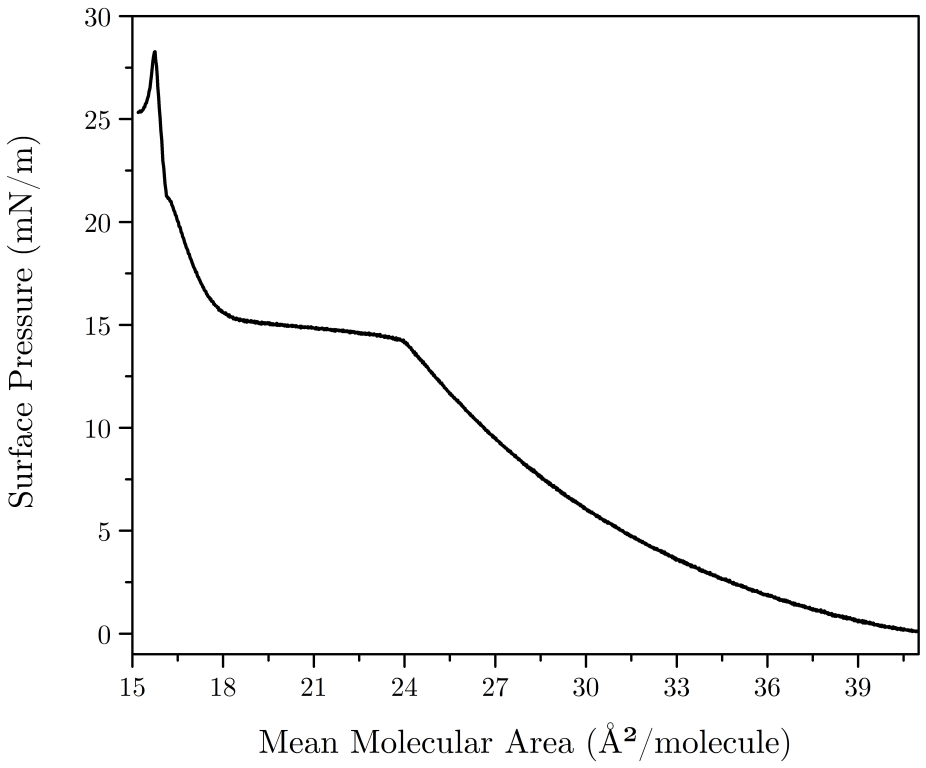

Figure 4.1: Π-A isotherm of myristic acid on ultrapure water at pH 5.6.

deprotonated, meaning that more of the fatty acid desorbs into the subphase over the course of the isotherm experiment.[81] Because there are fewer amphiphiles present at the surface, the lift-off points in Figures 4.1 and 4.4 are lower at 41 Å^2/molecule. Myristic acid is largely deprotonated at pH 8.2, so its rate of desorption increases such that a stable monolayer cannot be obtained for the model seawater subphase in Figure 4.3. Increasing the amount of fatty acid spread onto the air-water interface helps to overcome the diffusion-mediated desorption, but the lateral barrier compression during the experiment promotes desorption due to mechanical forcing. Hence, monolayer collapse cannot be reached.

The shorter aliphatic chain length in myristic acid yields a smaller sum of dispersion interactions between the lipids, meaning that myristic acid films at the air-water interface are more disordered and pack less tightly.[45,82,83] Thus, the films are highly

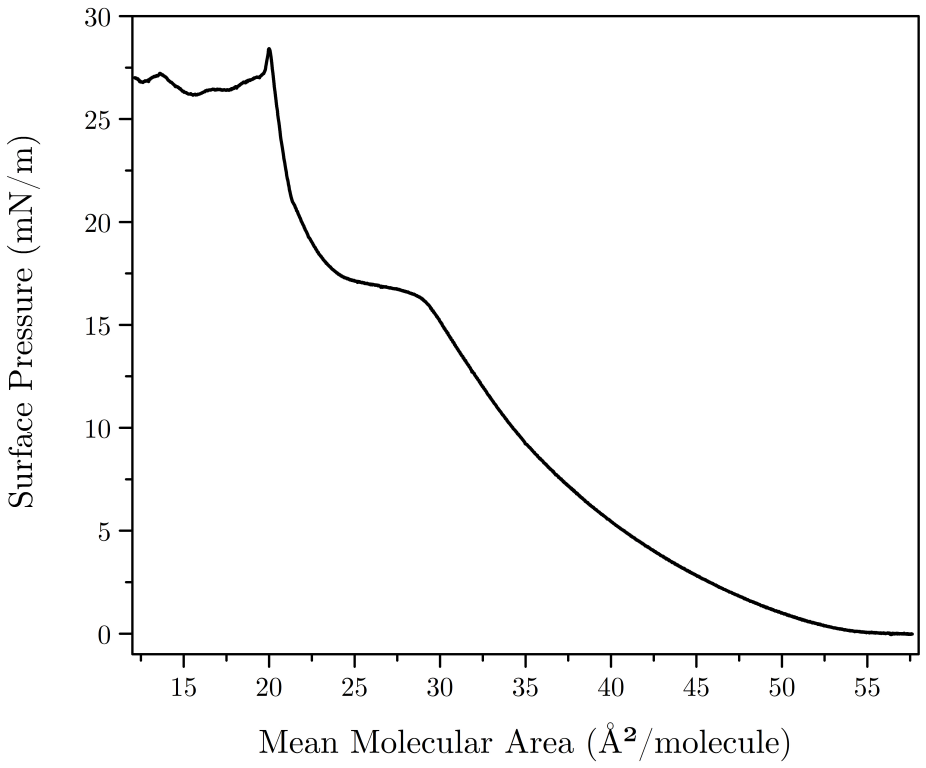

Figure 4.2: Π-*A* isotherm of myristic acid on ultrapure water at pH 2.0

compressible, as demonstrated by the smooth phase transitions and the gradual rise in surface pressure throughout the isotherms. Further evidence for high compressibility is found in the liquid-expanded (LE) phase which persists for a large range in mean molecular area (MMA). In Figure 4.1, the LE phase occurs between 24 and 41 Å^2/molecule; addition of NaCl at the same pH (Figure 4.4) slightly changes the LE phase range to 26 - 41 Å^2/molecule. Thus, the salt either helps to organize the lipids into a more compact arrangement or reduces the lipid solubility via interactions with the carboxyl headgroups. Myristic acid at pH 2.0 (Figure 4.2) has an even wider LE phase range between 29 and 55 Å^2/molecule which is a likely consequence of the decreased solubility at large MMA values.

Myristic acid does not exhibit a direct LE to liquid-condensed (LC) phase change; rather, an LE/LC coexistence region[84,85] is observed as a surface pressure plateau

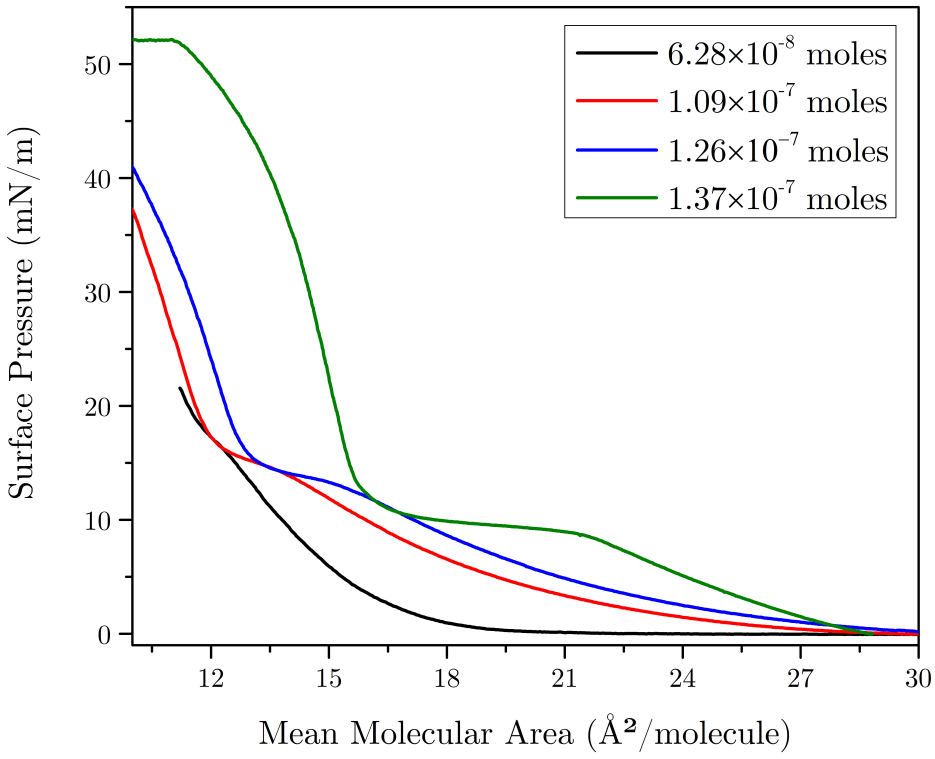

Figure 4.3: Π-*A* isotherms of myristic acid on aqueous 0.4 M NaCl at pH 8.2.

at 15 mN/m in Figures 4.1 and 4.4 and at 17 mN/m in Figure 4.2. The LE/LC phase occurs between 18 and 24 Å^2/molecule for myristic acid on water at pH 5.6 (Figure 4.1) and between 20 and 26 Å^2/molecule for an NaCl solution at the same pH (Figure 4.4). While the presence of salt affects the MMA at which this coexistence phase occurs, it does not change the phase MMA range. At pH 2.0 (Figure 4.2), the LE/LC phase is measured from 24 - 29 Å^2/molecule. Therefore, it appears as though the LE/LC MMA range is dependent upon myristic acid solubility on each aqueous subphase, with decreasing solubility corresponding to higher MMA values.

A distinct LC - solid (S) phase transition is observed in myristic acid isotherms conducted on water. At pH 5.6 (Figure 4.1), the transition occurs at 16 Å^2/molecule; at pH 2.0 (Figure 4.2), the transition occurs at 21.5 Å^2/molecule. Both transitions are measured at 21.5 mN/m. The S phase is particularly short-lived because both

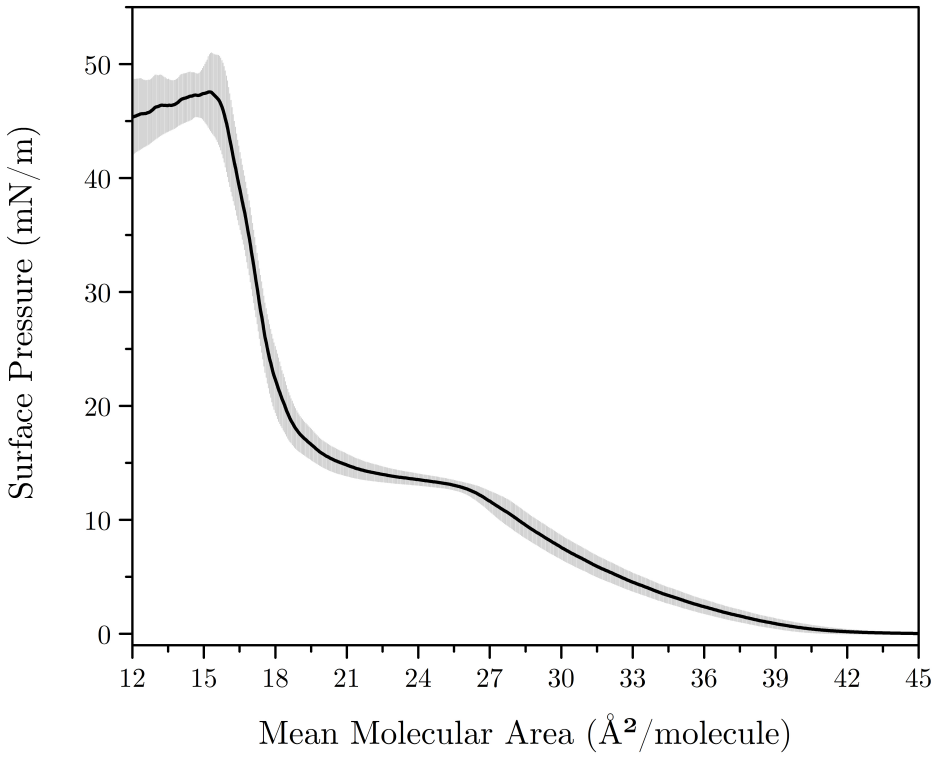

Figure 4.4: Π-A isotherms of myristic acid on aqueous 0.4 M NaCl at pH 5.6.

isotherms collapse at 28.5 mN/m. The MMA at collapse is 16.5 Å^2/molecule at pH 5.6 and 20 Å^2/molecule at pH 2.0; a greater MMA at lower pH is caused by decreased desorption kinetics. NaCl changes the condensed phase behavior such that a LC-S phase transition is not measured. Instead, the surface pressure increases linearly between 20 and 16.5 Å^2/molecule. The collapse pressure is measured at 47.5 mN/m, so NaCl significantly stabilizes the condensed monolayer at higher surface pressures.

Palmitic acid is highly surface active because of the strong dispersion interactions between the aliphatic chains, and its desorption kinetics into the bulk aqueous phase are slow when fully protonated. The surface pK_a of palmitic acid is 8.34 at 20° C, so the thin film is fully protonated at pH 5.6. At the pH of seawater, palmitic acid is partially deprotonated, meaning that some of the film is expected to desorb into the subphase throughout the course of an isotherm experiment. However, Na^+ ions

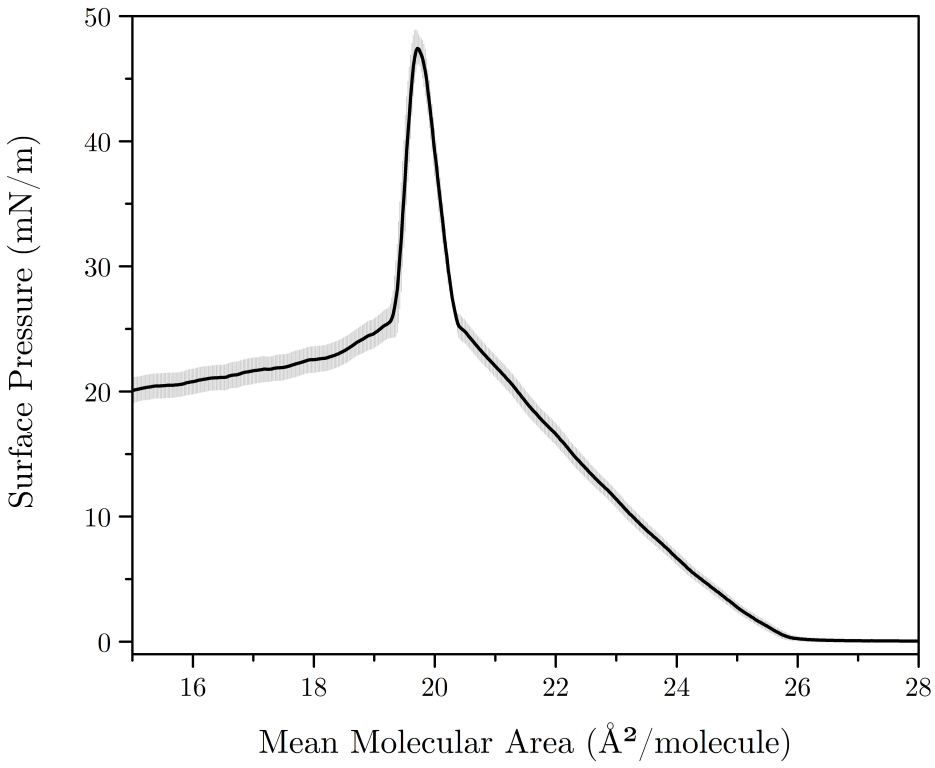

Figure 4.5: Π-A isotherm of palmitic acid on ultrapure water at pH 5.6.

have been shown to form contact ion pairs with palmitate at the air-water interface; hence, Na^+ ions compete with solvating water molecules around the headgroup which decrease the headgroup hydration and lead to increased palmitate stability at the interface.[70] Consequently, palmitate desorption into the subphase is slowed.

The palmitic acid isotherms in Figures 4.5 - 4.7 demonstrate how the phase behavior changes as a function of pH and NaCl presence in the subphase. On water at pH 5.6 (Figure 4.5), the monolayer undergoes a phase transition from the gaseous (G) to LC phase at 26 Å^2/molecule. The LC-S phase transition occurs at 20.5 Å^2/molecule (25 mN/m), and the monolayer collapses at 20 Å^2/molecule (47 mN/m). The nearly vertical rise in surface pressure in the S phase and the sharp collapse indicate a highly compact and rigid monolayer. This observation is supported by tilt angle measurements in which the aliphatic chain angle from surface normal was 5.3° at 30 mN/m.[86]

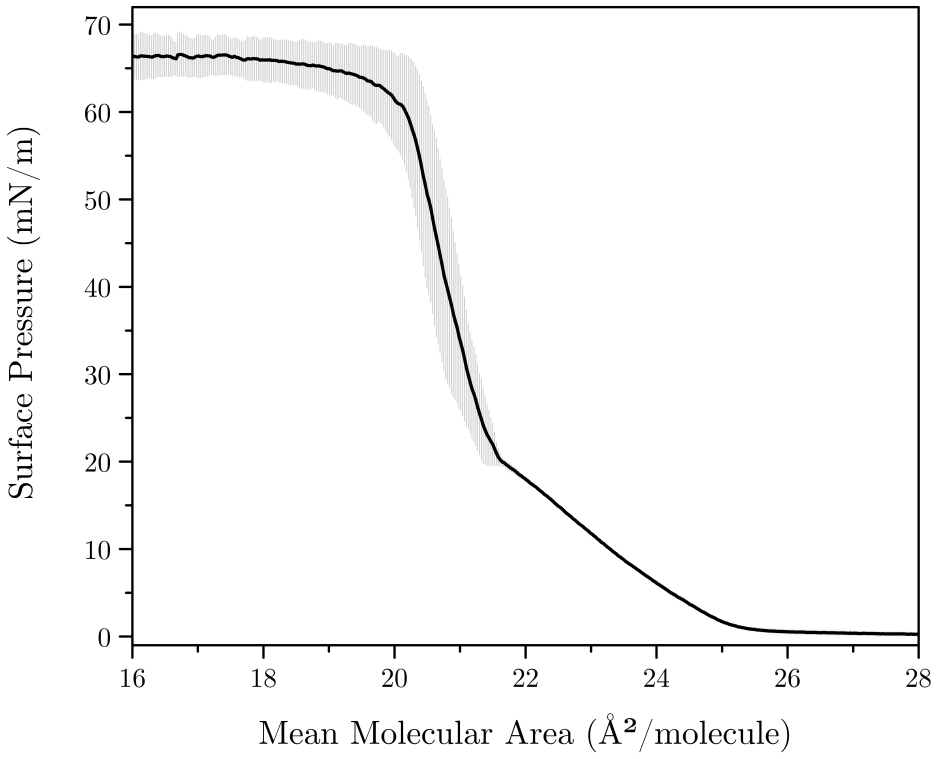

Figure 4.6: Π-A isotherm of palmitic acid on aqueous 0.4 M NaCl at pH 8.2.

At the LC-S phase transition, the measured tilt angle was 28.6°, further supporting the hypothesis of a phase transition from an ordered, tilted phase to a compact, nearly untilted phase.[70]

Addition of NaCl alters the mean molecular area (MMA) and surface pressure at which phase transitions occur in palmitic acid monolayers. The lift-off point is the same at pH 5.6 regardless of the presence of NaCl. At pH 8.2 (Figure 4.6), the lift-off point is shifted to a smaller MMA (25.5 Å^2/molecule) likely caused by palmitate desorption in the gaseous phase. The LC-S phase transition occurs at 21.5 Å^2/molecule and 22.0 Å^2/molecule at 20 mN/m for 0.4 M NaCl subphases at pH 8.2 and 5.6, respectively. The ions simultaneously increase the MMA and decrease the surface pressure at the phase transition. Thus, the NaCl renders the monolayer more compressible and less rigid. Na^+ ions likely intercalate between the palmitic

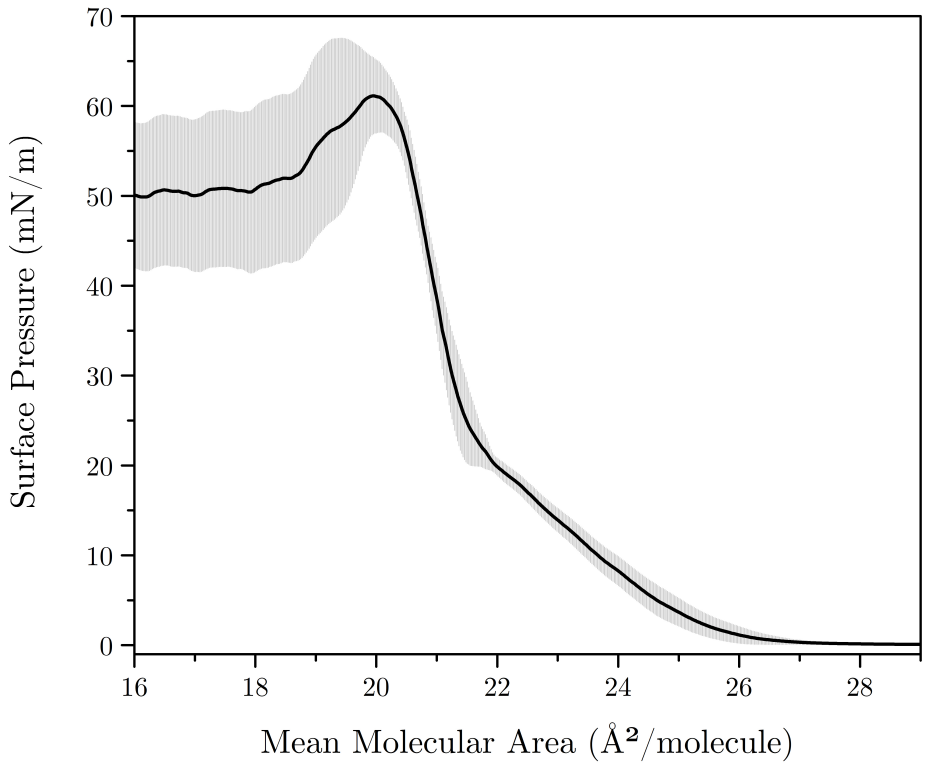

Figure 4.7: Π-A isotherm of palmitic acid on aqueous 0.4 M NaCl at pH 5.6.

acid molecules and screen electrostatic repulsion between the carboxyl groups which decreases the transition surface pressure.[44]

The largest difference between the three palmitic acid isotherms lies in their collapse structures. Palmitic acid on water at pH 5.6 (Figure 4.5) forms a rigid monolayer, as suggested by the sharp increase and subsequent decrease in surface pressure around the surface pressure maximum. This collapse behavior is indicative of a fracturing mechanism. The presence of 0.4 M NaCl at the same pH (Figure 4.7) decreases the rigidity of the monolayer and broadens the collapse shape. Further compression beyond the surface pressure maximum causes a decrease in surface pressure, but it only decreases to 50 mN/m which is near the collapse pressure of palmitic acid on water at pH 5.6. Increasing the pH of the NaCl solution (Figure 4.6) eliminates the drop in surface pressure altogether such that additional compression produces a sur-

face pressure plateau at 66 mN/m. This surface pressure plateau is likely caused by a folding collapse mechanism.[59] Thus, the constant collapse pressure suggests that a palmitic acid monolayer on model seawater achieves the "Goldilocks" rigidity regime in which it is neither too rigid nor too fluid to fold.

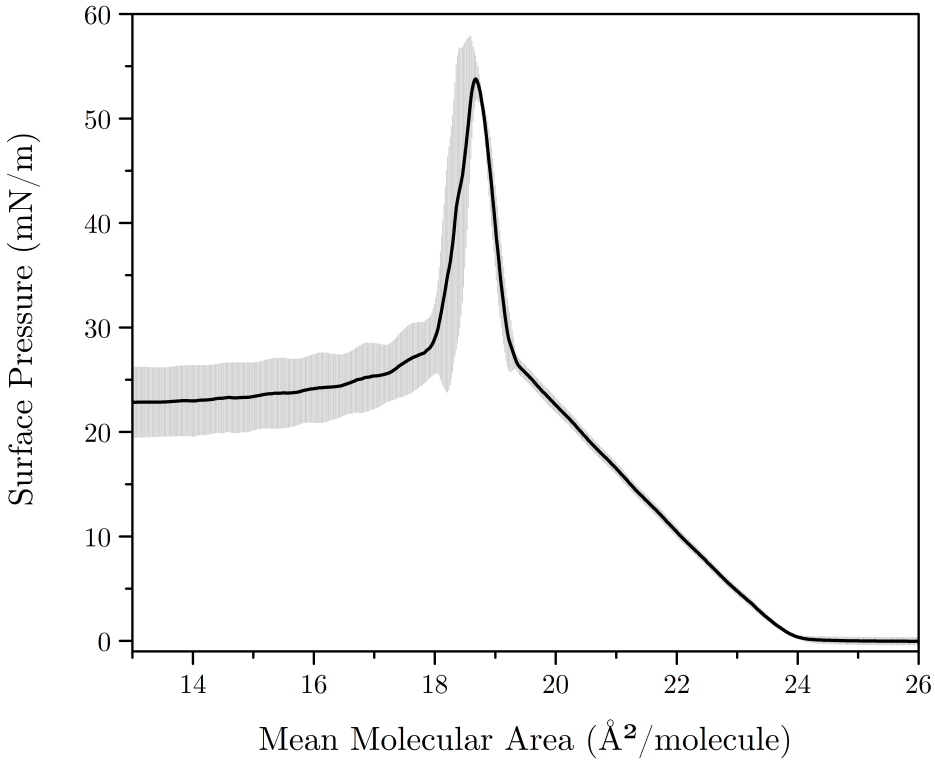

Figure 4.8: Π-A isotherm of stearic acid on ultrapure water at pH 5.6.

Stearic acid exhibits similar phase behavior to that of palmitic acid (Figures 4.8 - 4.10). Because stearic acid has two more carbons in its aliphatic chain than palmitic acid, it forms a more rigid monolayer due to the stronger dispersion interactions. As a result, the lift-off point on water at pH 5.6 (Figure 4.8) occurs at 24 Å^2/molecule. The G-LC phase transition on 0.4 M NaCl at pH 8.2 (Figure 4.9) occurs at a slightly smaller MMA due to stearate desorption into the bulk aqueous phase. Stearic acid undergoes the LC-S phase transition at 19.5 Å^2/molecule and 27 mN/m on water and at 19.5 Å^2/molecule and 23 mN/m on 0.4 M NaCl at pH 5.6. At pH 8.2, the LC-S

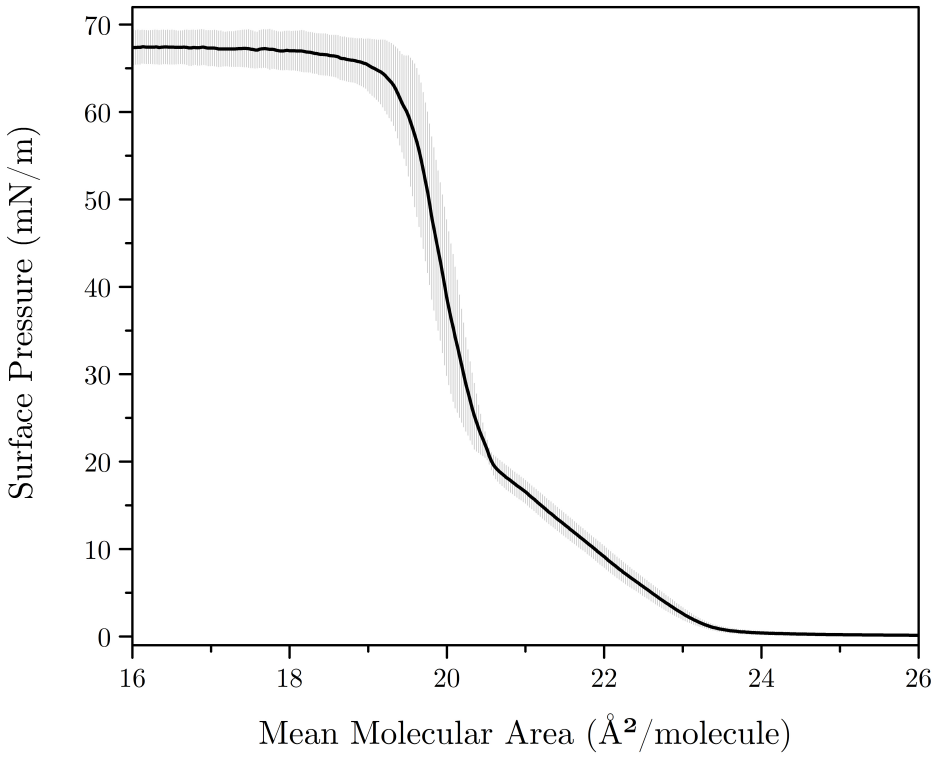

Figure 4.9: Π-A isotherm of stearic acid on aqueous 0.4 M NaCl at pH 8.2.

transition occurs at 20.5 Å^2/molecule and 20 mN/m. Like palmitic acid, the NaCl ions fluidize the stearic acid monolayer. Additionally, the collapse mechanisms are the same as those for palmitic acid on all three subphase compositions. Stearic acid fractures on water due to its highly rigid interfacial packing and exhibits a broadened, high pressure collapse at the same pH on 0.4 M NaCl. Lastly, the model seawater subphase likely causes the stearic acid monolayer to fold.[59]

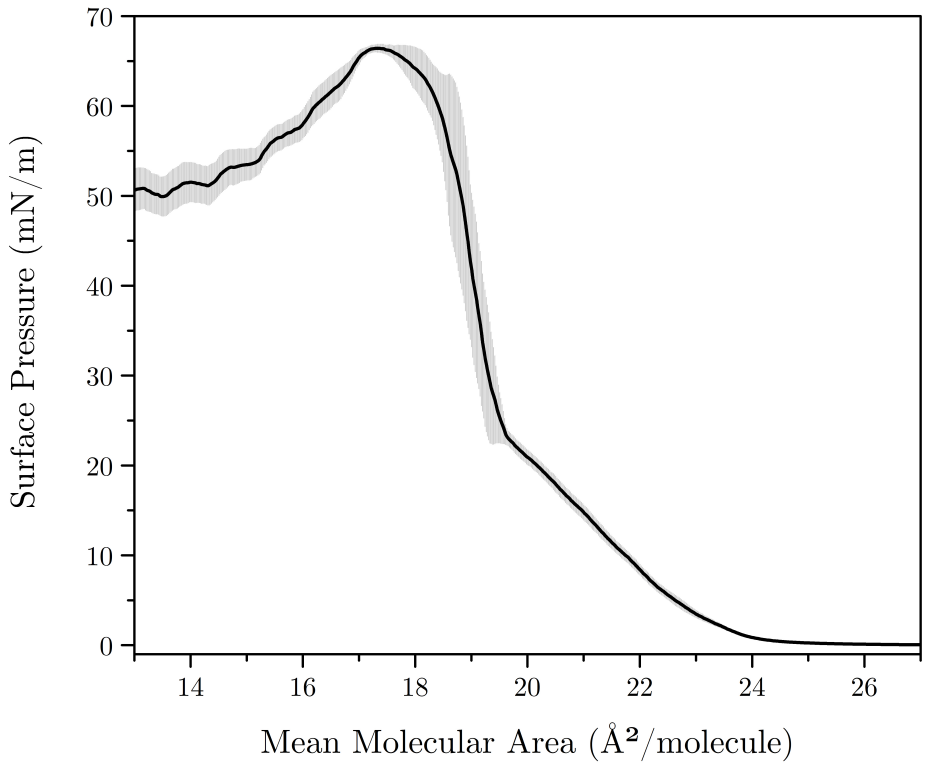

Figure 4.10: Π-A isotherm of stearic acid on aqueous 0.4 M NaCl at pH 5.6.

4.1.2 SSA Proxy Surface Pressure-Area Isotherms

The goal of this study was to understand how the composition of the aqueous subphase impacts the interfacial organization of a sea spray aerosol (SSA) proxy mixture of fatty acids at the air-water interface. In order to answer this question, surface pressure-area isotherms were conducted to measure the interfacial phase behavior of the film. Normally for mixed monolayers, one of the first questions to evaluate relates to the miscibility of the system. However, due to the solubility of lauric acid, Equation 2.52 cannot be used to investigate the ideality of amphiphile mixing. Lauric acid desorption also causes the isotherms to be shifted to lower MMA values, so the mean molecular area is denoted as "Apparent MMA" to indicate that the values are based on the SSA proxy mixture concentration initially spread onto the interface. Because each isotherm in Figure 4.11 has only one collapse, then it is very likely that the SSA

proxy mixture is miscible.

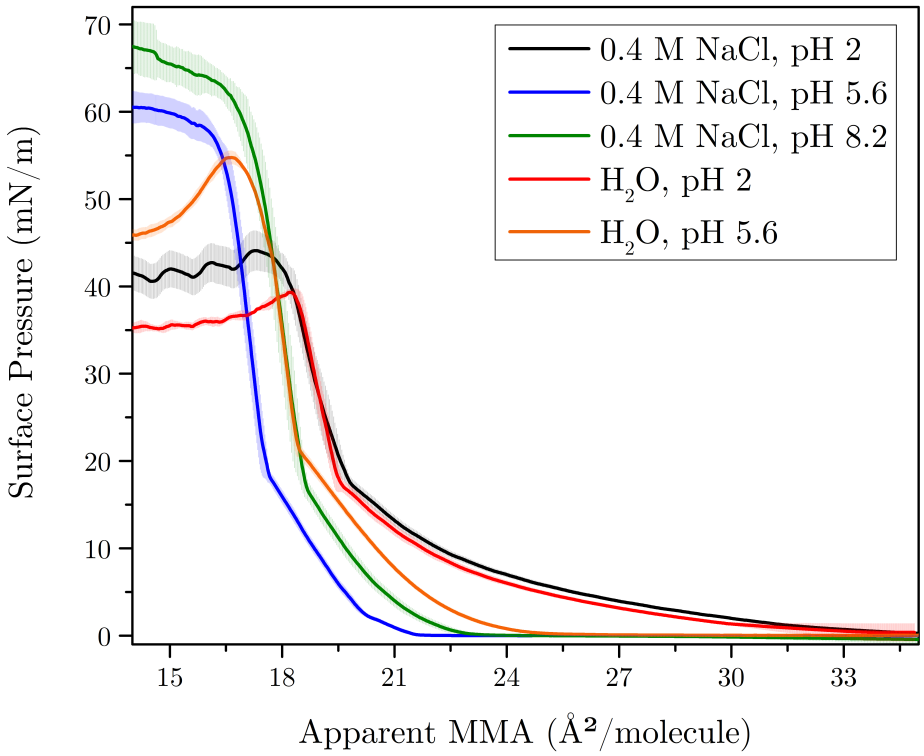

Figure 4.11: Π-A isotherms of the SSA proxy mixture on ultrapure water and aqueous 0.4 M NaCl at various pH values.

Palmitic acid and stearic acid are expected to dominate the phase behavior characteristics of the monolayer due to their large molar ratios within the mixture and their slow desorption kinetics. This is reflected in isotherms measured on subphases at pH 5.6 and 8.2 due to their steep increases in surface pressure and low MMA values at lift-off. At pH 2.0, the LE phase of the isotherms are broadened, indicating the increased contribution of myristic acid to the monolayer due to decreased desorption into the subphase. The isotherms conducted on water and 0.4 M NaCl at pH 2.0 are virtually the same; both lift-off at 34 Å^2/molecule and undergo a LE-LC phase transition at 20 Å^2/molecule. However, the collapse structures of the two subphases differ. The isotherm on water exhibits a sharp collapse at 18 Å^2/molecule and 39 mN/m. The NaCl solution enhances the condensed monolayer stability by

increasing the collapse pressure to 45 mN/m and decreasing the collapse MMA to 17 Å^2/molecule.

Although MMA values of phase transitions in the SSA proxy monolayer at pH 5.6 and 8.2 cannot be definitively assigned due to lauric acid and myristic acid desorption, the MMA values at a phase transition can be compared between the monolayer mixture isotherms on the various aqueous subphases. Unlike the individual surface pressure-area isotherms, the MMA differences between the monolayer phase transitions on water and 0.4 M NaCl are significantly different. Interestingly, isotherms on water at pH 5.6 and on 0.4 NaCl at pH 8.2 have a high degree of overlap in the solid phase. The mixture on water has a lift-off MMA 2 Å^2/molecule greater than on the seawater model subphase. Both undergo the LC-S phase transition at nearly the same MMA, but the mixture on water has a surface pressure 4 mN/m higher than the aqueous NaCl subphase. This indicates that the SSA proxy monolayer on water is more compressible and more stable in the LC phase. Additionally, the collapse structures differ between the two subphases; the mixture on 0.4 M NaCl at pH 8.2 approaches a surface pressure plateau, similar to that of stearic acid and palmitic acid on the same subphase (Figures 4.6 and 4.9). It appears as though the mixture still preserves the ideal rigidity necessary for a folding collapse mechanism.

Perhaps the most curious result is the SSA proxy mixture isotherm on 0.4 M NaCl at pH 5.6. It is significantly contracted compared to the isotherm on water at the same pH. The lift-off point on aqueous NaCl is 3.5 Å^2/molecule lower in MMA, and the LC-S phase transition is shifted by 1.5 Å^2/molecule. Secondly, there is a brief LE phase. Lastly, the mixture reaches a constant pressure collapse around 60 mN/m, unlike palmitic acid and stearic acid which fully collapse on the same subphase (Figures 4.7 and 4.10). It is possible that the sodium cations are facilitating deprotonation of the lipids which increases their solubility. The single component isotherms may not deprotonate as readily due to their tighter packing and higher dispersion interactions.

However, the addition of myristic acid and lauric acid disorders the packing, increasing the amount of space between the lipids and allowing for greater Na^+ : headgroup interactions. The amount of deprotonation is not enough to cause significant electrostatic repulsion, which could explain why the isotherm on pH 8.2 is more expanded. Additionally, the increased amount of carboxylate : Na^+ interactions may provide just the right amount of monolayer fluidity to yield a folding collapse mechanism.

4.1.3 Control SSA Proxy Surface Pressure-Area Isotherms

Because lauric acid is too soluble to obtain a surface pressure-area isotherm, it is difficult to determine its impact on the phase behavior of the SSA proxy mixtures. While lauric acid demonstrates some surface activity (Figure A.1), it is still possible for the longer chain fatty acids to push lauric acid out of the monolayer throughout compression due to the competition for space at the air-water interface. Thus, a control SSA proxy mixture was created, consisting of 2 myristic acid : 4 palmitic acid : 3 stearic acid. Then, surface pressure-area isotherms were conducted on the same set of subphases as before, except for water at pH 2.0 (Figure 4.12). This subphase was excluded due to the similar SSA proxy mixture phase behavior on 0.4 M NaCl at the same pH.

The SSA proxy mixtures spread on 0.4 M NaCl at pH 8.2 and on water at pH 5.6 nearly overlap, like the phase behavior observed in Figure 4.11. A constant pressure collapse is also obtained at approximately the same surface pressure as the four-part mixture at pH 8.2, suggesting that lauric acid does not dramatically change interfacial behavior in nascent SSA conditions. This is as expected since the basic pH would favor lauric acid deprotonation and subsequent desorption into the subphase. While a fatty acid monolayer is expected to be more compressed at basic pH because of enhanced desorption, it is possible that electrostatic repulsion between the carboxylate headgroups counteract some of the monolayer contraction.

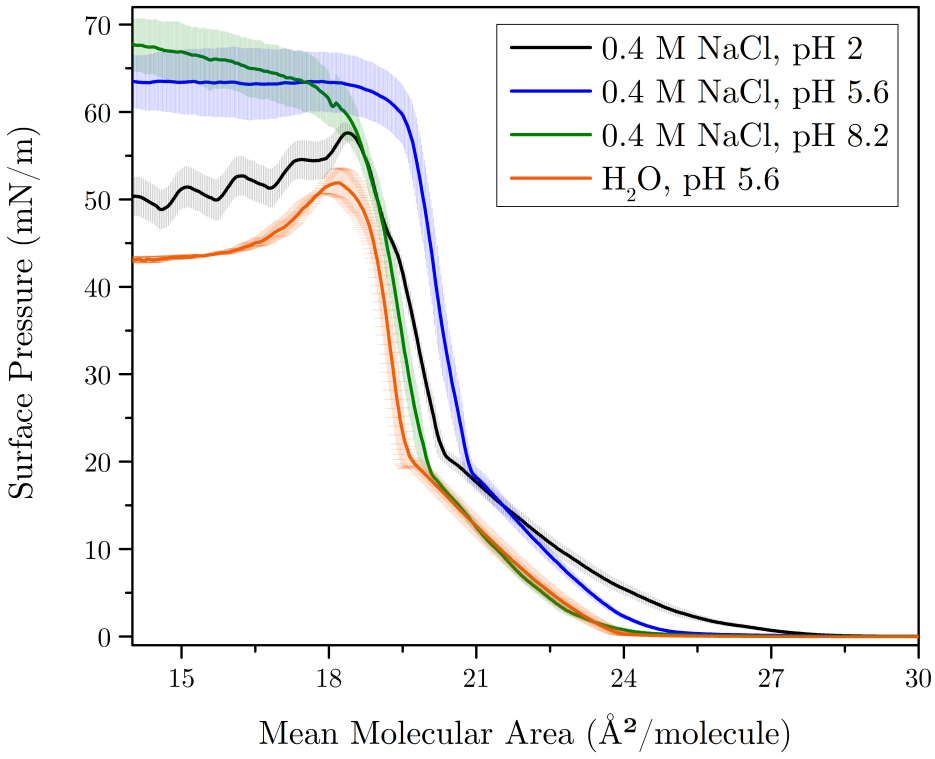

Figure 4.12: Π-*A* isotherms of the control SSA proxy mixtures on ultrapure water and aqueous 0.4 M NaCl at various pH values.

Similar to the SSA proxy mixture, the control mixture on an aqueous sodium chloride subphase at pH 2.0 is expanded in the LC phase relative to the isotherms on all of the other subphases; this is likely because of decreased myristic acid desorption. Specifically, the control mixture lifts off at 27.5 Å^2/molecule. Surprisingly, the isotherm at pH 2.0 is more compressed in the solid phase than the isotherm on aqueous sodium chloride at pH 5.6, which is the exact opposite trend of the one observed in the four-part SSA proxy mixture (Figure 4.11). The control mixture LC-S phase transition on 0.4 M NaCl at pH 5.6 occurs at an MMA 1 Å^2/molecule more than the mixture on aqueous NaCl at pH 2.0 and 1.5 Å^2/molecule greater than the mixture on water at pH 5.6. Like before, the mixture on the 0.4 M NaCl subphase at pH 5.6 exhibits a constant collapse pressure around 60 mN/m, in this case the average plateau pressure occurring at 63 mN/m. While the monolayer maintains its interme-

diate rigidity regardless of the presense of lauric acid, its phase dyanamics are altered by the absence of lauric acid. It is possible that the other fatty acids are able to pack more tightly and interact more strongly via increased dispersion interactions, hence decreasing the amount of lipid desorption into the subphase. The control mixture at pH 2.0 is less compressible than the corresponding SSA proxy mixture, meaning that lauric acid increases monolayer fluidity at low pH. This suggests that interfacial organization and behavior is significantly changed as the SSA pH decreases in the marine boundary layer.

4.2 Isotherm Surface Pressure Analysis

In order to better elucidate trends in the surface pressure-area isotherms, apparent MMA at constant pressure was plotted as a function of subphase pH. The surface pressures 10 mN/m and 30 mN/m were chosen as representative pressures in the liquid and solid phases, respectively. Isotherms of the individual fatty acids were compared to qualitatively evaluate their packing and stability on each subphase. The mixture isotherms were evaluated in the same manner. Similar plots at constant MMA values in the liquid and solid phases, rather than at constant surface pressures, were generated as well. The plots yielded equivalent trends, as shown in Figures D.1 and D.2.

4.2.1 Individual Fatty Acids Analysis

In the liquid phase (Figure 4.13), myristic acid (C_{14}) has the largest MMA which is indicative of an expanded monolayer. The shorter alkyl chains yield weaker dispersion interactions, so the amphiphiles pack less tightly. However, as the pH increases from 2.0 to 5.6, the myristic acid MMA precipitously drops due to increased desorption into the subphase. The MMA of myristic acid on water at pH 5.6 is smaller than

that of myristic acid on 0.4 M NaCl at pH 5.6, suggesting that NaCl stabilizes the monolayer. Palmitic acid (C_{16}) and stearic acid (C_{18}) have lower MMA values at pH 5.6 than myristic acid, but their MMA values remain stable with increasing pH. Hence, desorption into the subphase is minimal. Stearic acid has the smallest MMA because of its strong dispersion interactions and tight packing, and palmitic acid has a slightly larger MMA. Palmitic acid is expected to have weaker dispersion interactions than stearic acid because the stearic acid alkyl chain is longer by two carbon atoms. Although isotherms of palmitic acid and stearic acid were not measured at pH 2.0, their MMA values are expected to be the same as those at pH 5.6 and 8.2.

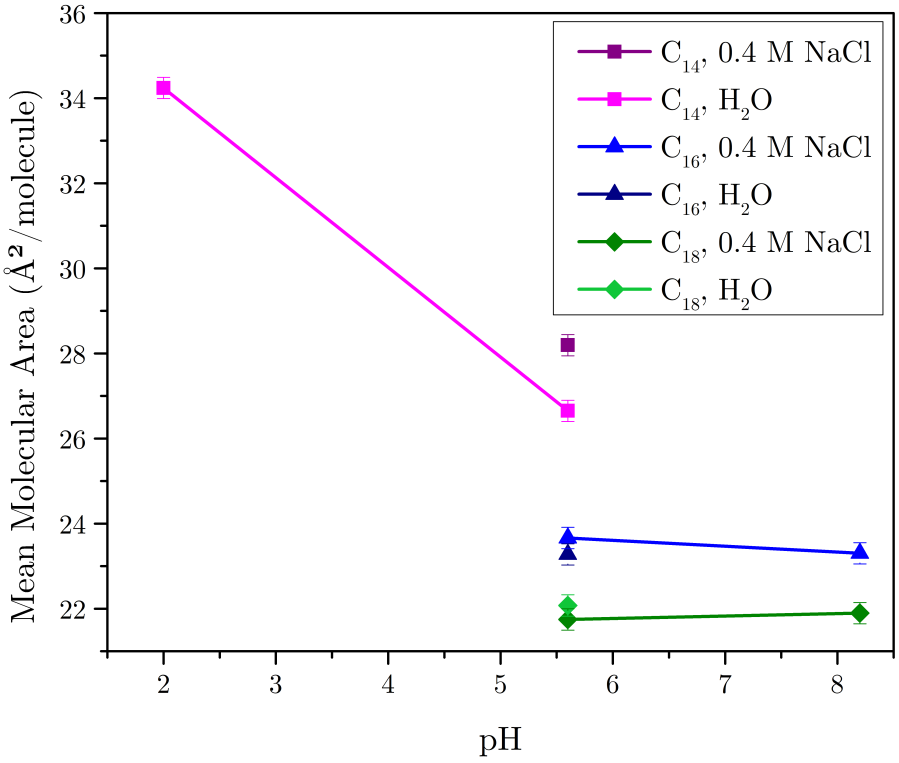

Figure 4.13: Constant pressure analysis of the individual fatty acid isotherms. The mean molecular area at a surface pressure of 10 mN/m is plotted as a function of subphase pH.

The solid phase (Figure 4.14) exhibits different interfacial behavior, but many of the trends remain the same as in the liquid phase. Myristic acid has the smallest

MMA at pH 2.0 and 5.6 because of desorption into the subphase. Stearic acid has a smaller MMA than palmitic acid at pH 5.6 and 8.2 because of its increased dispersion interactions and tighter packing. The MMA of stearic acid increases from pH 5.6 to 8.2, likely due to greater electrostatic repulsion between the negatively charged carboxylate headgroups. Palmitic acid has the largest MMA, and it forms a stable monolayer because its MMA does not change significantly from pH 5.6 to 8.2. At pH 5.6, palmitic acid on water has a lower MMA than palmitic acid on 0.4 M NaCl; Na^+ could expand the monolayer by intercalating between the carboxyl headgroups, and it could enhance palmitic acid stability at the air-water interface. Like in the liquid phase, the MMA values of palmitic acid and stearic acid are expected to remain approximately unchanged from pH 2.0 to 5.6.

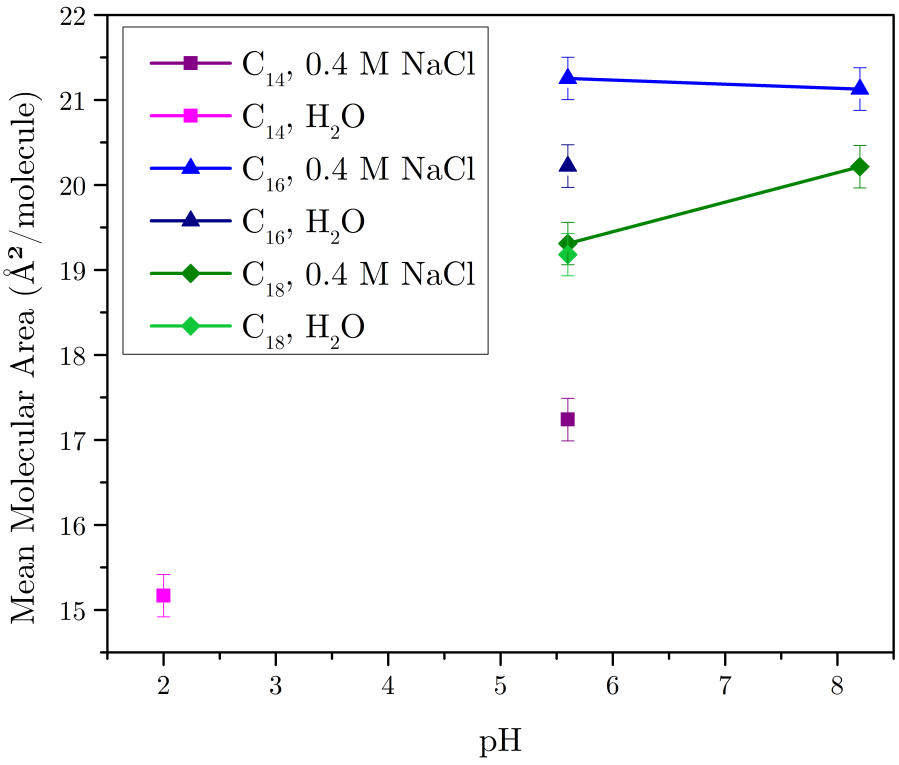

Figure 4.14: Constant pressure analysis of the individual fatty acid isotherms. The mean molecular area at a surface pressure of 30 mN/m is plotted as a function of subphase pH.

Finally, the monolayer collapse pressures are an indication of the individual fatty acid film stability (Figure 4.15). Myristic acid collapses at the lowest surface pressure, indicating that it forms the least stable film. Palmitic acid has a significantly higher collapse pressure, suggesting that the monolayer is able to decrease surface tension by a greater degree because of its tighter packing and higher stability at the air-water interface. Stearic acid has the highest collapse pressure, meaning that it forms a highly compact and stable monolayer. NaCl increases the collapse pressure for all three fatty acids. The Na^+ cation likely screens the carboxyl headgroups and enhances film stability at small MMA.

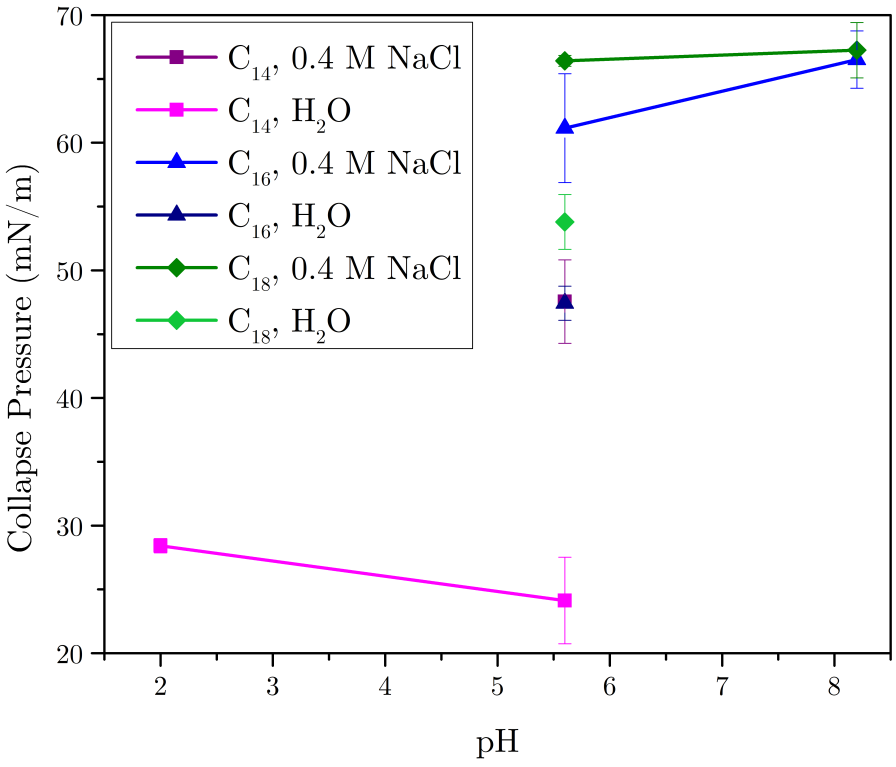

Figure 4.15: Collapse pressures of the individual fatty acid isotherms as a function of subphase pH.

4.2.2 Fatty Acids Mixture Analysis

Lauric acid desorption is significant at both low and high pH, so the MMA values are denoted as "apparent" to signify that they do not represent absolute mean molecular area. Rather, the apparent MMA will be shifted to smaller values with increasing lauric acid desorption. This can be seen in Figure 4.16 in which the SSA proxy MMA values in the liquid phase at 10 mN/m decrease from pH 2.0 to pH 5.6; higher pH facilitates lauric acid deprotonation which consequently increases lauric acid solubility and desorption into the subphase. The MMA values of the three-component control mixture on 0.4 M NaCl also decrease from pH 2.0 to pH 8.2, but to a lesser extent. This is most likely caused by myristic acid desorption at higher pH values.

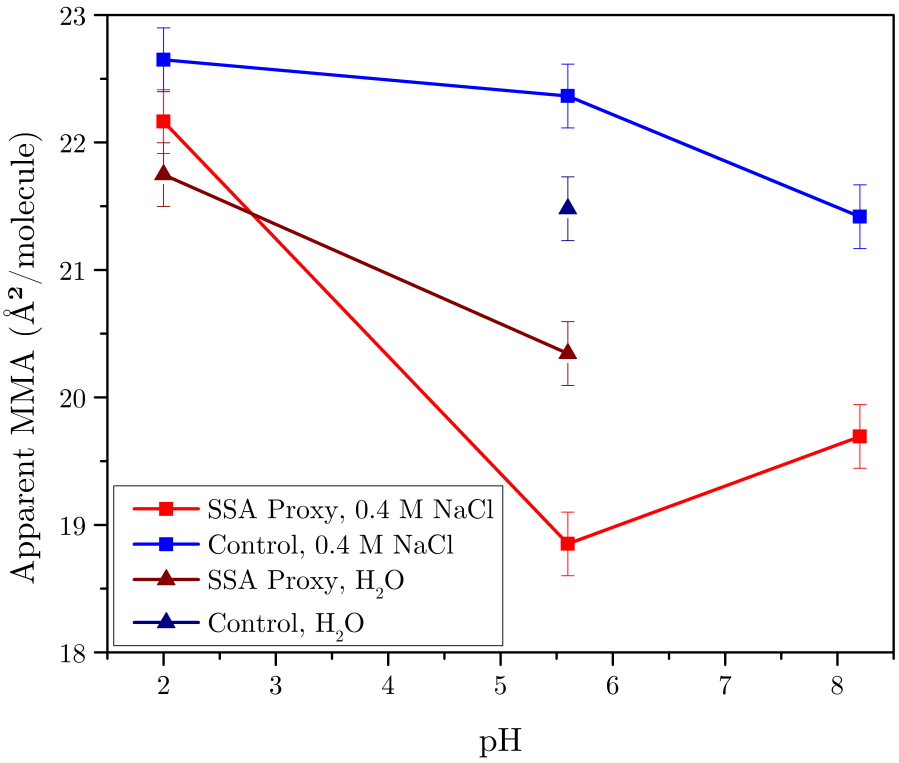

Figure 4.16: Constant pressure analysis of the fatty acid mixture isotherms. The mean molecular area at a surface pressure of 10 mN/m is plotted as a function of subphase pH.

While the mixtures largely behave similarly to their individual fatty acid compo-

nents, the phase behavior of the SSA proxy mixture deviates substantially at pH 5.6 (Figure 4.16). The apparent MMA of the SSA proxy monolayer on 0.4 M NaCl drops below that of the film on water. Normally, NaCl enhances fatty acid stability at the air-water interface. The control mixture behaves as expected at pH 5.6 in which the film on 0.4 M NaCl has a higher MMA than the film on water. Upon addition of lauric acid in the SSA proxy mixture, the apparent MMA of the monolayer on 0.4 M NaCl drops significantly below that of the film on water. Thus, it is possible that the increase in monolayer fluidity due to lauric acid decreases the dispersion interactions between the aliphatic molecules, and the Na^+ cation facilitates fatty acid deprotonation such that myristic acid and lauric acid desorption is increased. An increase in the SSA proxy MMA on 0.4 M NaCl from pH 5.6 to 8.2 is most likely the result of electrostatic repulsion between the carboxylate headgroups which expands the film.

The phase behavior in the solid phase at 30 mN/m is similar to that of the liquid phase, but the differences in apparent MMA at each pH are smaller in magnitude (Figure 4.17). The control films have larger MMA values than the SSA proxy films because of lauric acid desorption. At pH 2.0, the SSA proxy monolayers on water and 0.4 M NaCl have the same MMA; this is expected since the lipids are fully protonated, so Na^+ interacts with the carboxyl headgroups minimally. As in Figure 4.16, the apparent MMA of the SSA proxy monolayer on 0.4 M NaCl is smaller than the film MMA on water. However, the difference between the two MMA values is smaller in the solid phase than in the liquid phase, suggesting that the impact of lauric acid on the SSA proxy film reorganization is decreased upon compression. The MMA of the control monolayer on 0.4 M NaCl increases slightly from pH 2.0 to pH 5.6 which could be caused by electrostatic repulsion, but the difference is so small that the error bars partially overlap. SSA proxy mixture apparent MMA on 0.4 M NaCl rises from pH 5.6 to pH 8.2, likely because of electrostatic repulsion between the carboxylate headgroups.

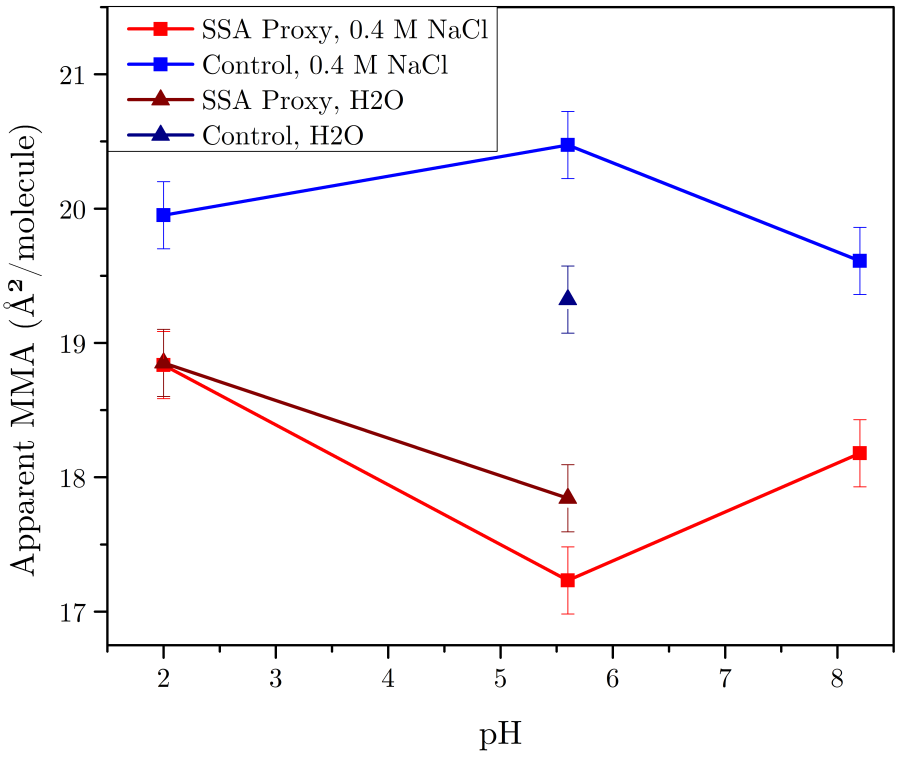

Figure 4.17: Constant pressure analysis of the fatty acid mixture isotherms. The mean molecular area at a surface pressure of 30 mN/m is plotted as a function of subphase pH.

At collapse, the fatty acid mixtures follow a clearer set of trends. Collapse pressure increases with increasing pH, and high collapse pressures are indicative of rigid, tightly-packed monolayers.[59] Electrostatic interactions between the negatively-charged carboxylate headgroups and Na^+ cations are expected to yield rigid ordering within the monolayer, and the magnitude of these interactions increases at higher pH due to greater lipid deprotonation. This is observed in the higher collapse pressures on 0.4 M NaCl than on water. Additionally, the collapse pressures of the control monolayers are greater than the collapse pressures of the SSA proxy films on their corresponding subphases. Lauric acid increases monolayer fluidity due to weaker dispersion interactions between the aliphatic chains, so the SSA proxy monolayers have lower collapse pressures. The disordering effect from lauric acid decreases at higher

pH due to desorption into the subphase.

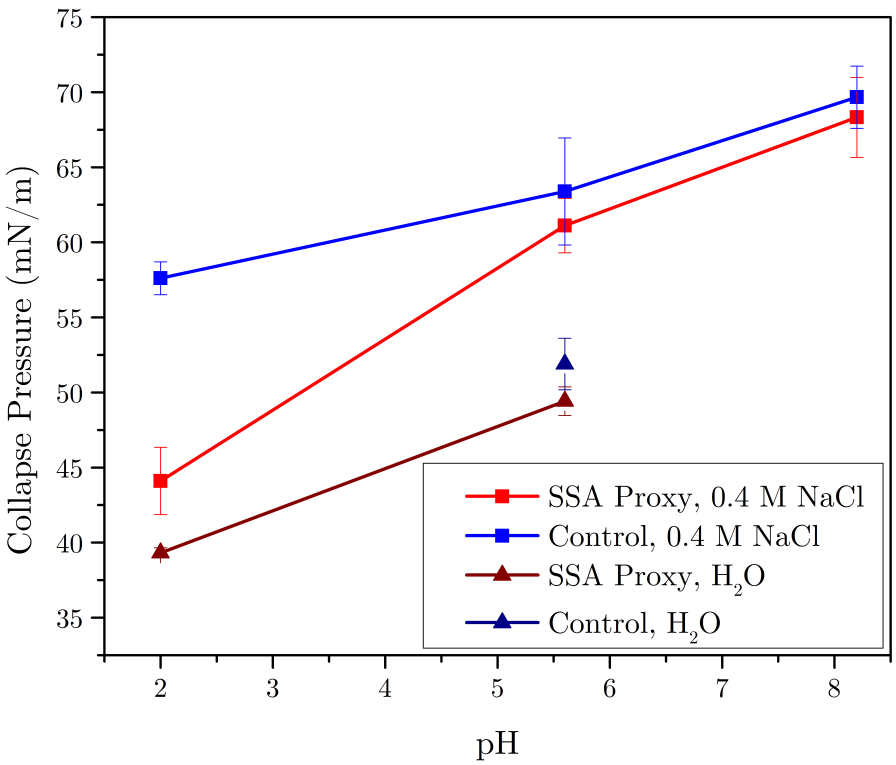

Figure 4.18: Collapse pressures of the fatty acid mixture isotherms as a function of subphase pH.

4.3 Lauric Acid Retention in the Mixed Monolayer

Complex desorption equilibria of lauric acid makes evaluation of the lauric acid contribution to the overall mean molecular area of the mixture isotherms particularly challenging. Shifts in the MMA are not specific to lauric acid alone; all four fatty acids are susceptible to some desorption over time, and the MMA is highly dependent upon molecular organization and packing at the air-water interface. While the dissolution of stearic acid and palmitic acid is quite minimal at the pH values studied, the desorption of myristic acid is significant at pH 5.6 and 8.2. Thus, in order to isolate the effects from lauric acid, the four-part SSA proxy mixture isotherms are

compared to the three-part control SSA proxy mixture isotherms. However, the calculated concentration of the four-part mixture is altered to remove the mole fraction contribution of lauric acid artificially:

$$[\text{Mixture}]_{\text{c}} = \frac{2n_{\text{myristic}} + 4n_{\text{palmitic}} + 3n_{\text{stearic}}}{V_{\text{lauric}} + V_{\text{myristic}} + V_{\text{palmitic}} + V_{\text{stearic}}} \tag{4.2}$$

$[\text{Mixture}]_{\text{c}}$ is the corrected mixture concentration, n is the number of moles of each fatty acid, and V is the volume of each fatty acid aliquot added to the mixture. Surface pressure-area isotherms are inherently a surface-specific technique, so removing the mole fraction contribution of lauric acid from the mixture concentration will shift the MMA such that the isotherm will perfectly align with the three-part control mixture isotherm if lauric acid is entirely absent from the interface.

Once the apparent MMA values of the corrected SSA proxy monolayer are known, they can be used to quantify lauric acid retention in the film. The equation

$$\frac{\text{MMA}_{\text{corrected}} - \text{MMA}_{\text{control}}}{\text{MMA}_{\text{corrected}} - \text{MMA}_{\text{uncorrected}}} \times 100\% = \%\ \text{C}_{12}\ \text{Retained} \tag{4.3}$$

describes the percentage of lauric acid retained in the SSA proxy monolayer. All retention percentage values were calculated in the solid phase at a surface pressure of 30 mN/m to minimize monolayer organization effects on the phase behavior, which are significant in the liquid phase. The numerator corresponds to the MMA contribution from lauric acid retention, and the denominator corresponds to the MMA contribution from the total amount of lauric acid originally spread onto the surface. When 0% of lauric acid is retained, the corrected SSA proxy MMA will be equal to the control MMA at some constant surface pressure (Figure 4.19). Conversely, if 100% of lauric acid is retained, the uncorrected SSA proxy MMA will overlap with the control MMA. Retention percentages between the two extremes will cause the uncorrected and corrected MMA values to translate by the same magnitude. However, their posi-

tioning around the control MMA indicates how much lauric acid is retained. Greater desorption is indicated by a larger difference in MMA between the control and the uncorrected SSA proxy than the control and the corrected SSA proxy.

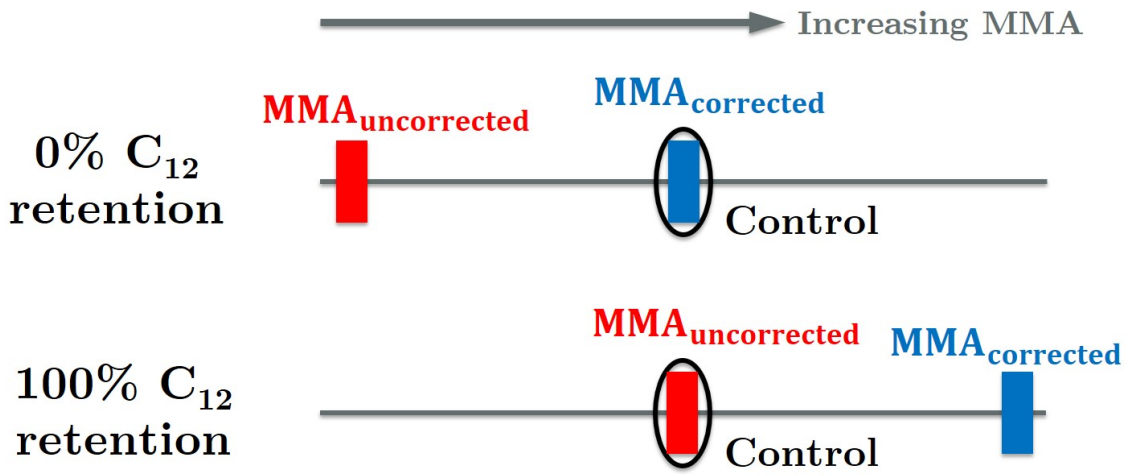

Figure 4.19: Schematic illustrating how the uncorrected and corrected MMA values of the SSA proxy mixtures will be shifted relative to that of the control mixture at 0% and 100% lauric acid retention. The red block represents the uncorrected SSA proxy MMA, the blue block represents the corrected SSA proxy MMA, and the black oval represents the control MMA.

Despite the fast desorption kinetics into the bulk aqueous phase at pH 8.2, lauric acid is still surface active (Figure 4.20). All three phase transitions (G-LC, LC-S, and collapse) are shifted to MMA values 1 $Å^2$/molecule higher in the corrected SSA proxy mixture isotherm. The shapes of the two isotherms are largely the same, suggesting that the molecular organization is similar between the two mixtures. Additionally, the slopes of the isotherms are very close to one another, meaning that the monolayer compressibility is approximately equal. Lauric acid retention at pH 8.2 is 30%, implying that soluble surfactants do play an important role in the interfacial behavior of nascent SSA.

The impact of lauric acid on the SSA proxy isotherms on aqueous subphases at pH 5.6 is more complicated (Figure 4.21). On water, the corrected SSA proxy mixture isotherm is expanded relative to the control mixture isotherm. More specifically, the

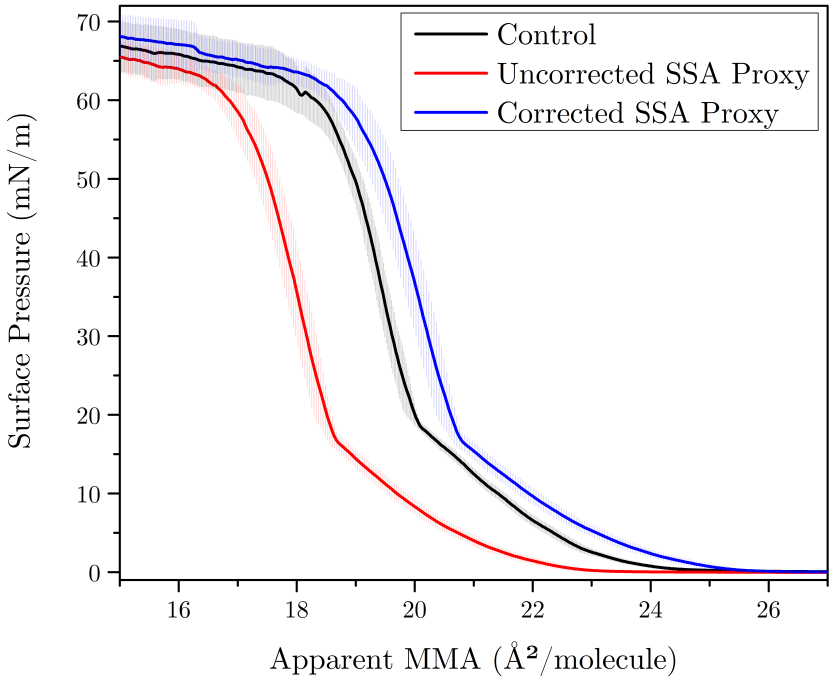

Figure 4.20: Π-A isotherms of the control and SSA proxy mixtures on aqueous 0.4 M NaCl at pH 8.2. Lauric acid retention is 30%.

lift-off point is increased by 5 Å^2/molecule, the LC - S phase transition is increased by 0.5 Å^2/molecule, and the collapse occurs at nearly the same MMA and surface pressure. The SSA proxy monolayer is more compressible than the control mixture, as evidenced by the expanded LC phase and smaller rate of surface pressure increase in the liquid phases. Thus, lauric acid increases the fluidity of the monolayer on water which is most likely caused by more disordered packing from weaker dispersion interactions between the alkyl chains. This is supported by the gradual decrease in monolayer expansion as surface pressure increases; compressing the fatty acids together increases the dispersion interactions, so the SSA proxy mixture packing begins to approach that of the control mixture interfacial organization. A lauric acid retention value of 26% is slightly less than that of the SSA proxy monolayer on 0.4 M NaCl at pH 8.2, suggesting that NaCl plays a significant role in stabilizing lauric acid in the SSA proxy film.

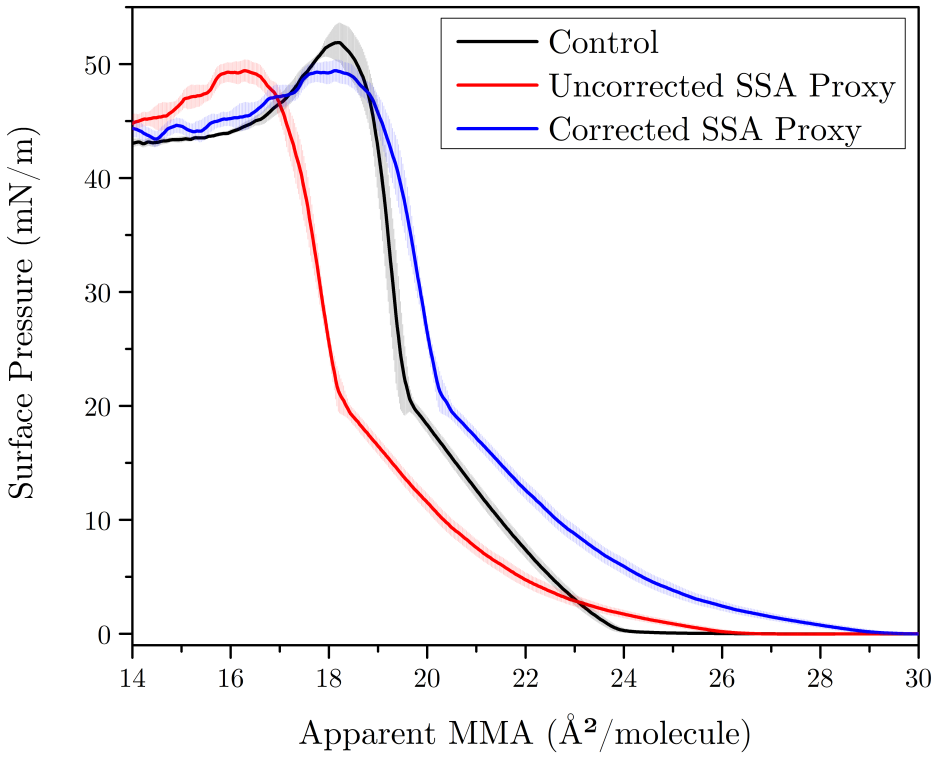

Figure 4.21: Π-*A* isotherms of the control and SSA proxy mixtures on ultrapure water at pH 5.6. Lauric acid retention is 26%.

SSA proxy isotherms on 0.4 M NaCl at pH 5.6 exhibit particularly strange interfacial behavior in comparison to the control SSA proxy isotherm (Figure 4.22). The corrected SSA proxy isotherm is compressed by 1 Å^2/molecule at lift-off, 1.5 Å^2/molecule at the LC-S phase transition, and 1.5 Å^2/molecule at collapse. Secondly, the SSA proxy monolayer briefly exists in a LE state. Therefore, lauric acid dramatically changes lipid organization at the air-water interface. The SSA proxy monolayer is more compressible than the three-component control as shown by the distinct LE phase and the slightly lower rate of surface pressure rise with decreasing MMA in the LC phase. Then the isotherm slopes become equivalent in the solid phase. It would appear as though lauric acid facilitates desorption of other lipids in the monolayer at this pH. Consequently, lauric acid retention could not be calculated from the corrected and uncorrected MMA values. Further studies need to be con-

ducted to confidently characterize the mechanism behind this anomalous interfacial behavior.

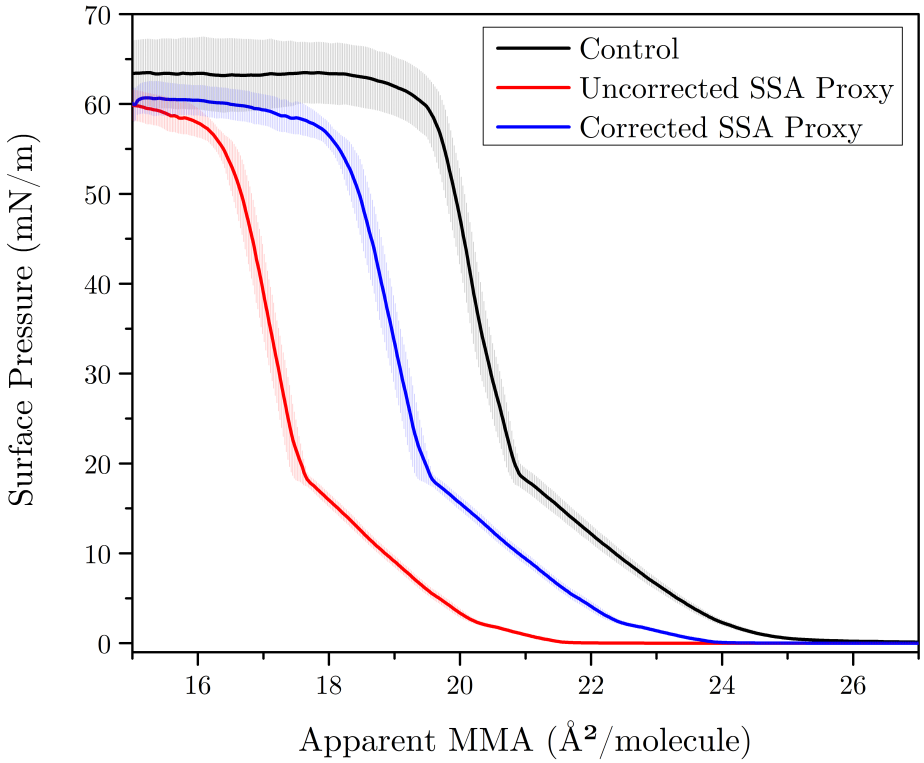

Figure 4.22: Π-A isotherms of the control and SSA proxy mixtures on 0.4 M NaCl at pH 5.6. Lauric acid retention is unknown.

Lastly, SSA proxy monolayers behave as expected at pH 2.0 (Figure 4.23). The corrected four-component mixture isotherms on water and 0.4 M NaCl are both expanded by 11 Å^2/molecule compared to the control mixture isotherm. Their monolayers are significantly more compressible too, as demonstrated by the gradual increase in surface pressure with decreasing MMA. The LC-S phase transition is only expanded by 1.5 Å^2/molecule, suggesting that the films become more similarly ordered at lower MMA. Monolayer collapse differs appreciably between the control and the corrected SSA proxy isotherms. The three-component control isotherm collapses at 58 mN/m, and the four-component isotherms on water and aqueous NaCl collapse at 40 mN/m and 45 mN/m, respectively. A higher collapse pressure is indicative of

greater film rigidity in the condensed phase, so the lauric acid is likely disordering the monolayer. NaCl minimally stabilizes the condensed phase for both mixtures, as shown by the small decrease in collapse MMA. Thus, the interfacial behavior of SSA proxy films is drastically different at low pH, and the surface activity of soluble organics is much higher due to decreased desorption. More specifically, 50% of the lauric acid is retained within the SSA proxy monolayer. As a result, organic matter interfacial organization on nascent SSA is expected to be quite dissimilar from that of SSA in the marine boundary layer.

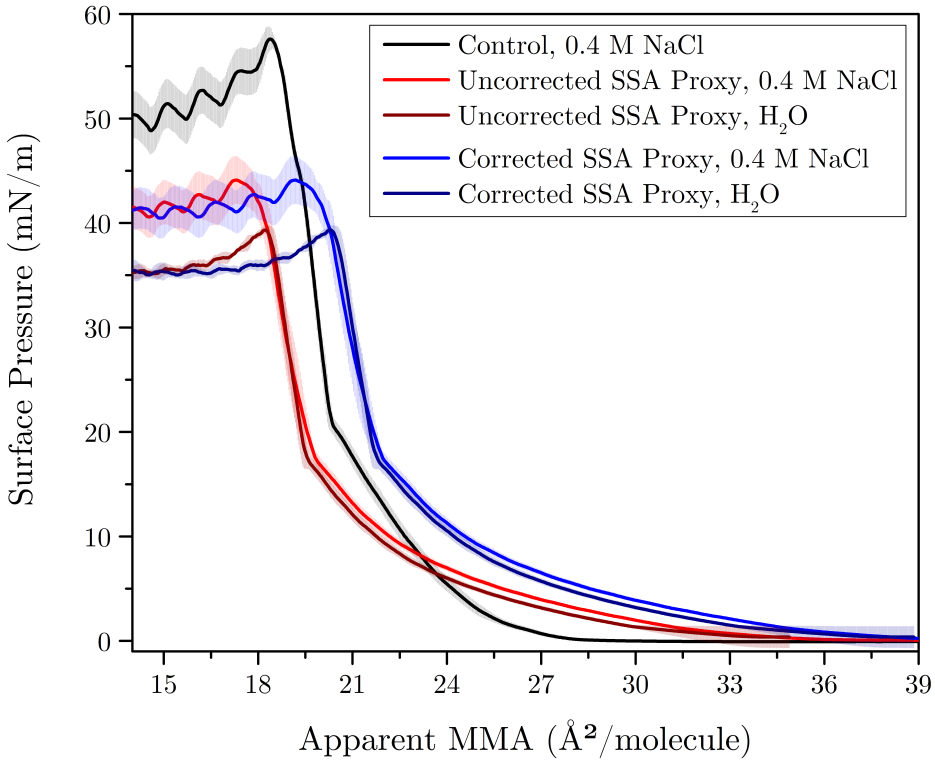

Figure 4.23: Π-A isotherms of the control and SSA proxy mixtures on ultrapure water and aqueous 0.4 M NaCl at pH 2.0. Lauric acid retention is 50%.

4.4 Lipid Parameterization in Climate Models

Due to the large scale of climate modeling, organic constituents in marine aerosol are classified into polysaccharides, proteins, lipids, humics, and processed compounds. These classes of compounds are represented by one particular model molecule that roughly encompasses the surface behavior and reactivity measured in real SSA. Stearic acid serves as the model lipid compound due to its high abundance in SSA and high surface activity.[28] Experimental data is used to empirically parameterize the model, such as half-saturation concentrations $C_{1/2}$, Langmuir coefficients α_i, molecular weight, and MMA.[35,87] The MMA chosen for stearic acid in the OCEANFILMS model is 18 Å^2/molecule,[88,89] which is at or beyond its collapse on all subphases tested in this study (Figures 4.8 - 4.10). Additionally, stearic acid forms a more compact monolayer than the SSA proxy films examined above. Thus, overestimation of the alkane : hydroxyl ratio in OCEANFILMS-2[38] could be partially explained by the poor choice in MMA for the lipids component and by the exclusion of soluble surfactants from the model.

Fatty acid organization at the air-water interface is highly dependent upon pH. Nascent SSA has a pH near that of bulk seawater,[42] so soluble surfactants will have a smaller impact on surface molecular organization than insoluble, long-chain fatty acids. Consequently, the SSA organic film will probably be more compressed. As the SSA travels through the marine boundary layer, its pH will decrease from interactions with gaseous acidic species.[42,90] Amphiphile organization at the air-water interface is dramatically different from pH 5.6 to pH 2.0, and these differences are largely driven by soluble amphiphiles such as myristic acid and lauric acid. Decreasing pH increases the surface activity and film fluidity of the fatty acid mixtures, so the surface tension of aged SSA near monolayer collapse is likely to be higher than that of nascent SSA. Competitive adsorption and cooperative adsorption mechanisms will also likely become more significant at low pH due to the increased organic surface activity. As

such, improved lipid parameterization within climate models should include changes in surface activity and MMA as a function of aerosol pH to account for the impact of labile surfactants.

Chapter 5

Conclusions and Future Work

The aim of this study was to determine how the presence of soluble organics within a sea spray aerosol (SSA) proxy fatty acid mixture altered interfacial film behavior as a function of aqueous subphase composition. The subphase consisted of water and 0.4 M NaCl solutions at various pH values to model the aqueous components of nascent SSA and aged SSA in the marine boundary layer. Surface pressure-area isotherms were used to measure the monolayer phase behavior. Soluble fatty acids impacted mixture phase behavior at all subphase conditions, and their surface activities increased with decreasing pH. Secondly, long-chain fatty acids increased interfacial retention of the short-chain fatty acids, likely through enhanced dispersion interactions between the alkyl chains. This work highlights the importance of incorporating soluble fatty acids in lipid climate model parameters due to their variable and significant influence on molecular organization at the air-water interface.

Fatty acids used in this project include lauric acid (C_{12}), myristic acid (C_{14}), palmitic acid (C_{16}), and stearic acid (C_{18}). Lauric acid was too soluble to obtain a complete isotherm, and myristic acid was also too soluble at pH 8.2 to obtain an isotherm. Palmitic acid and stearic acid were both sufficiently insoluble, and they formed rigid monolayers due to their strong dispersion interactions. When mixed

together in a molar ratio of 1 lauric acid : 2 myristic acid : 4 palmitic acid : 3 stearic acid, the two-dimensional phase behavior dramatically changed depending upon presence of NaCl and pH. NaCl increased film collapse pressure, and it exhibited modest effects on mixture mean molecular area (MMA) due to interactions with the carboxyl headgroups. A subphase at pH 8.2 (the pH of seawater) increased desorption kinetics for the soluble fatty acids, so the mixture isotherm had more palmitic and stearic acid character. Decreasing pH increased the surface activity of myristic acid and lauric acid, so the monolayer became more compressible as a result of more disordered film packing. This effect was especially evident at pH 2.0 in which the SSA proxy monolayer was highly expanded and compressible in the liquid phase.

The contribution of lauric acid to film behavior was evaluated by subtracting the lauric acid molar fraction from the SSA proxy mixture concentration, and the isotherms were compared to control mixtures containing only 2 myristic acid : 4 palmitic acid : 3 stearic acid. These results showed that lauric acid was surface active on all subphase compositions. At pH 8.2, the corrected SSA proxy monolayer was expanded relative to the control mixture, and the shape of the isotherms were similar; lauric acid exhibited 30% retention in the monolayer but had a smaller impact on interfacial molecular organization due to subphase desorption. The corrected SSA proxy mixture isotherm was also expanded on water at pH 5.6, but the 0.4 M NaCl isotherm was contracted relative to the control mixture. Lauric acid appeared to simultaneously increase mixture compressibility and enhance lipid desorption into the subphase. Lauric acid retention could not be determined on 0.4 M NaCl, but it had a retention value of 26% on water. Lastly, the corrected SSA proxy monolayer at pH 2.0 was significantly expanded and more compressible relative to the control mixture isotherm, and 50% of lauric acid was retained in the film. This demonstrated that lauric acid had a large impact on molecular packing at the air-water interface despite constituting a small mole fraction of the mixture. Consequently, these results

reveal the importance of parameterizing soluble organic lipids as major contributors to SSA interfacial organization throughout the marine boundary layer.

In future work, other techniques need to be applied to better characterize the SSA proxy film phase behavior. Brewster angle microscopy (BAM) will be used to take images of the mixtures in each phase state to visualize macroscopic film organization at the air-water interface. Additionally, BAM images can reveal the type of collapse mechanism observed in the isotherm experiments. Infrared reflection-absorption spectroscopy (IRRAS) will be used to probe the protonation state of the carboxyl headgroups as a function of subphase composition. While this method will not be specific to any of the fatty acids in the mixture, the spectra could provide a qualitative understanding of monolayer deprotonation that could then explain some of the phase behavior measured in the surface pressure-area isotherms. Constant surface pressure relaxation experiments of the SSA proxy mixture will be used to quantify surface excess parameters that can be directly applied in climate models. Lastly, the divalent cations Ca^{2+} and Mg^{2+} will be added to the aqueous subphase due to their enrichment in SSA and their strong interactions with lipid headgroups.[29,71,91] These cations have been observed to compress monolayers at the air-water interface, so it will be important to characterize how the cations affect labile surfactant activity on SSA proxy surfaces.

Bibliography

[1] IPCC, 2013, In *Climate Change 2014: Synthesis Report*; Core Writing Team,, Pachauri, R. K., Meyer, L., Eds.; Intergovernmental Panel on Climate Change: Geneva, Switzerland, 2015; OCLC: 914851124.

[2] IPCC, 2014, In *Climate Change 2013: The Physical Science Basis: Working Group I Contribution to the Fifth Assessment Report of the Intergovernmental Panel on Climate Change*; Stocker, T. F., Qin, D., Plattner, G.-K., Tignor, M. M. B., Allen, S. K., Boschung, J., Nauels, A., Xia, Y., Bex, V., Midgley, P. M., Eds.; Cambridge University Press: New York, 2014.

[3] Haywood, J.; Boucher, O. Estimates of the Direct and Indirect Radiative Forcing Due to Tropospheric Aerosols: A Review. *Reviews of Geophysics* **2000**, *38*, 513–543.

[4] Carslaw, K. S.; Lee, L. A.; Reddington, C. L.; Pringle, K. J.; Rap, A.; Forster, P. M.; Mann, G. W.; Spracklen, D. V.; Woodhouse, M. T.; Regayre, L. A.; Pierce, J. R. Large Contribution of Natural Aerosols to Uncertainty in Indirect Forcing. *Nature* **2013**, *503*, 67–71.

[5] Satheesh, S.; Krishnamoorthy, K. Radiative Effects of Natural Aerosols: A Review. *Atmospheric Environment* **2005**, *39*, 2089–2110.

[6] IPCC, 2007, In *Climate Change 2007: Synthesis Report*; Core Writing Team,, Pachauri, R. K., Reisinger, A., Eds.; IPCC: Geneva, Switzerland, 2007.

[7] de Leeuw, G.; Andreas, E. L.; Anguelova, M. D.; Fairall, C. W.; Lewis, E. R.; O'Dowd, C.; Schulz, M.; Schwartz, S. E. Production Flux of Sea Spray Aerosol. *Reviews of Geophysics* **2011**, *49*, RG2001.

[8] Thorpe, S. A. Bubble Clouds and the Dynamics of the Upper Ocean. *Quarterly Journal of the Royal Meteorological Society* **1992**, *118*, 1–22.

[9] Hoffman, E. J.; Duce, R. A. Factors Influencing the Organic Carbon Content of Marine Aerosols: A Laboratory Study. *Journal of Geophysical Research* **1976**, *81*, 3667–3670.

[10] Bird, J. C.; de Ruiter, R.; Courbin, L.; Stone, H. A. Daughter Bubble Cascades Produced by Folding of Ruptured Thin Films. *Nature* **2010**, *465*, 759–762.

[11] Bertram, T. H.; Cochran, R. E.; Grassian, V. H.; Stone, E. A. Sea Spray Aerosol Chemical Composition: Elemental and Molecular Mimics for Laboratory Studies of Heterogeneous and Multiphase Reactions. *Chemical Society Reviews* **2018**, *47*, 2374–2400.

[12] O'Dowd, C. D.; Facchini, M. C.; Cavalli, F.; Ceburnis, D.; Mircea, M.; Decesari, S.; Fuzzi, S.; Yoon, Y. J.; Putaud, J.-P. Biogenically Driven Organic Contribution to Marine Aerosol. *Nature* **2004**, *431*, nature02959.

[13] O'Dowd, C. D.; de Leeuw, G. Marine Aerosol Production: A Review of the Current Knowledge. *Philosophical Transactions of the Royal Society of London A: Mathematical, Physical and Engineering Sciences* **2007**, *365*, 1753–1774.

[14] Prather, K. A. et al. Bringing the Ocean into the Laboratory to Probe the Chemical Complexity of Sea Spray Aerosol. *Proceedings of the National Academy of Sciences* **2013**, *110*, 7550–7555.

[15] Quinn, P. K.; Collins, D. B.; Grassian, V. H.; Prather, K. A.; Bates, T. S. Chemistry and Related Properties of Freshly Emitted Sea Spray Aerosol. *Chemical Reviews* **2015**, *115*, 4383–4399.

[16] Twomey, S. Pollution and the Planetary Albedo. *Atmospheric Environment (1967)* **1974**, *8*, 1251–1256.

[17] Brooks, S. D.; Thornton, D. C. Marine Aerosols and Clouds. **2018**,

[18] Sorjamaa, R.; Svenningsson, B.; Raatikainen, T.; Henning, S.; Bilde, M.; Laaksonen, A. The Role of Surfactants in Köhler Theory Reconsidered. *Atmospheric Chemistry and Physics* **2004**, *4*, 2107–2117.

[19] Yoon, Y. J.; Ceburnis, D.; Cavalli, F.; Jourdan, O.; Putaud, J. P.; Facchini, M. C.; Decesari, S.; Fuzzi, S.; Sellegri, K.; Jennings, S. G.; O'Dowd, C. D. Seasonal Characteristics of the Physicochemical Properties of North Atlantic Marine Atmospheric Aerosols. *Journal of Geophysical Research: Atmospheres* **2007**, *112*, D04206.

[20] Claeys, M.; Wang, W.; Vermeylen, R.; Kourtchev, I.; Chi, X.; Farhat, Y.; Surratt, J. D.; Gómez-González, Y.; Sciare, J.; Maenhaut, W. Chemical Characterisation of Marine Aerosol at Amsterdam Island during the Austral Summer of 2006–2007. *Journal of Aerosol Science* **2010**, *41*, 13–22.

[21] Russell, L. M.; Hawkins, L. N.; Frossard, A. A.; Quinn, P. K.; Bates, T. S. Carbohydrate-like Composition of Submicron Atmospheric Particles and Their Production from Ocean Bubble Bursting. *Proceedings of the National Academy of Sciences* **2010**, *107*, 6652–6657.

[22] Gantt, B.; Meskhidze, N. The Physical and Chemical Characteristics of Marine Primary Organic Aerosol: A Review. *Atmospheric Chemistry and Physics* **2013**, *13*, 3979–3996.

[23] van Pinxteren, M.; Fiedler, B.; van Pinxteren, D.; Iinuma, Y.; Körtzinger, A.; Herrmann, H. Chemical Characterization of Sub-Micrometer Aerosol Particles in the Tropical Atlantic Ocean: Marine and Biomass Burning Influences. *Journal of Atmospheric Chemistry* **2015**, *72*, 105–125.

[24] Van Pinxteren, M.; Barthel, S.; Fomba, K. W.; Müller, K.; Von Tümpling, W.; Herrmann, H. The Influence of Environmental Drivers on the Enrichment of Organic Carbon in the Sea Surface Microlayer and in Submicron Aerosol Particles – Measurements from the Atlantic Ocean. *Elem Sci Anth* **2017**, *5*, 35.

[25] Collins, D. B.; Zhao, D. F.; Ruppel, M. J.; Laskina, O.; Grandquist, J. R.; Modini, R. L.; Stokes, M. D.; Russell, L. M.; Bertram, T. H.; Grassian, V. H.; Deane, G. B.; Prather, K. A. Direct Aerosol Chemical Composition Measurements to Evaluate the Physicochemical Differences between Controlled Sea Spray Aerosol Generation Schemes. *Atmos. Meas. Tech.* **2014**, *7*, 3667–3683.

[26] Lee, C.; Sultana, C. M.; Collins, D. B.; Santander, M. V.; Axson, J. L.; Malfatti, F.; Cornwell, G. C.; Grandquist, J. R.; Deane, G. B.; Stokes, M. D.; Azam, F.; Grassian, V. H.; Prather, K. A. Advancing Model Systems for Fundamental Laboratory Studies of Sea Spray Aerosol Using the Microbial Loop. *The Journal of Physical Chemistry A* **2015**, *119*, 8860–8870.

[27] Wang, X. et al. Microbial Control of Sea Spray Aerosol Composition: A Tale of Two Blooms. *ACS Central Science* **2015**, *1*, 124–131.

[28] Cochran, R. E.; Laskina, O.; Jayarathne, T.; Laskin, A.; Laskin, J.; Lin, P.; Sultana, C.; Lee, C.; Moore, K. A.; Cappa, C. D.; Bertram, T. H.; Prather, K. A.; Grassian, V. H.; Stone, E. A. Analysis of Organic Anionic Surfactants in Fine and Coarse Fractions of Freshly Emitted Sea Spray Aerosol. *Environmental Science & Technology* **2016**, *50*, 2477–2486.

[29] Jayarathne, T.; Sultana, C. M.; Lee, C.; Malfatti, F.; Cox, J. L.; Pendergraft, M. A.; Moore, K. A.; Azam, F.; Tivanski, A. V.; Cappa, C. D.; Bertram, T. H.; Grassian, V. H.; Prather, K. A.; Stone, E. A. Enrichment of Saccharides and Divalent Cations in Sea Spray Aerosol During Two Phytoplankton Blooms. *Environmental Science & Technology* **2016**, *50*, 11511–11520.

[30] Cochran, R. E. et al. Molecular Diversity of Sea Spray Aerosol Particles: Impact of Ocean Biology on Particle Composition and Hygroscopicity. *Chem* **2017**, *2*, 655–667.

[31] Pham, D. Q.; O'Brien, R.; Fraund, M.; Bonanno, D.; Laskina, O.; Beall, C.; Moore, K. A.; Forestieri, S.; Wang, X.; Lee, C.; Sultana, C.; Grassian, V.; Cappa, C. D.; Prather, K. A.; Moffet, R. C. Biological Impacts on Carbon Speciation and Morphology of Sea Spray Aerosol. *ACS Earth and Space Chemistry* **2017**, *1*, 551–561.

[32] Sciare, J.; Favez, O.; Sarda-Estève, R.; Oikonomou, K.; Cachier, H.; Kazan, V. Long-Term Observations of Carbonaceous Aerosols in the Austral Ocean Atmosphere: Evidence of a Biogenic Marine Organic Source. *Journal of Geophysical Research* **2009**, *114*.

[33] Gantt, B.; Meskhidze, N.; Facchini, M. C.; Rinaldi, M.; Ceburnis, D.; O'Dowd, C. D. Wind Speed Dependent Size-Resolved Parameterization for the Organic Mass Fraction of Sea Spray Aerosol. *Atmospheric Chemistry and Physics* **2011**, *11*, 8777–8790.

[34] Rinaldi, M.; Fuzzi, S.; Decesari, S.; Marullo, S.; Santoleri, R.; Provenzale, A.; von Hardenberg, J.; Ceburnis, D.; Vaishya, A.; O'Dowd, C. D.; Facchini, M. C. Is Chlorophyll-a the Best Surrogate for Organic Matter Enrichment in Submicron Primary Marine Aerosol? *Journal of Geophysical Research: Atmospheres* **2013**, *118*, 4964–4973.

[35] Burrows, S. M.; Ogunro, O.; Frossard, A. A.; Russell, L. M.; Rasch, P. J.; Elliott, S. M. A Physically Based Framework for Modeling the Organic Fractionation of Sea Spray Aerosol from Bubble Film Langmuir Equilibria. *Atmos. Chem. Phys.* **2014**, *14*, 13601–13629.

[36] Elliott, S.; Burrows, S. M.; Deal, C.; Liu, X.; Long, M.; Ogunro, O.; Russell, L. M.; Wingenter, O. Prospects for Simulating Macromolecular Surfactant Chemistry at the Ocean–Atmosphere Boundary. *Environmental Research Letters* **2014**, *9*, 064012.

[37] Ogunro, O. O.; Burrows, S. M.; Elliott, S.; Frossard, A. A.; Hoffman, F.; Letscher, R. T.; Moore, J. K.; Russell, L. M.; Wang, S.; Wingenter, O. W. Global Distribution and Surface Activity of Macromolecules in Offline Simulations of Marine Organic Chemistry. *Biogeochemistry* **2015**, *126*, 25–56.

[38] Burrows, S. M.; Gobrogge, E.; Fu, L.; Link, K.; Elliott, S. M.; Wang, H.; Walker, R. OCEANFILMS-2: Representing Coadsorption of Saccharides in Marine Films and Potential Impacts on Modeled Marine Aerosol Chemistry: SACCHARIDE COADSORPTION IN MARINE FILMS. *Geophysical Research Letters* **2016**, *43*, 8306–8313.

[39] Hawkins, L. N.; Russell, L. M. Polysaccharides, Proteins, and Phytoplankton Fragments: Four Chemically Distinct Types of Marine Primary Organic Aerosol Classified by Single Particle Spectromicroscopy. https://www.hindawi.com/journals/amete/2010/612132/, 2010.

[40] Frossard Amanda A.,; Russell Lynn M.,; Burrows Susannah M.,; Elliott Scott M.,; Bates Timothy S.,; Quinn Patricia K., Sources and Composition of Submicron Organic Mass in Marine Aerosol Particles. *Journal of Geophysical Research: Atmospheres* **2014**, *119*, 12,977–13,003.

[41] Millero, F. J. *Chemical Oceanography*, 4th ed.; Taylor & Francis: Boca Raton, 2013.

[42] Fridlind, A. M.; Jacobson, M. Z. A Study of Gas-Aerosol Equilibrium and Aerosol pH in the Remote Marine Boundary Layer during the First Aerosol Characterization Experiment (ACE 1). *Journal of Geophysical Research: Atmospheres* **2000**, *105*, 17325–17340.

[43] Panayiotou, C. Interfacial Tension and Interfacial Profiles of Fluids and Their Mixtures. *Langmuir* **2002**, *18*, 8841–8853.

[44] Butt, H.-J.; Graf, K.; Kappl, M. *Physics and Chemistry of Interfaces*, third, revised and enlarged edition ed.; Wiley-VCH Verlag GmbH & Co. KGaA: Weinheim, Germany, 2013; OCLC: ocn823552831.

[45] Gaines, G. L. *Insoluble Monolayers at Liquid-Gas Interfaces*; Interscience Publishers, 1966.

[46] Chattoraj, D. K.; Birdi, K. S. *Adsorption and the Gibbs Surface Excess*; Plenum Press: New York, 1984.

[47] Guggenheim, E. A. *Thermodynamics: An Advanced Treatment for Chemists and Physicists*; North-Holland Pub. Co., 1959.

[48] Zuidema, H.; Waters, G. Ring Method for the Determination of Interfacial Tension. *Industrial & Engineering Chemistry Analytical Edition* **1941**, *13*, 312–313.

[49] Huh, C.; Mason, S. G. A Rigorous Theory of Ring Tensiometry. *Colloid and Polymer Science* **1975**, *253*, 566–580.

[50] Padday, J. F.; Pitt, A. R.; Pashley, R. M. Menisci at a Free Liquid Surface: Surface Tension from the Maximum Pull on a Rod. *Journal of the Chemical Society, Faraday Transactions 1: Physical Chemistry in Condensed Phases* **1975**, *71*, 1919–1931.

[51] Dynarowicz-Łątka, P.; Kita, K. Molecular Interaction in Mixed Monolayers at the Air/Water Interface. *Advances in Colloid and Interface Science* **1999**, *79*, 1–17.

[52] Hosoi, K.; Ishikawa, T.; Tomioka, A.; Miyano, K. Quantitative Image Analysis in Brewster Angle Microscopy: Molecular Tilt of a Stearic Acid Monolayer on Water. *Japanese Journal of Applied Physics* **1993**, *32*, L135–L137.

[53] Lautz, C.; Fischer, T. M. Determination of the Tilt Angle of Langmuir Monolayers with Brewster Angle Autocorrelation Spectroscopy and Quantitative Image Analysis in Brewster Angle Microscopy: A Comparison between Two Different Methods. *Japanese Journal of Applied Physics* **1997**, *36*, 5703–5706.

[54] Lautz, C.; Fischer, T. M. Brewster Angle Autocorrelation Spectroscopy a New Method for Precise Determination of the Tilt Angle of Amphiphiles in Langmuir Monolayers. *Materials Science and Engineering: C* **1998**, *5*, 271–274.

[55] Lautz, C.; Fischer, T. M.; Weygand, M.; Lösche, M.; Howes, P. B.; Kjaer, K. Determination of Alkyl Chain Tilt Angles in Langmuir Monolayers: A Comparison of Brewster Angle Autocorrelation Spectroscopy and x-Ray Diffraction. *The Journal of Chemical Physics* **1998**, *108*, 4640–4646.

[56] Israelachvili, J. N. In *Intermolecular and Surface Forces (Third Edition)*; Israelachvili, J. N., Ed.; Academic Press: San Diego, 2011; pp 107–132.

[57] Smith, R. D.; Berg, J. C. The Collapse of Surfactant Monolayers at the Air—Water Interface. *Journal of Colloid and Interface Science* **1980**, *74*, 273–286.

[58] Ybert, C.; Lu, W.; Möller, G.; Knobler, C. M. Collapse of a Monolayer by Three Mechanisms. *The Journal of Physical Chemistry B* **2002**, *106*, 2004–2008.

[59] Lee, K. Y. C. Collapse Mechanisms of Langmuir Monolayers. *Annual Review of Physical Chemistry* **2008**, *59*, 771–791.

[60] Adam, N. K.; Jessop, G. The Structure of Thin Films. Part VIII.—Expanded Films. *Proc. R. Soc. Lond. A* **1926**, *112*, 362–375.

[61] Agrawal, M. L.; Neuman, R. D. Surface Diffusion in Monomolecular Films: I. Lateral Profile Shift in Radiotracer Method. *Journal of Colloid and Interface Science* **1988**, *121*, 355–365.

[62] MacArthur, B. W.; Berg, J. C. Surface Equations of State for Insoluble Monolayers on Aqueous Solutions. *Journal of Colloid and Interface Science* **1979**, *68*, 201–213.

[63] Bouloussa, O.; Dupeyrat, M. Disturbing Effect of Perdeuterated Fatty Acids Used as Probes in Phospholipid Monolayers. *Biochimica et Biophysica Acta (BBA) - Biomembranes* **1987**, *896*, 239–246.

[64] Müller-Landau, F.; Cadenhead, D. A. Molecular Packing in Steroid-Lecithin Monolayers, Part I: Pure Films of Cholesterol, 3-Doxyl-Cholestane, 3-Doxyl-17-Hydroxyl-Androstane, Tetradecanoic Acid and Dipalmitoyl-Phosphatidylcholine. *Chemistry and Physics of Lipids* **1979**, *25*, 299–314.

[65] Baret, J. F.; Hasmonay, H.; Firpo, J. L.; Dupin, J. J.; Dupeyrat, M. The Different Types of Isotherm Exhibited by Insoluble Fatty Acid Monolayers. A Theoretical Interpretation of Phase Transitions in the Condensed State. *Chemistry and Physics of Lipids* **1982**, *30*, 177–187.

[66] Gershfeld, N. L. The Liquid Condensed/Liquid Expanded Transition in Lipid Films: A Critical Analysis of the Film Balance Experiment. *Journal of Colloid and Interface Science* **1982**, *85*, 28–40.

[67] Bishop, D. G.; Kenrick, J. R.; Bayston, J. H.; Macpherson, A. S.; Johns, S. R. Monolayer Properties of Chloroplast Lipids. *Biochimica et Biophysica Acta (BBA) - Biomembranes* **1980**, *602*, 248–259.

[68] Albrecht, O. Experimental Study of the Stability and Metastability of Palmitic Acid. *Thin Solid Films* **1989**, *178*, 93–101.

[69] Uematsu, S.; Kimura, F.; Sonoda, Y.; Akahori, Y.; Nakagaki, M. The Temperature Dependence of Mixed Monolayers of Poly-γ-Methyl-l-Glutamate and Palmitic Acid at the Air/Water Interface. *Journal of Colloid and Interface Science* **1990**, *135*, 580–582.

[70] Adams, E. M.; Wellen, B. A.; Thiraux, R.; Reddy, S. K.; Vidalis, A. S.; Paesani, F.; Allen, H. C. Sodium–Carboxylate Contact Ion Pair Formation Induces Stabilization of Palmitic Acid Monolayers at High pH. *Physical Chemistry Chemical Physics* **2017**, *19*, 10481–10490.

[71] Rudd, B. A. W.; Vidalis, A. S.; Allen, H. C. Thermodynamic versus Non-Equilibrium Stability of Palmitic Acid Monolayers in Calcium-Enriched Sea Spray Aerosol Proxy Systems. *Physical Chemistry Chemical Physics* **2018**,

[72] Yazdanian, M.; Yu, H.; Zografi, G. Ionic Interactions of Fatty Acid Monolayers at the Air/Water Interface. *Langmuir* **1990**, *6*, 1093–1098.

[73] Tomoaia-Cotişel, M.; Zsako´, J.; Mocanu, A.; Lupea, M.; Chifu, E. Insoluble Mixed Monolayers: III. The Ionization Characteristics of Some Fatty Acids at the Air/Water Interface. *Journal of Colloid and Interface Science* **1987**, *117*, 464–476.

[74] Munden, J. W.; Blois, D. W.; Swarbrick, J. Surface Pressure Relaxation and Hysteresis in Stearic Acid Monolayers at the Air-Water Interface. *Journal of Pharmaceutical Sciences* **1969**, *58*, 1308–1312.

[75] Heikkila, R. E.; Kwong, C. N.; Cornwell, D. G. Stability of Fatty Acid Monolayers and the Relationship between Equilibrium Spreading Pressure, Phase Transformations, and Polymorphic Crystal Forms. *Journal of Lipid Research* **1970**, *11*, 190–194.

[76] Griffith, E. C.; Adams, E. M.; Allen, H. C.; Vaida, V. Hydrophobic Collapse of a Stearic Acid Film by Adsorbed L -Phenylalanine at the Air–Water Interface. *The Journal of Physical Chemistry B* **2012**, *116*, 7849–7857.

[77] Minassian-Saraga, L. T. Recent Work on Spread Monolayers, Adsorption and Desorption. *Journal of Colloid Science* **1956**, *11*, 398–418.

[78] Patil, G. S.; Matthews, R. H.; Cornwell, D. G. Kinetics of the Processes of Desorption from Fatty Acid Monolayers. *Journal of Lipid Research* **1973**, *14*, 26–31.

[79] McLean, D. S.; Vercoe, D.; Stack, K. R.; Richardson, D. The Colloidal pKa of Lipophilic Extractives Commonly Found in Pinus Radiata. *Appita Journal: Journal of the Technical Association of the Australian and New Zealand Pulp and Paper Industry* **2005**, *58*, 362.

[80] Khattari, Z.; Sayyed, M. I.; Qashou, S. I.; Fasfous, I.; Al-Abdullah, T.; Maghrabi, M. Interfacial Behavior of Myristic Acid in Mixtures with DMPC and Cholesterol. *Chemical Physics* **2017**, *490*, 106–114.

[81] Albrecht, O.; Matsuda, H.; Eguchi, K.; Nakagiri, T. The Dissolution of Myristic Acid Monolayers in Water. *Thin Solid Films* **1999**, *338*, 252–264.

[82] Guyot-Sionnest, P.; Hunt, J. H.; Shen, Y. R. Sum-Frequency Vibrational Spectroscopy of a Langmuir Film: Study of Molecular Orientation of a Two-Dimensional System. *Physical Review Letters* **1987**, *59*, 1597–1600.

[83] Gericke, A.; Huehnerfuss, H. In Situ Investigation of Saturated Long-Chain Fatty Acids at the Air/Water Interface by External Infrared Reflection-Absorption Spectrometry. *The Journal of Physical Chemistry* **1993**, *97*, 12899–12908.

[84] Pallas, N. R.; Pethica, B. A. Liquid-Expanded to Liquid-Condensed Transition in Lipid Monolayers at the Air/Water Interface. *Langmuir* **1985**, *1*, 509–513.

[85] Ruckenstein, E. On the Nature of The Liquid Expanded/Liquid Condensed Phase Transition in Monolayers of Polar Molecules. *Journal of Colloid and Interface Science* **1997**, *196*, 313–315.

[86] Lee, K. Y. C.; Gopal, A.; von Nahmen, A.; Zasadzinski, J. A.; Majewski, J.; Smith, G. S.; Howes, P. B.; Kjaer, K. Influence of Palmitic Acid and Hexadecanol on the Phase Transition Temperature and Molecular Packing of Dipalmitoylphosphatidyl-Choline Monolayers at the Air–Water Interface. *The Journal of Chemical Physics* **2001**, *116*, 774–783.

[87] Turpin, B. J.; Lim, H.-J. Species Contributions to PM2.5 Mass Concentrations: Revisiting Common Assumptions for Estimating Organic Mass. *Aerosol Science and Technology* **2001**, *35*, 602–610.

[88] Heikkila, R. E.; Deamer, D. W.; Cornwell, D. G. Solution of Fatty Acids from Monolayers Spread at the Air-Water Interface: Identification of Phase Transformations and the Estimation of Surface Charge. *Journal of Lipid Research* **1970**, *11*, 195–200.

[89] Brzozowska, A. M.; Duits, M. H. G.; Mugele, F. Stability of Stearic Acid Monolayers on Artificial Sea Water. *Colloids and Surfaces A: Physicochemical and Engineering Aspects* **2012**, *407*, 38–48.

[90] Keene, W. C.; Pszenny, A. A. P.; Maben, J. R.; Stevenson, E.; Wall, A. Closure Evaluation of Size-Resolved Aerosol pH in the New England Coastal Atmosphere during Summer. *Journal of Geophysical Research: Atmospheres* **2004**, *109*.

[91] Salter, M. E.; Hamacher-Barth, E.; Leck, C.; Werner, J.; Johnson, C. M.; Riipinen, I.; Nilsson, E. D.; Zieger, P. Calcium Enrichment in Sea Spray Aerosol Particles. *Geophysical Research Letters* **2016**, *43*, 2016GL070275.

Appendix A

Lauric Acid

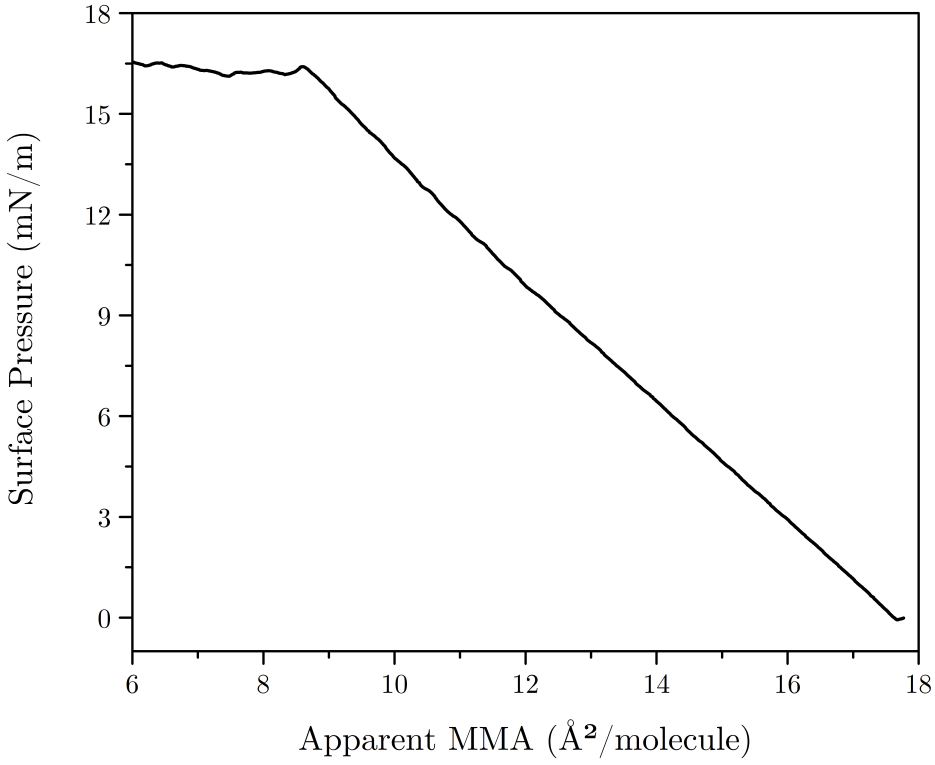

Figure A.1: Π-A isotherm of lauric acid on ultrapure water at pH 2.0.

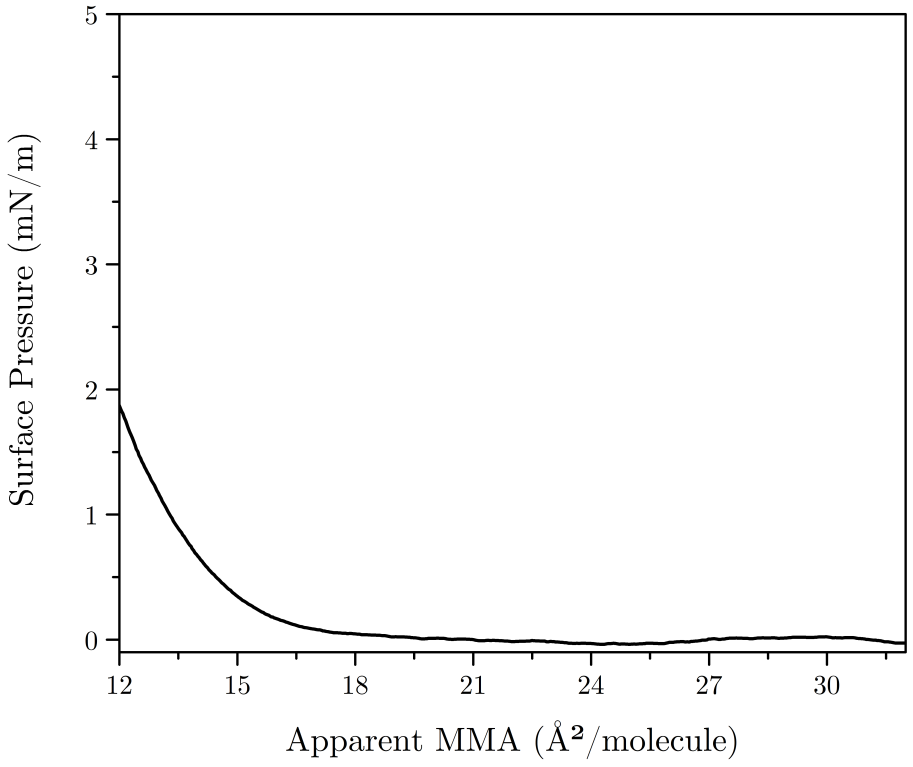

Figure A.2: Π-A isotherm of lauric acid on ultrapure water at pH 5.6.

Appendix B

SSA Proxy Surface Pressure-Area Isotherms

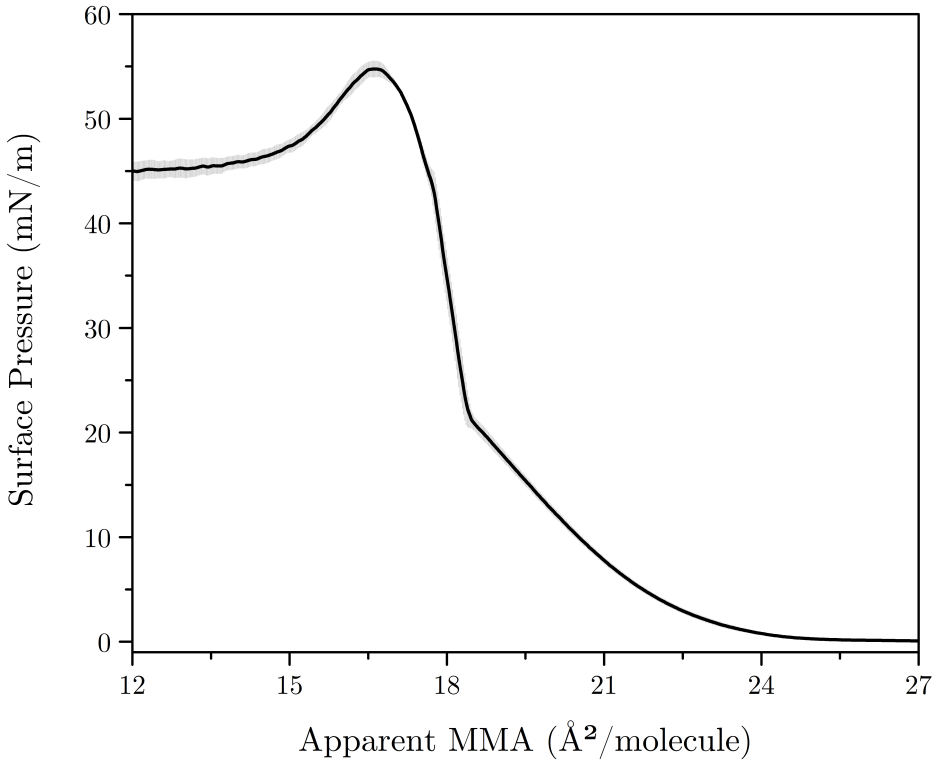

Figure B.1: Π-A isotherm of the SSA proxy mixture on ultrapure water at pH 5.6.

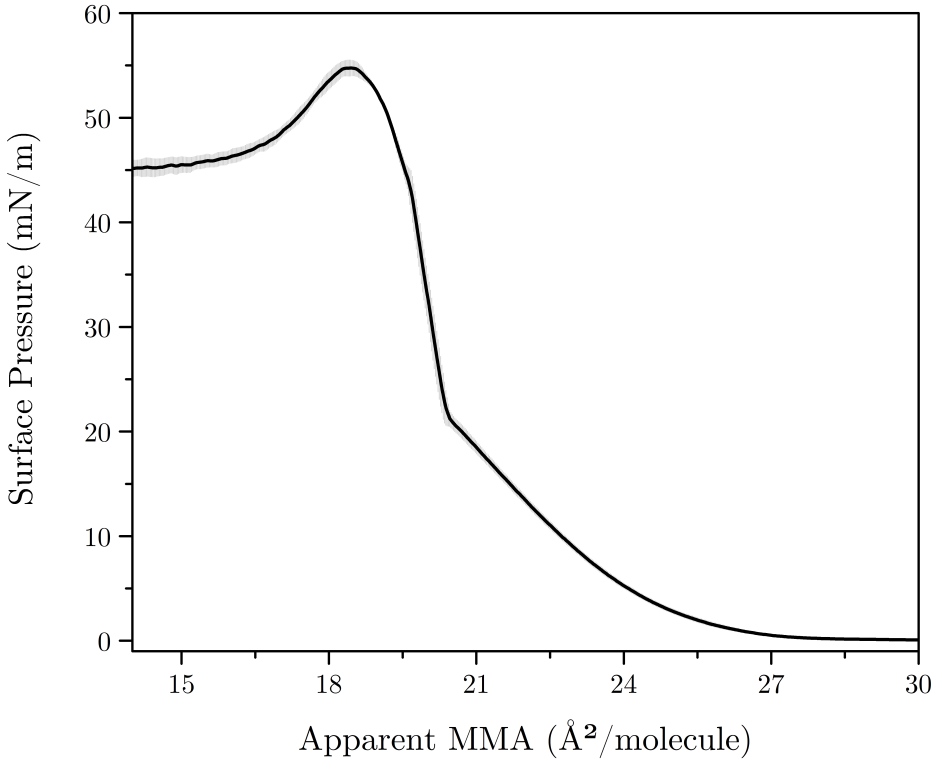

Figure B.2: Π-A isotherm of the SSA proxy mixture on ultrapure water at pH 5.6. The lauric acid mole fraction contribution has been subtracted from the total mean molecular area.

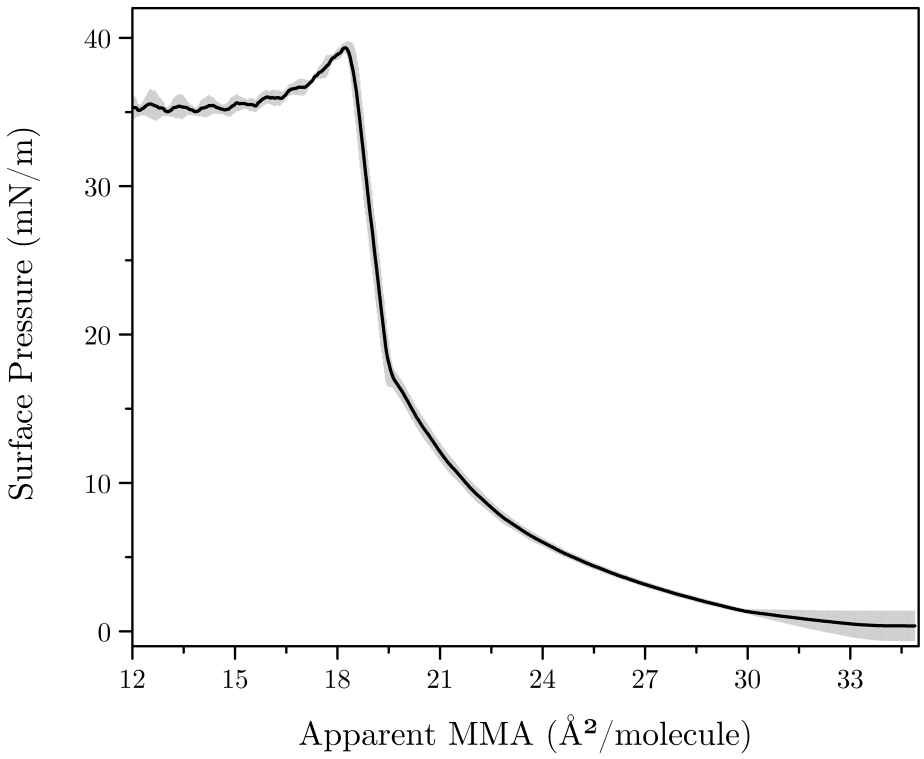

Figure B.3: Π-A isotherm of the SSA proxy mixture on ultrapure water at pH 2.0.

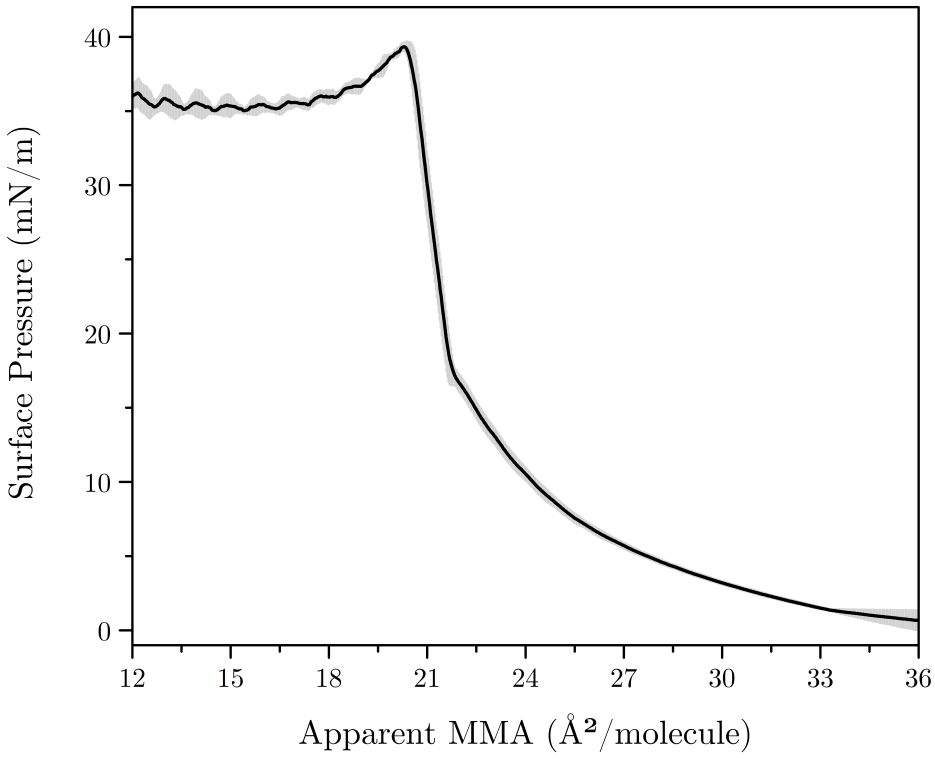

Figure B.4: Π-A isotherm of the SSA proxy mixture on ultrapure water at pH 2.0. The lauric acid mole fraction contribution has been subtracted from the total mean molecular area.

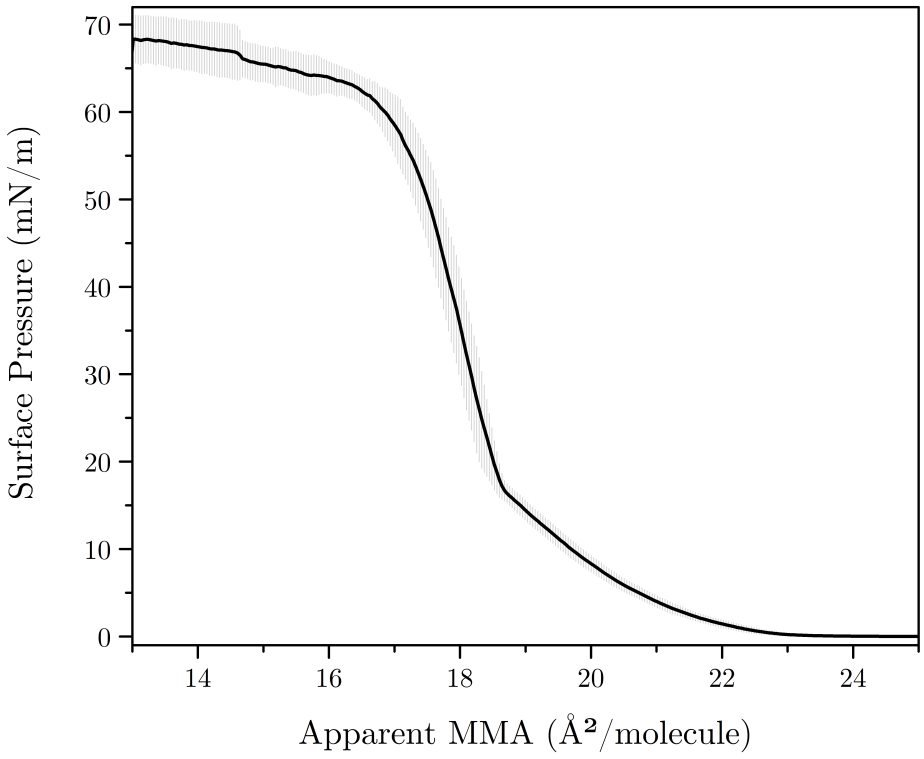

Figure B.5: Π-A isotherm of the SSA proxy mixture on aqueous 0.4 M NaCl at pH 8.2.

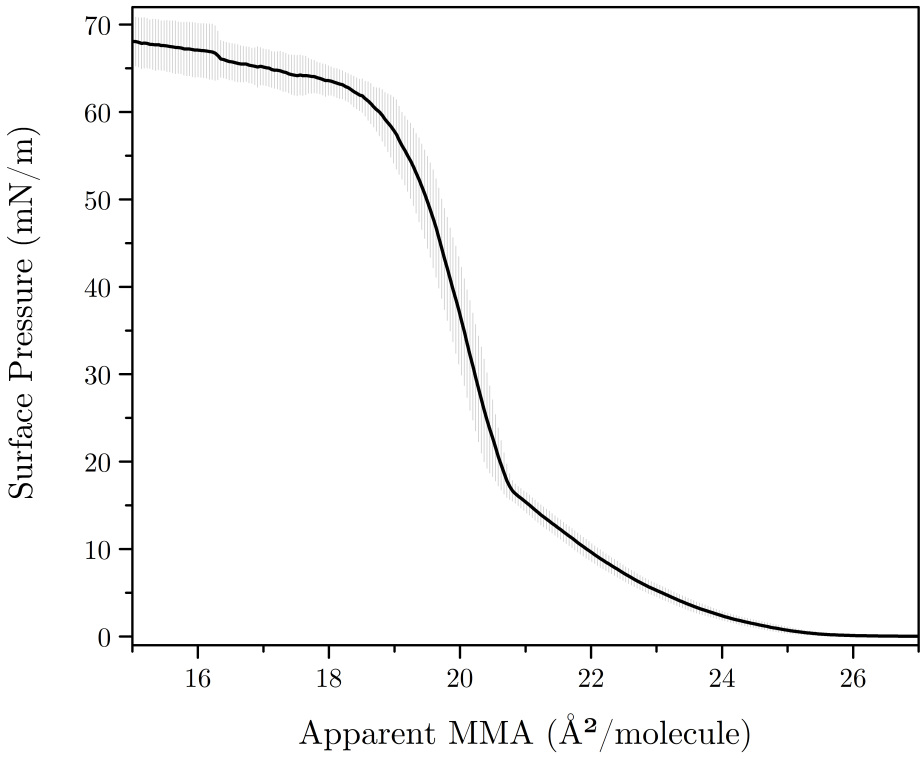

Figure B.6: Π-A isotherm of the SSA proxy mixture on aqueous 0.4 M NaCl at pH 8.2. The lauric acid mole fraction contribution has been subtracted from the total mean molecular area.

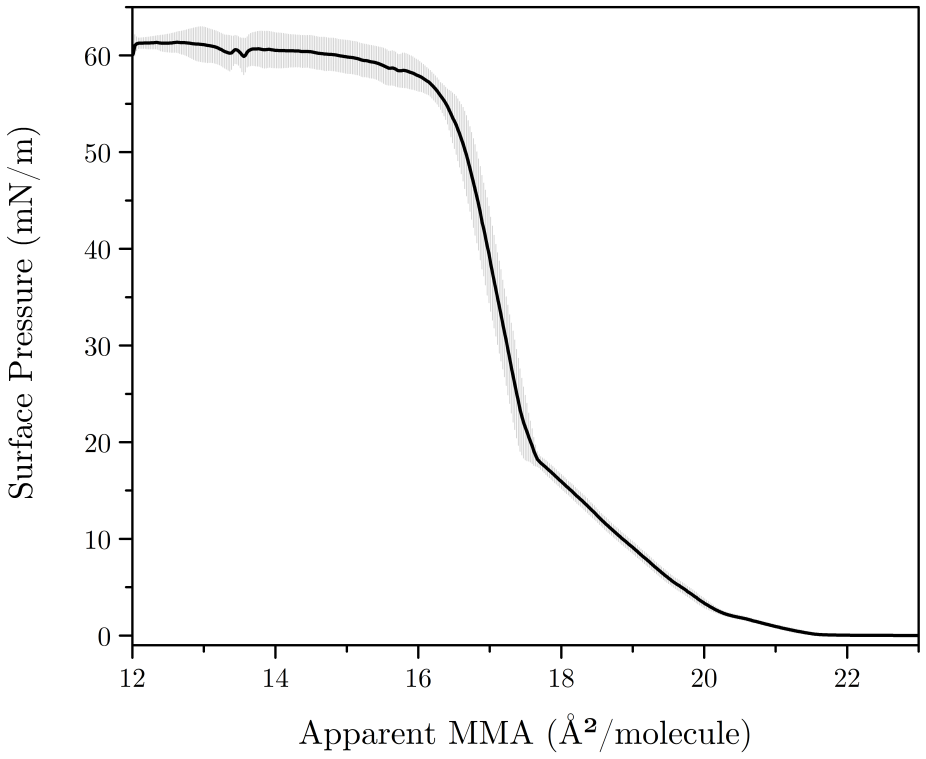

Figure B.7: Π-A isotherm of the SSA proxy mixture on aqueous 0.4 M NaCl at pH 5.6.

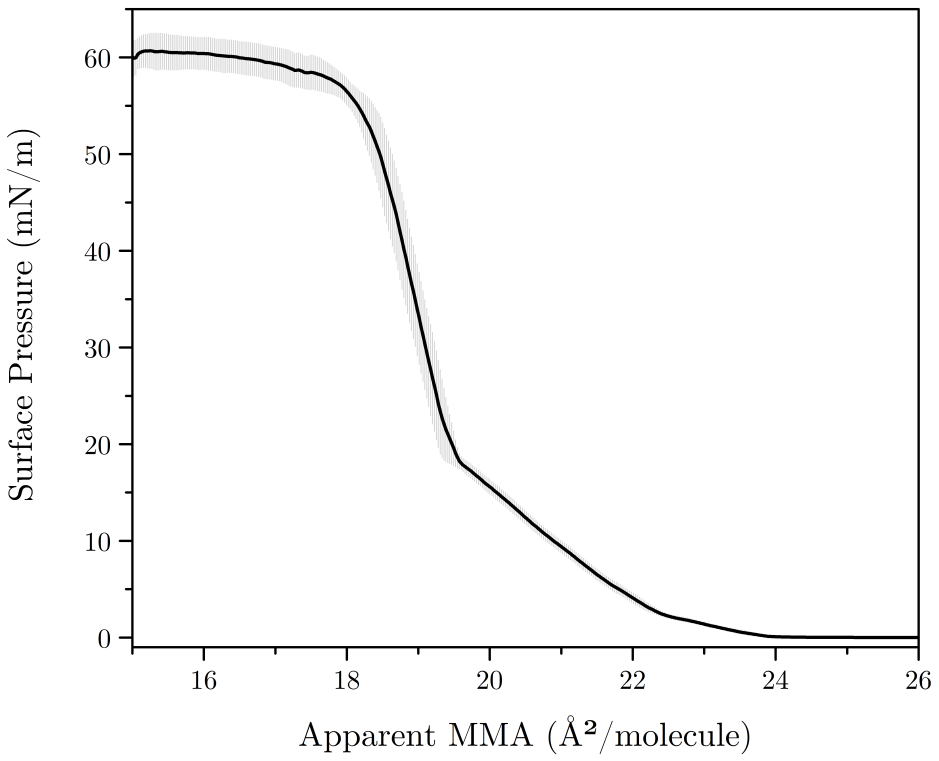

Figure B.8: Π-A isotherm of the SSA proxy mixture on aqueous 0.4 M NaCl at pH 5.6. The lauric acid mole fraction contribution has been subtracted from the total mean molecular area.

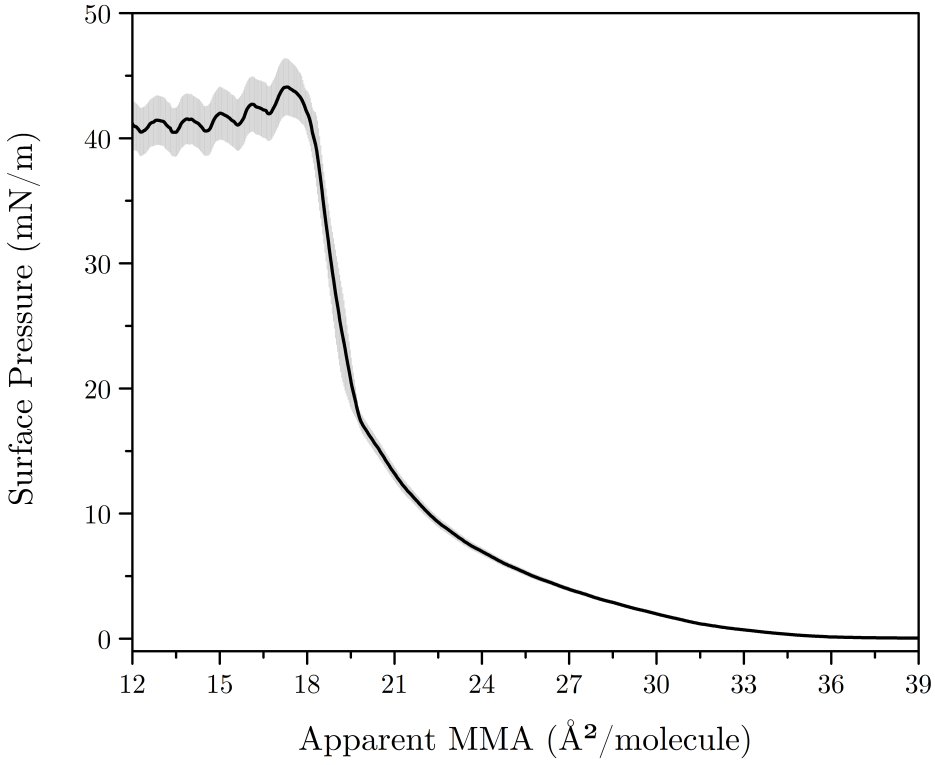

Figure B.9: Π-A isotherm of the SSA proxy mixture on aqueous 0.4 M NaCl at pH 2.0.

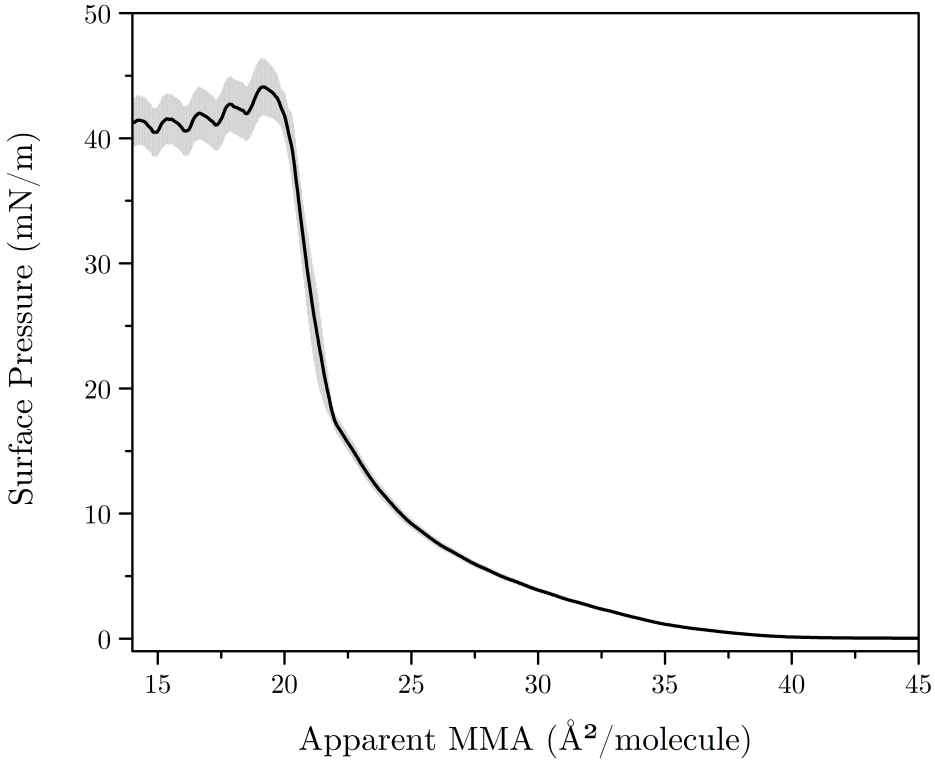

Figure B.10: Π-A isotherm of the SSA proxy mixture on aqueous 0.4 M NaCl at pH 2.0. The lauric acid mole fraction contribution has been subtracted from the total mean molecular area.

Appendix C

Control SSA Proxy Surface Pressure-Area Isotherms

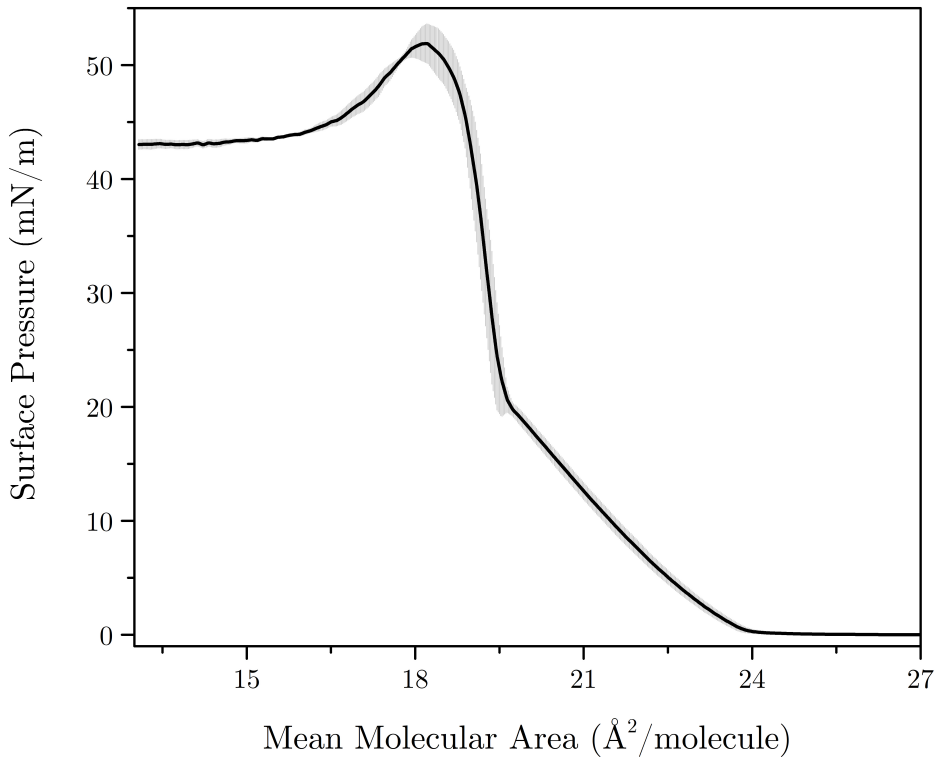

Figure C.1: Π-A isotherms of the control SSA proxy mixture on ultrapure water at pH 5.6.

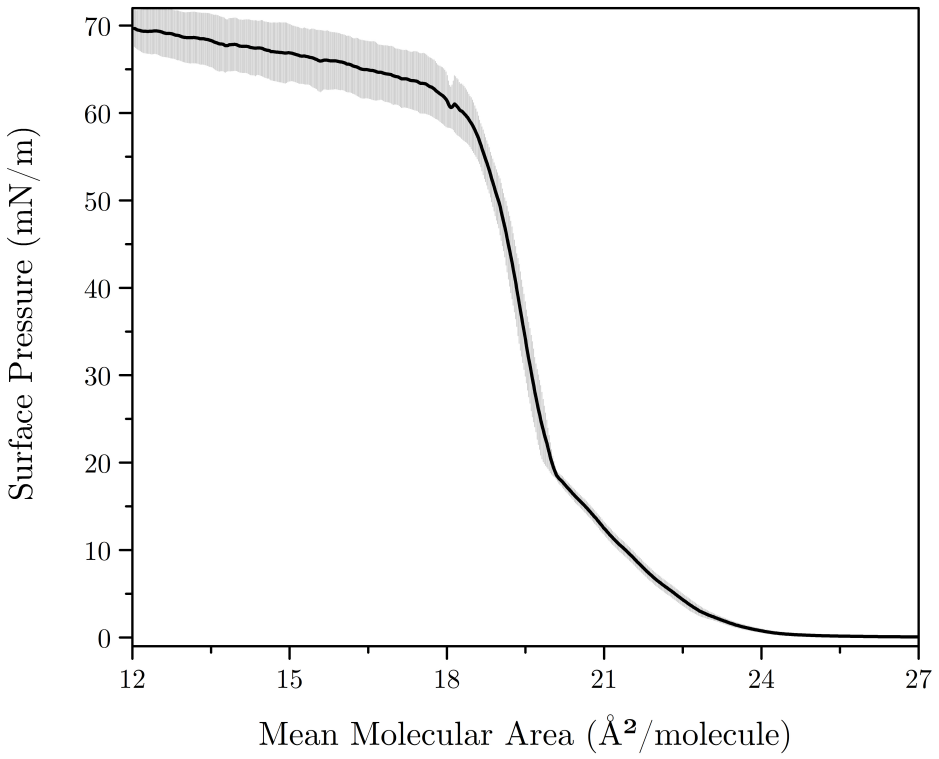

Figure C.2: Π-*A* isotherms of the control SSA proxy mixture on aqueous 0.4 M NaCl at pH 8.2.

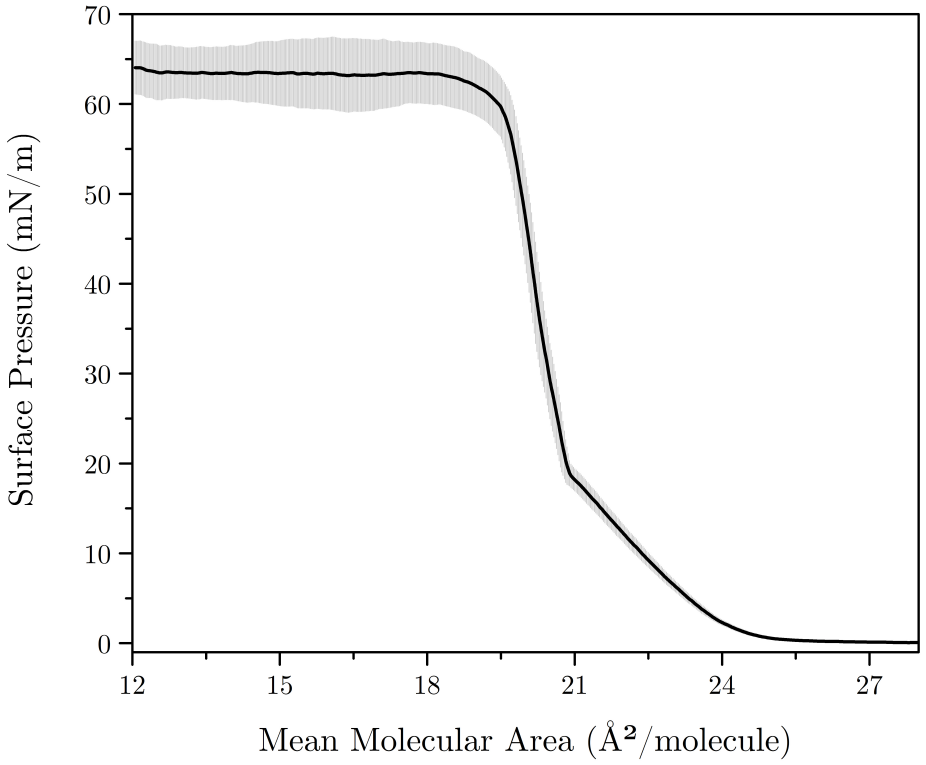

Figure C.3: Π-*A* isotherms of the control SSA proxy mixture on aqueous 0.4 M NaCl at pH 5.6.

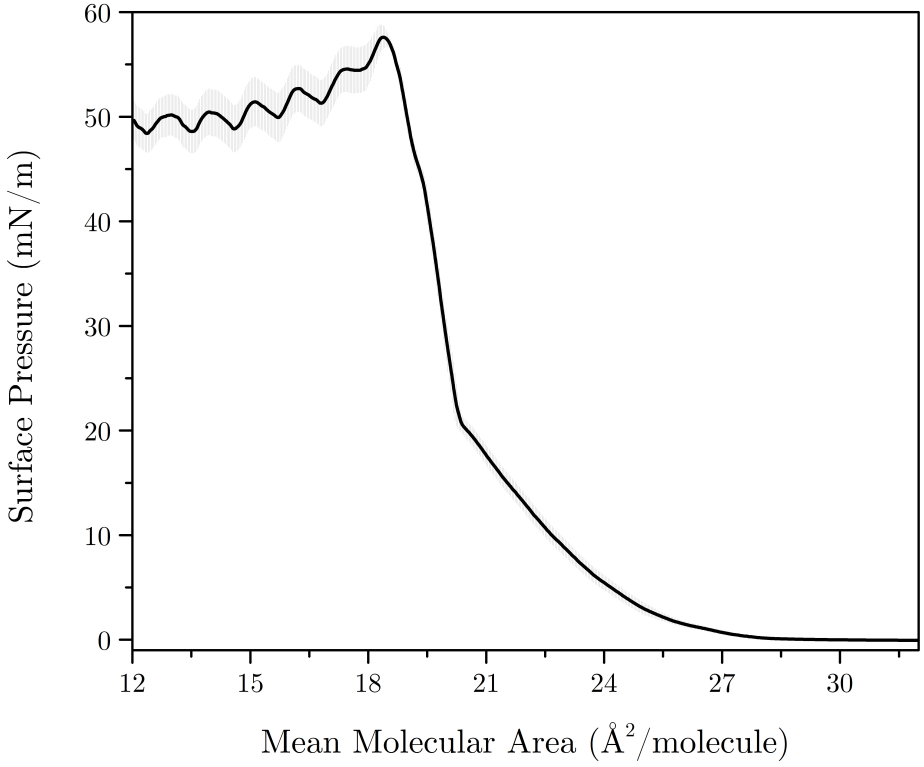

Figure C.4: Π-*A* isotherms of the control SSA proxy mixture on aqueous 0.4 M NaCl at pH 2.0.

Appendix D

Isotherm Constant Area Analysis

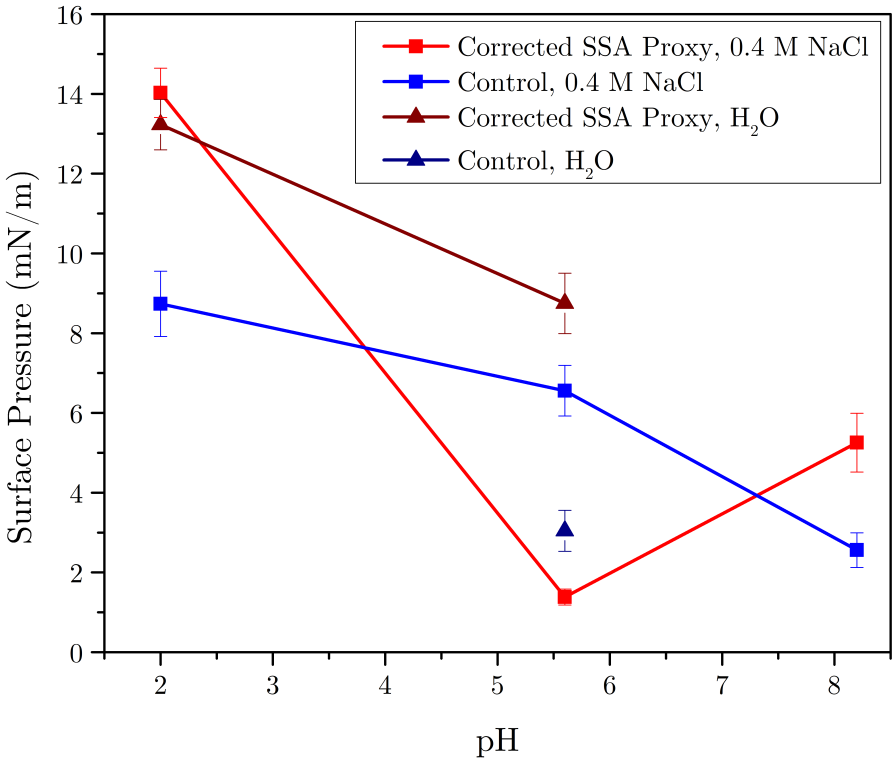

Figure D.1: Constant mean molecular area analysis of the fatty acid mixture isotherms. The surface pressure at an MMA of 23 $Å^2$/molecule is plotted as a function of subphase pH.

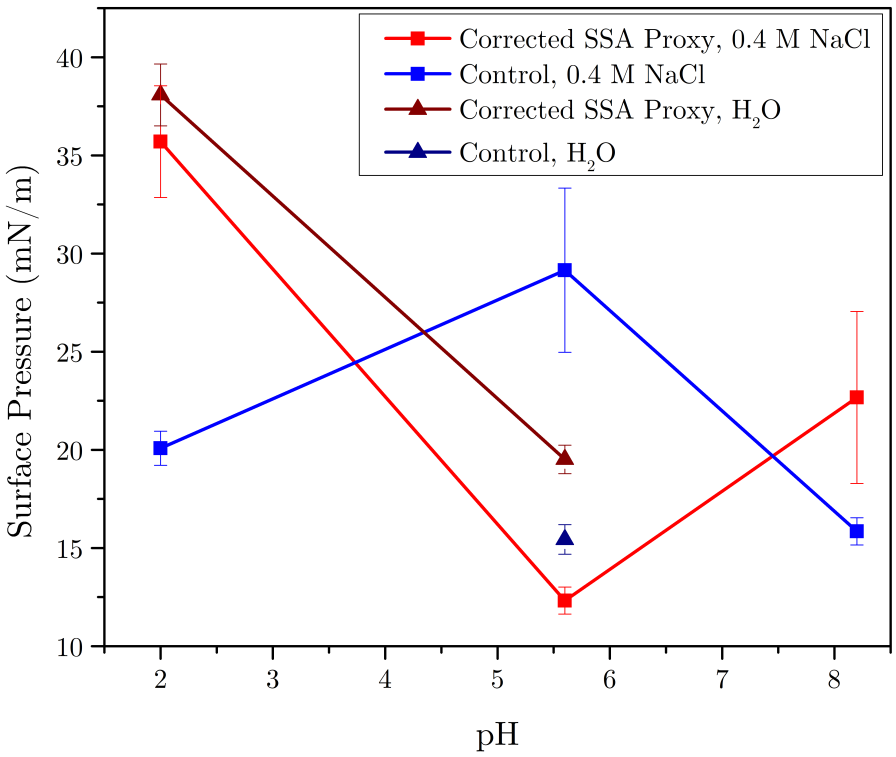

Figure D.2: Constant mean molecular area analysis of the fatty acid mixture isotherms. The surface pressure at an MMA of 20.5 Å^2/molecule is plotted as a function of subphase pH.